



TECHNISCHE
UNIVERSITÄT
WIEN
Vienna University of Technology



MEDIZINISCHE
UNIVERSITÄT WIEN

Diplomarbeit

Entwicklung eines magnetresonanz-kompatiblen Torso-Bewegungs-Phantoms

Development of a magnetic-resonance-compatible torso motion phantom

zur Erlangung des akademischen Grades

Diplom-Ingenieur

im Rahmen des Studiums

Biomedical Engineering

eingereicht von

Ernesto Jesús Gómez Tamm

Matrikelnummer: 11938264

ausgeführt am Hochfeld MR Zentrum, Zentrum für Medizinische Physik und Biomedizinische Technik, Medizinische Universität Wien
in Zusammenarbeit mit dem Institut für Angewandte Physik
der Fakultät für Physik der Technischen Universität Wien

Betreuung

Hauptbetreuung: Roberta Frass-Kriegl, M.Sc., Ph.D.

Mitbetreuung: Ao.Univ.Prof. Dipl.-Ing. Dr.techn. Martin Gröschl

Wien, am 23.08.2023

Ernesto Gómez Tamm

Martin Gröschl



Die approbierte gedruckte Originalversion dieser Diplomarbeit ist an der TU Wien Bibliothek verfügbar
The approved original version of this thesis is available in print at TU Wien Bibliothek.



TECHNISCHE
UNIVERSITÄT
WIEN
Vienna University of Technology



MEDICAL UNIVERSITY
OF VIENNA

Diploma Thesis

in the master's Degree

Biomedical Engineering

Interfaculty studies

at the

High Field MR Center

in the Center for Medical Physics and Biomedical Engineering
at the Medical University of Vienna

with collaboration of the Institute of Applied Physics
Faculty of Physics

Vienna University of Technology

Topic:

Development of a magnetic-resonance-compatible torso motion phantom

Entwicklung eines magnetresonanz-kompatiblen Torso-Bewegungs-Phantoms

Author: Ernesto Jesús Gómez Tamm, B.Sc.
Student ID: 11938264
Supervisor: Roberta Frass-Kriegl, M.Sc., Ph.D.
Professor and examiner: Ao.Univ.Prof. Dipl.-Ing. Dr.techn. Martin Gröschl
Date of submission: 23. August 2023



Die approbierte gedruckte Originalversion dieser Diplomarbeit ist an der TU Wien Bibliothek verfügbar
The approved original version of this thesis is available in print at TU Wien Bibliothek.

Statutory Declaration

I hereby declare on my honor that I have prepared this thesis independently. Only the sources and aids expressly named in the thesis have been used. I have marked as such any ideas that I have taken over verbatim or in spirit.

Ernesto Jesús Gómez Tamm

Vienna, 23.08.2023

Eidesstattliche Erklärung

Ich erkläre hiermit ehrenwörtlich, dass ich die vorliegende Arbeit selbstständig angefertigt habe. Es wurden nur die in der Arbeit ausdrücklich benannten Quellen und Hilfsmittel benutzt. Wörtlich und sinngemäß übernommenes Gedankengut habe ich als solches kenntlich gemacht.

Ernesto Jesús Gómez Tamm

Wien, 23.08.2023

Acknowledgment

This project not only offers me the opportunity to document the result of my final thesis but also gives me a chance to thank the people who contributed to the success of my thesis. I hereby would like to express my profound gratitude to all those who have supported me in completing this master's thesis, and in particular, the following:

I am deeply thankful to my thesis supervisor, Roberta Frass-Kriegl, for her invaluable guidance, scientific expertise, and continuous support throughout this project. This thesis could not have been done without your help and patience after inviting me to join your team.

I extend my gratitude to Prof. Martin Gröschl for taking the supervisor role, from the TU Wien side, in a very short term. As well as Prof. Gerald Badurek for allowing me to start this project and always being helpful even in difficult times. I thank both for their guidelines and assessment of this work.

Special thanks to Andreas Hodul for the invaluable technical assistance and expertise in manufacturing, which proved crucial, alongside numerous discussions, in successfully completing this project.

This research benefitted from the collaborative efforts of various experts and researchers. Here I would like to thank Ivo Rausch and his team, Markus Ortner and Zacharias Chalampalakis, for their help and cooperation in building and developing the different modules and Quang Nguyen for his well-employed programming skills.

I want to acknowledge the support of Elmar Laistler for welcoming me into the RF Lab and allowing me to do this project as a team member. I also want to thank Onisim Soanca for always helping me with the use of the Lab and 3D printing technology. Additionally, my thanks go to all the colleagues in the RF Lab, Lena, Michael, Raphi, Veronica, Thomas, and also Benedikt (even if not exactly part of the team). I am grateful for their willingness to engage in fruitful discussions, knowledge exchange, and motivational speeches during the very numerous coffee and lunch breaks and for really making me feel part of the team!

I extend my appreciation to Albrecht Ingo Schmid, Wolfgang Birkfellner, Lorenz Kiss, and Paul Péry for their cooperation and assistance during the project. As well as the rest of the MR Center employees for their fair treatment and conversations in the k-space.

I want to acknowledge the support of Basti Rapp for having me as an equal partner during the thesis, motivating each other after each step. I thank him, as well as Miriam Schmid and Lena Stadtmüller, for their camaraderie, assistance, and support through this shared journey, likewise to all the non-study related plans we had, which have been equally crucial in making this work available in this form.

My profound gratitude goes out to all my friends around the world and in the context of this work, particularly those in Vienna, especially Björn, Philipp G., Arthur, Tobi, and Javi. For positive distractions and moral support, I would like to thank them, who have accompanied me at all times during my studies.

To my Austrian family, I extend my sincere thanks to my aunt Elisabeth, uncle Fritz, and cousins Paul and Philipp, who have continuously backed me since I arrived in Vienna.

My most heartfelt thanks go to Mirjam Gößwein, who was constantly at my side not only during this work but also throughout the most important years of my studies and life, motivating and supporting me at all times. Even in difficult times, but also in the most beautiful ones, you were there for me. Thank you for this, my love!

Finally, I am immensely grateful to the rest of my family for their lifelong support. In particular, I thank my mother Edeltraud, for her unparalleled kindness and transfer of work ethic, my father Ernesto, for his desire for wisdom and care for the family, and my brother Alejandro, for his unwavering loyalty and deep understanding. I deeply appreciate everything that you have done during my life and without you, I could not have achieved any of this or be the person I am today. You know I love you for this.

Ohne Euch wäre dies alles nicht möglich gewesen. ¡Muchas gracias por todo!

Financial support from the MedUni internal Φ ocus grant *T4MR* and the Austrian Science Fund (FWF) project no. P35305-B *AquaLactEMISM* is gratefully acknowledged.

Abstract

The non-ionizing medical imaging technique of magnetic resonance imaging (MRI), based on the behavior of nuclear magnetic moments in an external magnetic field, is relatively novel compared to other medical imaging methods. Therefore, significant optimization advances are still being made. One of the regions where image acquisition and quality can be improved is artifact reduction. The most critical quality-reducing artifacts for the vital torso region of the patient are the motion artifacts, typically generated by breathing and heart motion.

Accordingly, motion correction and tracking systems are being researched. To better develop these systems, a testing setup in the form of an MRI-compatible torso motion phantom is highly needed. Through this setup, the systems can be tested without the need for patients, as well as calibrated and validated due to its precise known reproducible movement.

This torso motion phantom was fully developed and designed in this thesis and manufactured as far as possible in the given time. In order to make the phantom as versatile and adaptable to various research interests as possible, a modular design was chosen. Each module features one type of motion and could be individually replaced or adjusted for specific needs in the future.

The biggest hurdle to overcome while developing the motion phantom was securing its MRI compatibility, which partially means avoiding metallic parts, which is the most common material used in engineering when building a system with motion. Accordingly, new manufacturing methods were used, and polymers were heavily relied on. Furthermore, materials with approximate physiological relaxation times had to be implemented to get optimal images.

The motion phantom was divided into four primary modules. The Outer Shell module confines the whole phantom in a ribcage-like acrylic water shell. The Chest Motion module created the chest wall elevation movement found in laying down breathing patients. The Abdominal Organ Bulk module, which simulates the organ shift due to pulmonary expansion, and can house other specific organ phantoms. Lastly, the Heart Motion module moves a heart phantom with the heartbeat frequency while being displaced by the breathing motion of the other modules.

Sophisticated non-magnetic linear piezo stages displace the Chest Motion and Abdominal Organ Bulk modules, while a self-made polymer pneumatic piston actuates the Heart Motion module.

The movement of this phantom will be first used for the development of a Beat Pilot Tone motion tracking system. Nevertheless, further module customization and alternatives are already being planned for future studies.

Kurzfassung

Die nicht-ionisierende medizinische Bildgebungsmethode der Magnetresonanztomographie (MRT), die auf der Wechselwirkung von Atomkernen in externen Magnetfeldern beruht, ist im Vergleich zu anderen medizinischen Bildgebungsverfahren relativ neu. Daher werden immer noch bedeutende Optimierungsfortschritte gemacht. Einer der Bereiche, in denen die Bildaufnahme und -qualität verbessert werden kann, ist die Artefaktreduktion. Die kritischsten qualitätsmindernden Artefakte für die medizinisch relevante Rumpfregeion des Patienten sind die Bewegungsartefakte, die durch Atem- und Herzbewegungen entstehen können.

Daher wird an Systemen zur Bewegungskorrektur und -verfolgung geforscht. Um diese Systeme besser entwickeln zu können, ist ein Testaufbau in Form eines MRT-kompatiblen Torso-Bewegungsphantoms dringend erforderlich. Mit diesem Versuchsaufbau können die Systeme ohne Patienten getestet und aufgrund der präzisen, bekannten und reproduzierbaren Bewegung kalibriert und validiert werden.

Dieses Torso-Bewegungsphantom wurde in dieser Arbeit vollständig entwickelt und konstruiert und so weit wie in der vorgegebenen Zeit möglich hergestellt. Um möglichst vielen Bedürfnissen der unterschiedlichen interessierten Forschungsteams gerecht zu werden, wurde das Bewegungsphantom in Module unterteilt, die für jeden spezifischen Bedarf ausgetauscht oder angepasst werden können.

Die größte Hürde, die es bei der Entwicklung des Bewegungsphantoms zu überwinden galt, war die Sicherstellung seiner MRT-Kompatibilität, was bedeutet, dass teilweise metallische Teile vermieden werden müssen, das in der Technik am häufigsten verwendete Material beim Bau eines Bewegungssystems. Deshalb wurden neue Herstellungsmethoden angewandt und in hohem Maße Polymere eingesetzt. Außerdem mussten Materialien mit annähernd physiologischen Relaxationszeiten verwendet werden, um optimale Bilder zu erhalten.

Das Bewegungsphantom wurde in vier Hauptmodule unterteilt. Das Outer Shell Modul (äußere Hülle) schließt das gesamte Phantom in einer rippenkäfigartigen Acrylwasserhülle ein. Das Chest Motion Modul (Brustkorbbewegung) erzeugt die Heb- und Senkbewegung der Brust, die bei liegenden, atmenden Patienten auftritt. Das Abdominal Organ Bulk Modul (inneren Organe Hauptmasse) simuliert die Verschiebung der inneren Organe aufgrund der Lungenausdehnung und kann andere spezifische Organphantome aufnehmen. Zuletzt bewegt das Heart Motion Modul (Herzbewegung) ein Herzphantom mit der Herzschlagfrequenz, während es durch die Atembewegung der anderen Module verschoben wird.

Hochentwickelte nichtmagnetische lineare piezoelektrische Motoren verschieben die Module Chest Motion und Abdominal Organ Bulk, während ein selbst hergestellter pneumatischer Polymerkolben das Modul Heart Motion betätigt.

Die Bewegung dieses Phantoms wird zunächst für die Entwicklung eines Beat Pilot Tone Systems, zur Bewegungsverfolgung, verwendet. Dennoch sind weitere Modulanpassungen und Alternativen für zukünftige Studien bereits in Planung.

List of Abbreviations

<i>Acronym</i>	<i>Meaning</i>	<i>Acronym</i>	<i>Meaning</i>
MRI	magnetic resonance imaging	EMI	electromagnetic interference
MP	motion phantom	MP	motion phantom
MR	magnetic resonance	CAD	computer aided design
E	energy	3D	three dimensional
RF	radio frequency	PVC	polyvinyl chloride
NMR	nuclear magnetic resonance	FDM	fused deposition modeling
HR	high radio frequency	PLA	polylactic acid
Tx	transmit	SLA	stereolithography
Rx	receive	PMMA	polymethylmethacrylate
FOV	field of view	OS	Outer Shell
ROI	region of interest	CM	Chest Motion
PET	positron emission tomography	AOB	Abdominal Organ Bulk
UTE	ultrashort echo time	ABS	acrylonitrile butadiene styrene
TE	echo time	AKH	Vienna general hospital
ZTE	zero echo time	DIN	Deutsches Institut für Normung
MA	motion artifacts	HM	Heart Motion
SE	spin echo	PA 6	polycaprolactam
GE	gradient echo	DAQ	data acquisition
ECG	electrocardiogram	SP	Scanner Plate
CMPBME	Center for Medical Physics and Biomedical Engineering		

Table of Contents

STATUTORY DECLARATION	I
ACKNOWLEDGMENT	III
ABSTRACT	V
KURZFASSUNG	VI
LIST OF ABBREVIATIONS	VII
1 INTRODUCTION	1
1.1 MOTIVATION	1
1.2 AIM	2
2 THEORETICAL BACKGROUND	3
2.1 NUCLEAR MAGNETIC RESONANCE	3
2.1.1 <i>Spins and Magnetization</i>	3
2.1.2 <i>Radiofrequency Coils</i>	5
2.1.3 <i>Torso MRI</i>	7
2.2 SIGNAL, NOISE, AND ARTIFACTS IN NMR	9
2.2.1 <i>Signal in different Materials</i>	9
2.2.2 <i>Material-induced Noise and Artifacts</i>	14
2.2.3 <i>Motion Artifacts</i>	18
2.3 IMAGING PHANTOMS	21
2.3.1 <i>NMR Phantoms</i>	21
2.3.2 <i>NMR Motion Phantoms</i>	22
2.3.3 <i>NMR Phantom Manufacturing Techniques</i>	23
2.4 MOTION REDUCTION, MEASUREMENT AND CORRECTION	26
3 PHANTOM DESIGN AND DEVELOPMENT	29
3.1 MOTION PHANTOM OVERVIEW	29
3.1.1 <i>Requirements</i>	29
3.1.2 <i>Modules</i>	30
3.1.3 <i>Design and Manufacturing Tools</i>	32
3.2 OUTER SHELL	34
3.2.1 <i>Requirements</i>	34
3.2.2 <i>Design</i>	34
3.2.3 <i>Manufacturing and Materials</i>	37
3.3 CHEST MOTION	39
3.3.1 <i>Requirements</i>	39
3.3.2 <i>Design</i>	39
3.3.3 <i>Manufacturing and Materials</i>	44
3.3.4 <i>Test and Evaluations</i>	48
3.4 ABDOMINAL ORGAN BULK MOTION	51
3.4.1 <i>Requirements</i>	51
3.4.2 <i>Design</i>	52
3.4.3 <i>Manufacturing and Materials</i>	57

3.5 HEART MOTION	59
3.5.1 Requirements	59
3.5.2 Design	60
3.5.3 Manufacturing and Materials	67
3.5.4 Test and Evaluations	70
3.6 SCANNER PLATE (AND EXTRA HARDWARE)	72
3.6.1 Requirements	72
3.6.2 Design	72
3.6.3 Manufacturing and Materials	73
4 DISCUSSION	74
4.1 ASSESSMENTS AND LIMITATIONS	74
4.1.1 Evaluation of Module Design	74
4.1.2 Evaluation of Module Manufacture and Materials	76
4.1.3 Evaluation of Project Management	77
4.2 OUTLOOK	78
4.2.1 Phantom Development Outlook	78
4.2.2 Phantom Use Outlook	78
5 CONCLUSION	80
LIST OF REFERENCES	81
LIST OF FIGURES	84
LIST OF TABLES	89
APPENDIX	90

1 Introduction

1.1 Motivation

Magnetic resonance imaging (MRI) is a non-ionizing imaging technique that contrasts on this point with other medically used imaging methods based on X-rays. This fact makes MRI more secure and less intimidating for getting detailed image slices of the inside of biological bodies, primarily medical patients, in order to recognize, identify and track anomalies and diseases in the interior of the body. Nevertheless, this method is relatively novel. Even though its theoretical development spans from the 1950s to the 1980s, its standard medical implementation does not surpass the last 30 years, making it a relatively new medical imaging technology. For this reason, significant progress is still being made with every new technological breakthrough in order to optimize this methodology further. These advancements could be made in the scanner itself, its complementary hardware, or the complex evaluating software.

One of the areas where MRI can be further improved is artifact reduction. Artifacts are commonly the most significant imaging degrading source, which could even lead to the discarding and repetition of the scanned image. Radiologists and other imaging personnel are frequently not informed about the medical history of patients, which could lead to misconceptions when viewing artifacts in scans that could be confused with pathologies or foreign bodies and vice versa. Almost every MRI exam includes some kind of artifact that degrades the image quality, which can be classified into different groups depending on their origin. With material artifacts, the most common and damaging one to the image is the motion artifact.

As the name indicates, this artifact type is created when the imaged body section is displaced during the image acquisition. This fact is true for most medical imaging modalities. Nevertheless, the long scanning times and the complex Fourier-based data acquisition make MRI more susceptible to them. Patients have to lay still in the tight, loud scanner bore for prolonged measurements, which is not always an easy task. Furthermore, in the torso, which is often a region of interest due to all the vital organs that can be found there, the breathing and heart motion do also create these artifacts. These two motions can only be stopped for short periods of time in the case of breathing or not at all in the case of the heartbeat. Therefore, researchers strive to control, reduce or even eliminate these motion artifacts through various methods in order to increase the image sensitivity and lower the obstruction of small anatomical structures. One of the methods being explored is tracking the patient's body motion and correcting image motion artifacts through software.

1.2 Aim

For the purpose of developing motion tracking and motion correction systems for movement in the torso region, a testing setup is needed. This setup substantially decreases the number of patients that have to be scanned for research purposes. The envisioned test setup is an MRI-compatible torso motion phantom.

This phantom would have materials with similar relaxation times as the simulated human tissue to get comparable signals. Furthermore, the phantom would need a precise and discrete movement that creates a reliable and reproducible motion source. This way, the motion tracking and correction systems can be conveniently tested, as well as validated and calibrated in future development steps.

The desired MRI motion phantom should simulate the breathing and heartbeat motion of the torso. These movements should be achieved through a modularity concept to be as interchangeable and adaptable in further tests and research topics as possible. Through this concept, the need for a new phantom for each new research topic is reduced, maintaining this new motion phantom relevant for years to come with just the need to develop a single interchangeable module.

2 Theoretical Background

In order to understand the requirements and usage of a motion phantom (MP) for magnetic resonance imaging (MRI), as well as the thought process behind its design and development, theoretical knowledge of MRI itself is required. Understanding how an image is achieved and which hardware is needed in the process is critical to determine the current process's flaws. Only then can this knowledge be applied to develop a phantom that recreates the human body with specific characteristics to find possible solutions to problems and optimize the imaging procedure.

2.1 Nuclear Magnetic Resonance

2.1.1 Spins and Magnetization

The main functional element of nuclear magnetic resonance (NMR), and therefore of MRI, revolves around the spin of atomic nuclei and their interaction when put in a magnetic field. The spin is the intrinsic angular momentum of the protons and neutrons in the nuclei of the atoms. This angular momentum \mathbf{I} is described in quantum mechanics and quantized to give discrete values.[1, 2]

$$|\mathbf{I}| = \hbar\sqrt{I(I+1)} \quad (1)$$

Depending on the number of protons and neutrons in the nucleus, I can either have an integer value, half an integer value, or zero. \hbar is the reduced Planck constant. If a nucleus has a non-zero angular momentum, it also possesses a magnetic moment μ linked to the angular momentum by the gyromagnetic ratio γ in the following equation.[1, 2]

$$\mu = \gamma\mathbf{I} \quad (2)$$

This magnetic moment is found on atoms with an odd number of nucleons. Several nuclei can be used and detected for MRI thanks to this characteristic, such as ^{13}C , ^{23}Na , or ^{31}P . Nevertheless, the most commonly used nucleus for imaging is Hydrogen ^1H . ^1H is a stable nucleus that is most abundant in the human body since nearly every organ and tissue consists partly of water, thus Hydrogen can be found. Furthermore, it possesses a high gyromagnetic ratio, with specific and achievable resonance frequencies in the 1.5-7T magnetic field of standard MRI machines. This static magnetic field B_0 is created by a superconductor around the machine's bore. B_0 is a constant and steady field that points in the z-direction when the isocenter of the scanner is viewed, which is the region used for imaging. This strong field influences the nuclei's naturally randomly oriented spins to align themselves in a precession movement, either parallel or antiparallel to B_0 , i.e. here, the z-axis (Figure 2.1a). Without B_0 , the direction of all \mathbf{I} is random, producing an equally energetic distribution. Nevertheless, with the static magnetic field, the $2I+1$ possible different discrete spin orientations are split into two possible states in the case of ^1H . This split is called the Zeeman effect, which is

2 Theoretical Background

described visually in Figure 2.1b. The magnetic moment of nuclei in a static external magnetic field possesses a potential energy E , described in the following equation.[3, 4]

$$E = -\mu B_0 = -\gamma m_I \hbar B_0 \quad (3)$$

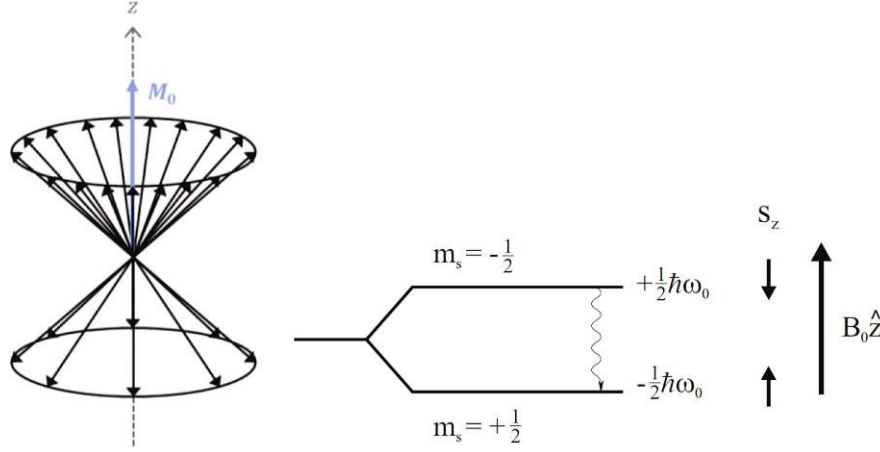


Figure 2.1: Left: Schematic illustration portrayed by arrows of the precession movement around the z -axis of the static magnetic field M_0 , with most spins in the lower energy state parallel to M_0 [4]. Right: Schematic illustration of the Zeeman effect, portraying the split of the energy levels depending on the spin's new orientation in a static magnetic field[2].

As seen in Figure 2.1b, depending on the orientation of the spins when the Zeeman-splitting occurs, Δm_I can either be -1 (parallel to B_0) or $+1$ (antiparallel to B_0). This phenomenon occurs in concordance with the quantum mechanical rule of selection, deriving into an equidistant energy level difference, as seen in the following equation.[2, 3]

$$\Delta E = \gamma \hbar B_0 \quad (4)$$

Most of them are parallel to B_0 since it is the more energy-efficient state, creating a noticeable macroscopic magnetization in this direction, as seen in Figure 2.1a.[2]

From now on the achieved macroscopic magnetization will be treated in classical physics terms (no quantum mechanical explanation) for clarity and simplicity, which is sufficient for the topics treated in this thesis. This macroscopic magnetisation is described in each direction by the following simplified Bloch equations.

$$\frac{dM_x}{dt} = \gamma(M_y B_0 - M_z B_{1y}) \quad (5)$$

$$\frac{dM_y}{dt} = -\gamma(M_x B_0 - M_z B_{1x}) \quad (6)$$

$$\frac{dM_z}{dt} = \gamma(M_x B_{1y} - M_y B_{1x}) \quad (7)$$

The transition from lower to higher energy states of the spins can occur through irradiation or absorption of radio frequency (RF) waves with the Larmor frequency (B_1 is an electromagnetic field orthogonal to B_0), which is known as nuclear magnetic resonance (NMR). The Larmor frequency ω_L , is described by the static magnetic field in the subsequent equation.[5]

2 Theoretical Background

$$\omega_L = \gamma B_0 \quad (8)$$

A secondary coil, in/around the bore or on the patient, can create this high radio frequency (RF) pulse in a transversal direction to the static field, in order to manipulate the magnetisation. These waves flip the spin precession by 90° to the z-Axis of B_0 , shifting the spin energy weight while a precession movement around the axis is created, this shift occurs measurably more to a higher energy state. Even if these energy changes occur naturally in systems with a temperature higher than absolute zero. When the spins naturally fall back to their more stable lower energy state, they release electromagnetic waves in the Larmor frequency range. The fallback precession movement induces an alternating voltage with ω_L in the RF coil, which is then detected and processed in order to create an image.[3, 5]

The third magnetic field needed for a patient's three-dimensional scan is the gradient field. This field encodes the spatial information of the signal received by the RF coil through the generation of small spatially varying magnetic fields that influence the static magnetic field B_0 . The gradient coils are situated around the machine's bore, creating gradient fields that differ in strength and duration around the three principal axes. Thus, encoding the exact spatial positions of each of the measured signals. For example, on the z-Axis, the encoding is seen as predefined slices, while the x-dimension is encoded by frequency and the y-dimension by a phase shift. Thou the imaging slices can be done in any desired orientation.[1, 2]

2.1.2 Radiofrequency Coils

An RF coil is, in essence, a circular wire loop that is part of a resonant circuit, resonating at the Larmor frequency of the specific scanner and analyzed nucleus. The RF coil can be used, as mentioned in point 2.1.1, to induce or measure a change in the magnetic field. As the name indicates, a transmit (Tx) coil transmits an RF signal to the body, also known as excitation. On the contrary, a receive (Rx) coil detects changes in the magnetization of the body. In agreement with Faraday's law, macroscopic changes in a body's magnetization induce a measurable electric voltage in the circuit. Nevertheless, both coils are manufactured to operate at the same Larmor frequency. Furthermore, the two functions can be combined into a transceiver (TxRx) coil, capable of transmitting and receiving a signal.[6, 7]

A TxRx coil can be found around an MRI machine's bore. It is usually integrated as a so-called body coil in MRI at magnetic fields below 7T. At ultra-high fields (≥ 7 T), a large body coil can not be operated efficiently due to field inhomogeneities related to the short wavelength in the human body and increased radiation losses. For that reason, as well as for better resolution, noise reduction, and field of view (FOV), external (local) RF coils are often used, which are placed on or around the patient's region of interest (ROI). The detected signal is then forwarded to a receiver chain connected to an electronic network, where the signal is then amplified, digitized, and processed to a full MR image.[4, 7]

2 Theoretical Background

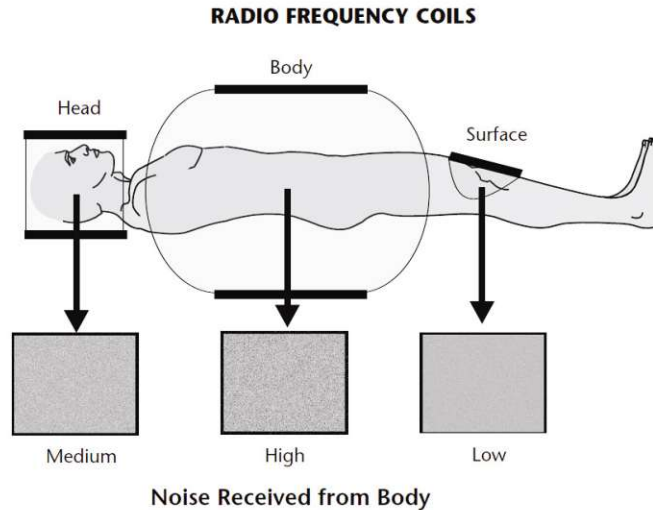


Figure 2.2: Schematic illustration of the types of RF coils used in MRI for each body location and their corresponding level of picked-up noise [3].

Besides the body coil inside an MR machine, two other main types of RF coils are found, surface and volume. Surface coils have a high sensitivity, but they lack a large FOV and do not penetrate very far into the body. They are usually used in the extremities and for high-quality images of concrete ROIs. On the other hand, birdcage coils (a type of volume coils) penetrate further into the body since it is placed around the body part of interest. The coil has two ports with a phase shift of 90° , working in tandem to increase the coverage and FOV with a homogenous field. Because of their tube-/cage-like structure, these types of coils are often used to get images of the insides on an extremity or to be used around a broad ROI like the head. In Figure 2.2, these three types of RF coils can be seen placed on a patient in their usual locations. The noise level, indicating the sensitivity of the coils, is also given, with increasing noise levels from surface to birdcage, to body coils. The whole general setup for an MR measurement on a patient can be viewed in Figure 2.3.[3, 7]

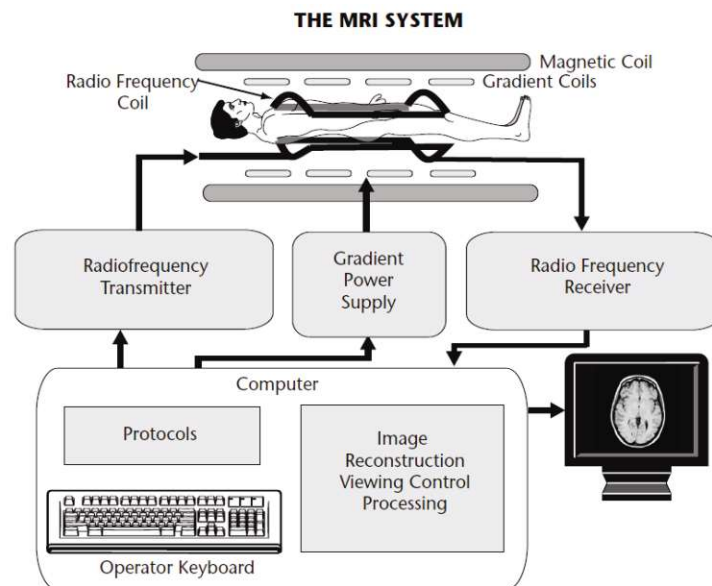


Figure 2.3: Schematic diagram of the major components of an MRI system [3].

2.1.3 Torso MRI

For the scope of this thesis, the portrayal of the human trunk is the main MR utility, comprising organs and tissues of the chest, abdomen, and pelvis. Torso MRI can be used to diagnose a variety of medical conditions such as cancer, heart disease, liver illness, and renal disorders, among many more. They are also being used to track these disorders' progression and assess the efficacy of treatments. Furthermore, images obtained by torso MRI can offer extensive information regarding organ and tissue size, shape, and exact location, as well as the existence of any abnormalities or damage. Of significant interest are the heart, liver, spine, and lymph nodes (in relation to breast cancer). The lungs can only be made visible by the use of special MR techniques since they are mostly filled with air.[8]

Since the torso is the most voluminous part of the human body, the ROI is large, in order to identify lymph nodes or view one of the vital organs as a whole. For that reason, the FOV should also be large, which would conclude that the body coil of the scanner should be used. Since a surface coil has a FOV that is too small. Nevertheless, the body coil has insufficient sensitivity and a large amount of signal to noise ratio for detailed observations (even at fields of 3T and below). To solve this problem, phased array coils are used [9]. These phased array surface coils maintain a high sensitivity due to their small diameter but reduced noise because of their small single FOV. Meanwhile, they increase the total FOV by covering the whole ROI with a mesh of overlapping sensitive coils. Another advantage of coil arrays is a potential reduction of the image acquisition time via parallel imaging methods. These methods exploit spatial information provided by coil element placing to reduce the amount of data needed to correctly generate the MR image. Additionally, the coils can be arranged in a form-fitting way since the modularity of the array makes it more flexible than a single coil. That way, the whole desired ROI can be covered in a single specialized coil that can be tightly fitted onto the patient's torso, as seen in Figure 2.4.[3, 6]

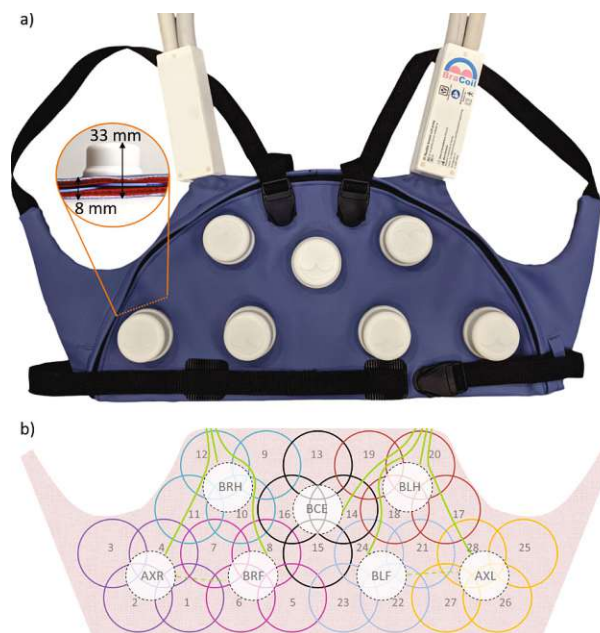


Figure 2.4: a) Photograph of a torso RF coil for breast cancer screening (BraCoil), made to be as flexible and comfortable as possible. b) Schematic view of the single coil arrays of the BraCoil [10].

2 Theoretical Background

Through this form-fitted coil array, a high-quality image of the patient can be obtained. Still, an emphasis should be put on image defects, artifacts, and loss of resolution through the involuntary body and physiological movement. Besides the natural restlessness of the patient during an MRI, of more significance are the breathing and cardiovascular motions, which can not be stopped voluntarily by more than a dozen seconds for breathing or not at all for the heart. In the case of the breathing motion, not only the lungs are concerned since the whole chest, as well as all the organs surrounding the lungs, get pushed around. These facts are of utmost importance for this thesis.

2.2 Signal, Noise, and Artifacts in NMR

As viewed in Figure 2.2, the noise level and, therefore, the image quality of an MRI is highly dependent on the used coils. Yet this is not the only factor that influences the image, other determinants are different tissue types, as well as the artifact-creating movement mentioned in 2.1.3. Furthermore, the excitation and gradient sequences of the MR scanner, which can be extremely customizable, also influence the image quality depending on the needs. These quality characteristics are schematically shown in Figure 2.5. All these factors will be discussed closer in the following subchapters.

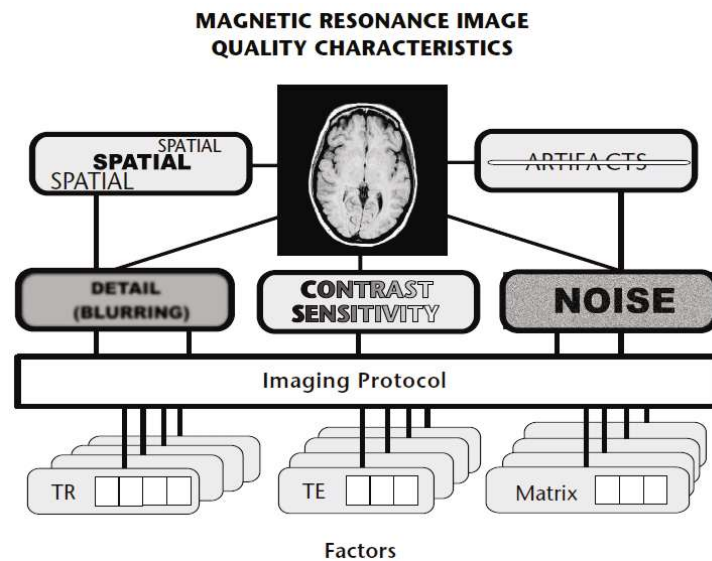


Figure 2.5: Schematic diagram of MR image quality characteristics influenced by the selection of protocol factors [3].

2.2.1 Signal in different Materials

As mentioned in 2.1.1, for the detection of a material, the nuclei of interest have to be excited with a specific resonance frequency. These excitations are induced by electromagnetic pulses of the RF coils, which can vary their phase, duration, or amplitude depending on their pulse sequences, influencing the flip angle of the precessing magnetization around B_0 . The excitation's characteristics influence the spin's relaxation process when returning to its equilibrium state. The relaxation times differ for every material, controlling the material-specific contrast value in an MR image. Furthermore, there are two types of weighting of relaxation times, T_1 and T_2 depending on which interaction process is weighted. Either spin-lattice or spin-spin interaction. These times are also known as longitudinal (T_1) or transverse (T_2) relaxation times.[3, 6, 11]

The spin-lattice interaction is the longitudinal relaxation of the magnetization, where they return to their original equilibrium position parallel to the z-axis of the static magnetic field. The time it takes for 63% of the original magnetization value to be recovered is known as T_1 . Tissues with a tighter and stronger ^1H lattice interaction between molecules have a longer T_1 , as shown in Figure 2.6 (top left), giving their name to this type of interaction.[1, 6]

2 Theoretical Background

The spin-spin interaction, also known as transverse relaxation, refers to the process by which the magnetization decays in the x-y-axis after being perturbed by an RF pulse. This is caused by the dephasing of the individual nuclei spins. This process occurs in a substantially shorter time than T_1 . T_2 relaxation time is described as the decay of the transverse magnetization to 37% of its original value, as can be seen in Figure 2.6 (bottom left).

Hard materials like bone are instinctively thought to not be visible in the MR scanner, which is valid for their hard mineral component since it does not contribute to the relaxation time. Nevertheless, bone's soft tissue component contains hydrogen atoms, as other hard materials do, and these very well contain sufficient ^1H to be measurable in MRI.[6]

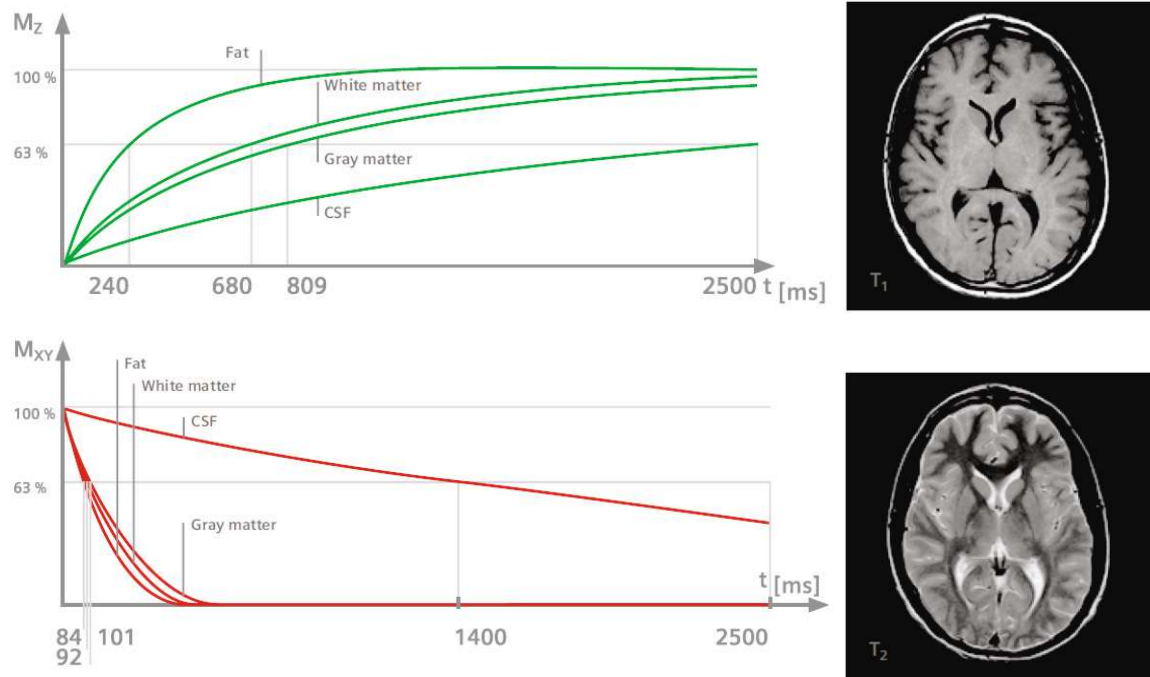


Figure 2.6: **Top:** Graph with magnetization relaxation percent on the y-axis and time frame in ms on the x-axis - **(left)** MR transversal Brain image - **(right)** of T_1 relaxation times according to the tissue [6]. **Bottom:** Graph with magnetization relaxation percent on the y-axis and time frame in ms on the x-axis - **(left)** MR transversal Brain image - **(right)** T_2 relaxation times according to the tissue [6].

In order to produce the curves seen in Figure 2.6 for new, untested materials, from which the T_1 and T_2 relaxation times can be determined, measurements have to be done. There are several available methods to define the longitudinal relaxation T_1 ; the most common one is the inversion recovery sequence. This sequence consists of an 180° inversion pulse, followed after a fixed inversion time τ by a 90° reading pulse. This pulse sequence can be seen on the left of Figure 2.7. As explained in the sections above, the 180° pulse inverts the magnetization from a precession in the positive z-axis to its opposite negative side. After some time, the magnetization returns to its original position by spin-lattice relaxation. After τ , the free induction decay signal is given through the 90° pulse, which produces a rotation in the xy-plane. This technique is then used for a whole series of different τ , each measurement divided in time by the recovery delay, which should be approximated to be larger than at least five times the expected T_1 to get at least a signal recovery of 98,5%. In that way, the spins can fully relax between measurement sequences. The results of the measurements can be put in a diagram of relaxation percentage by time and fitted to achieve a curve similar to the one in Figure 2.7. From this fitted curve, the T_1 time can then be determined with the 63% approximation mentioned above.

2 Theoretical Background

Several parameters can be adjusted to optimize the resulting curve, such as the pulse angle, detection mode, receiver gain, or recovery time. An emphasis is put on getting a resonance frequency matching the water molecules as closely as possible and adjusting τ to be lower than a tenth of T_1 . For this fitting, at least twelve measurement points are needed, achieving better results if more points are measured at the beginning of the curve.[11]

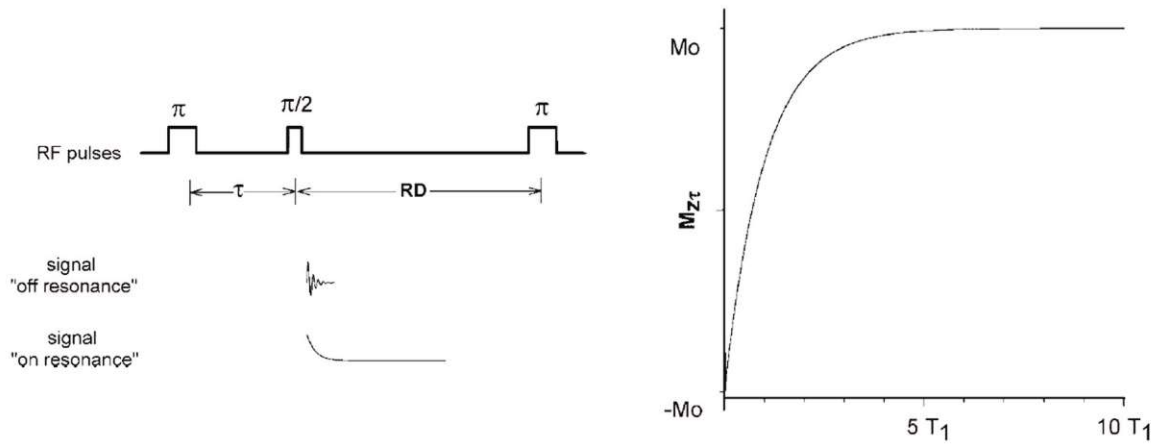


Figure 2.7: **Left:** Schematic of an inversion recovery pulse sequence. **Right:** Diagram showing an exemplary T_1 definition graph with magnetization relaxation percent on the y-axis and time frame in ms on the x-axis.[11]

To determine T_2 , a different approach has to be taken. In this case, the sequence starts with a 90° pulse followed by a series of 180° pulses throughout the whole decay of the signal. The 90° pulse excites the spins into a precession motion in the xy-plane, which starts a free induction decay determined by T_2 . After a specific τ , the 180° pulse flips the signal phase, letting an echo of the signal appear after 2τ , as seen in the left of Figure 2.8. For that reason, this pulse sequence is called spin-echo. The sequence of 180° pulses creates a succession of echoes of decreasing amplitude. This amplitude reduction is independent of inhomogeneities and disturbances and only determined by T_2 . The decay of the amplitudes can then be plotted as points again in a diagram of magnetization percentage by time and fitted to achieve a falling curve similar to the one in the diagram of Figure 2.8.

As for T_1 , several parameters should be adjusted to achieve an optimal measurement. These are also the receiver gain, the exact pulse angles, the resonance frequency, and even the number of scans and echoes done, which is beneficial to have a high quantity of them. The recovery delay is set the same way as for T_1 , but in contrast, τ needs to be very short, below 10 ms.[11]

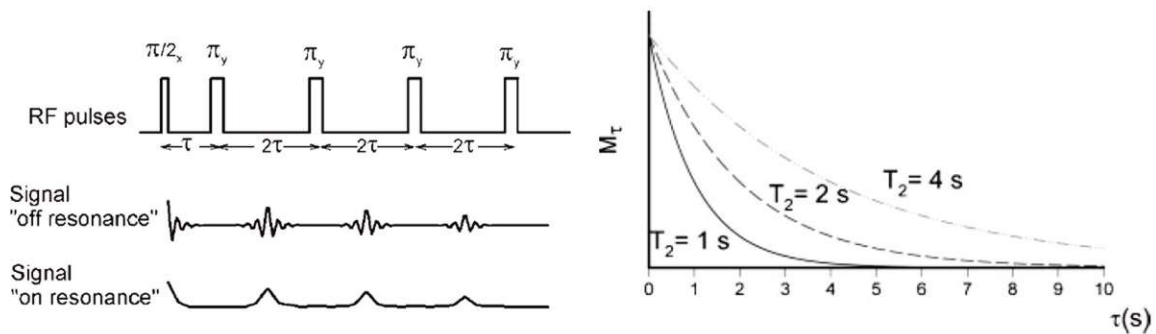


Figure 2.8: **Left:** Schematic of a spin-echo pulse sequence. **Right:** Diagram showing an exemplary T_2 definition graph with magnetization relaxation percent on the y-axis and time frame in ms on the x-axis.[11]

2 Theoretical Background

To summarize, T_1 and T_2 relaxation times are critical characteristics MRI utilizes to generate body pictures. T_1 relaxation is the rate at which magnetization returns to equilibrium, and T_2 relaxation represents the rate at which transverse magnetization decays. T_1 and T_2 relaxation times in various body tissues differ, which can be utilized to distinguish them in MRI pictures, e.g. fat has a lower T_1 than water but a higher T_2 . Considering these two-time measurements, the contrast can be enhanced for the specific imaging needs, as shown in Figure 2.6 (top right and bottom right).[2]

When considering how relaxation mechanisms affect the magnetization, the Bloch equations are adapted to describe the perturbed magnetization falling back to their equilibrium states. These interactions can be seen in the following equation, relating the first two to the x-y-axis and, therefore, T_2 and the last to the z-axis, therefore T_1 . [2]

$$\frac{dM_x}{dt} = \gamma(M_y B_0 - M_z B_{1y}) - \frac{M_x}{T_2}, \quad (9)$$

$$\frac{dM_y}{dt} = -\gamma(M_x B_0 - M_z B_{1x}) - \frac{M_y}{T_2}, \quad (10)$$

$$\frac{dM_z}{dt} = \gamma(M_x B_{1y} - M_y B_{1x}) - \frac{M_z - M_0}{T_1}. \quad (11)$$

For the reasons mentioned above, as well as for its high availability, water is the most commonly used substance to do MRI tests with. Usually in combination with salt or other additives like contrast agents, to get a more conductive solution with higher contrast and signal. It furthermore possesses good visibility in both its relaxation times. If the substance needs to be less liquid, a watery gel can be mixed through the addition of agar, ethylene glycol, or other viscosity-increasing compounds. These compounds, alongside the other widely used liquid oil, are shown imaged by an MR in Figure 2.9. On the other hand, materials like plastics and acrylics used to encase the imaged test liquid or substance are viewed as black in the scan. Meaning that they do not produce any signal since they lack ^1H nuclei, appearing as signal less as air.[1, 2]

2 Theoretical Background

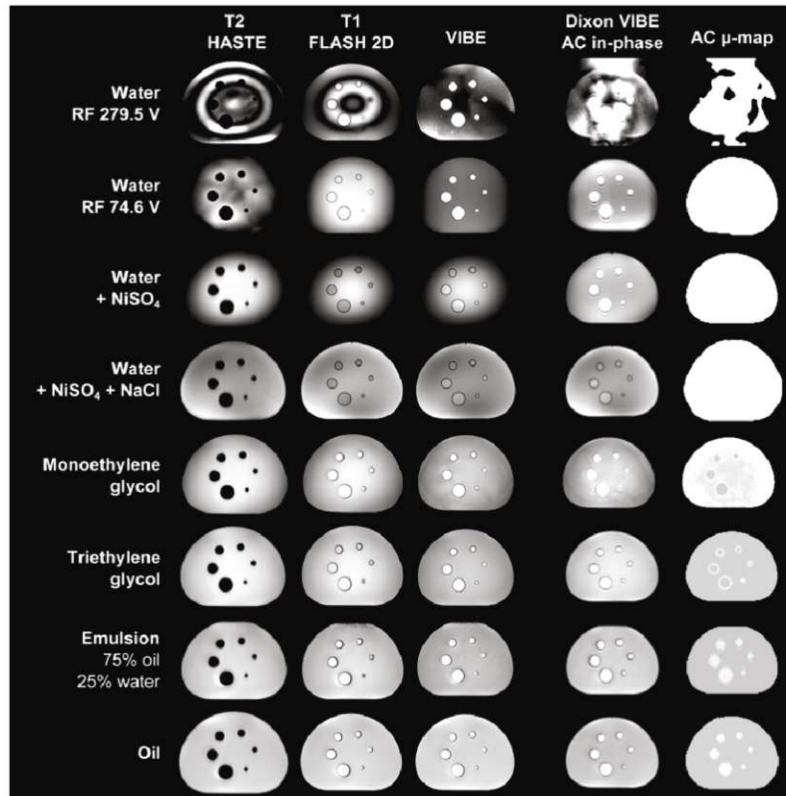


Figure 2.9: Tabular evaluation of different phantom fluids (rows) tested for PET/MR with different MR sequences (columns) [12].

Further parameters that can also influence T_1 and T_2 , besides the measured substance, are sample volume, temperature (ideally 37°C), and sample position in relation to the bore of the MR. Along with the sequence parameters that can be programmed for the scanner, like readout bandwidth, pulse angles, or recovery delay. Together with the adjustment of the inversion delays for T_1 or the half echo time for T_2 . In addition, several measurements are done on the same sample to ensure no changes regarding relaxation times over the measured period.[11]

Moreover, new advances in pulse sequences have enabled the imaging of tissues with very short relaxation times through the use of ultrashort echo time (UTE). Echo time (TE) is the period between an initial excitation of protons in tissue and detecting the MRI signal. The TE for a standard MRI sequence ranges from a few milliseconds to tens of milliseconds. The TE in UTE time sequences is substantially shorter, often ranging from a few microseconds to a few milliseconds. Tissues with short T_2 relaxation durations, such as bone, tendon, and lung, produce rapidly decaying signals that are challenging to record using common MRI pulse sequences. These signals are caught by UTE pulse sequences, making it feasible to image tissues that were previously difficult or impossible to detect with MRI [13, 14]. To capture the tissues with very short T_2 with even higher sensitivity and specificity, zero echo time (ZTE) sequences can be applied. As the name indicates, ZTE has an echo time of precisely zero, meaning that the signal is captured before any echoes have a chance to be formed, just after the RF excitation pulse is applied.[14, 15]

These two methods enable the visualization, with high spatial resolution, of cartilage in joints or lung tissues. Which can have significant clinical implications for the diagnosis and monitoring of, for example, musculoskeletal and pulmonary diseases like osteoarthritis, emphysema, or fibrosis.[14]

2.2.2 Material-induced Noise and Artifacts

Most imaged materials and subjects are of organic composition, as already mentioned. These can have better or worse signal qualities (proton density, relaxation times) but usually do not create artifacts themselves. As stated above, non-organic materials like plastic or air pockets are seen as signal-less by the scanner and, therefore, black in the image. These black surfaces are sometimes regarded as artifacts if they obscure tissue or fluids around them. This is notoriously common for air bubbles in liquids or the air-filled pockets of the body, like the lungs. These artifacts, as well as all other types of artifacts, tend to reduce the quality of the examination or even be confused with a non-existing pathology. For that reason, it is essential to identify and understand these artifacts and their sources to minimize their influence in the scanned image and, consequently, in the diagnosis.

Metallic objects found in patients, for example, prosthetics and implants, are known to experience movement, even if non-ferromagnetic or paramagnetic, through magnetic or Lorenz forces inside an MRI scanner. Diamagnetism may also play a role for non-ferromagnetic materials, inducing magnetic fields in the opposite direction of the applied magnetic field [16, 17]. The time varying gradient and RF fields can also induce heat through Faraday's law into the metallic part. These effects are of utmost importance for the safety of patients and medical personnel. These metals can not only be found on endoprosthesis or medical equipment but can also be remnants of surgical operations like surgical clips, which are easily forgotten by patients. Or even more likely to be seen as non-reactive are mundane accessories like hair ties, clothes/clothes labels, or even makeup [18]. Nevertheless, metallic objects can also induce artifacts in the images by inducing local inhomogeneities, which is another of the main reasons why most metals are avoided when constructing phantoms, test setups, or MR gear, accessories, and attachments. These artifacts usually make it impossible to see the surrounding of the artifact's source by obscuring its surroundings while appearing abnormally bright in the image (Figure 2.10) or, on the contrary, disappearing themselves too (Figure 2.11 **a./b.**). These artifacts are known either as pile-up artifacts, which form when some areas have an abnormally high signal, or suppression artifacts, which form when an area experiences signal loss. Sometimes the image outline is even spatially warped, known as geometric distortion, as in Figure 2.12 **b. c. e. and f.**. The size, shape, and type of metal influence the appearance and severity of the artifact. This makes ferromagnetic orthodontics very obstructive when imaging the head, while titanium implants are nearly non-disruptive due to their lower magnetic susceptibility.[16, 18]

2 Theoretical Background



Figure 2.10: MRI image with an anterior distorted cruciate ligament reconstruction on a knee's sagittal plane using stainless steel screw. The image is highly distorted in its quality due to an artifact originating in the screw.[18]

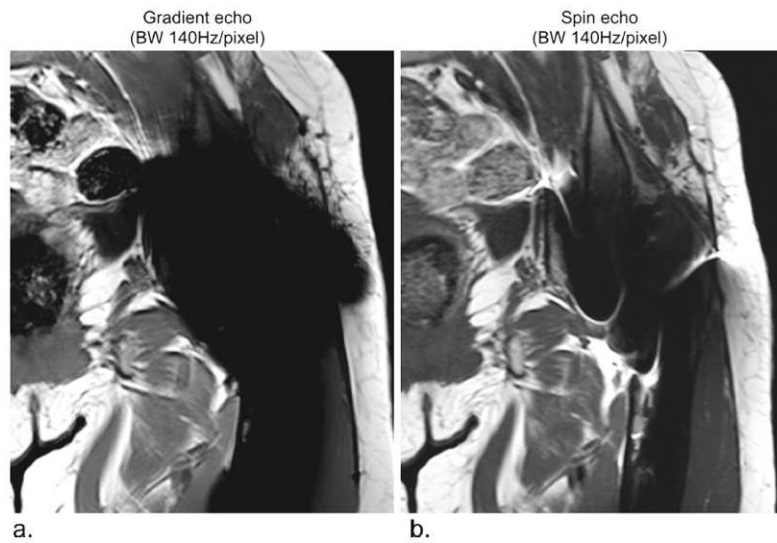


Figure 2.11: Comparison of a 50-year-old male patient's left complete hip replacement (Cr-Co) coronal MR image with T_1 Gradient echo in **a.** and T_1 Spin echo **b.**. Although there are spatial distortions in the two pictures, the gradient-echo sequence **b.** exhibits a significantly decreased distortion signal.[16]

2 Theoretical Background

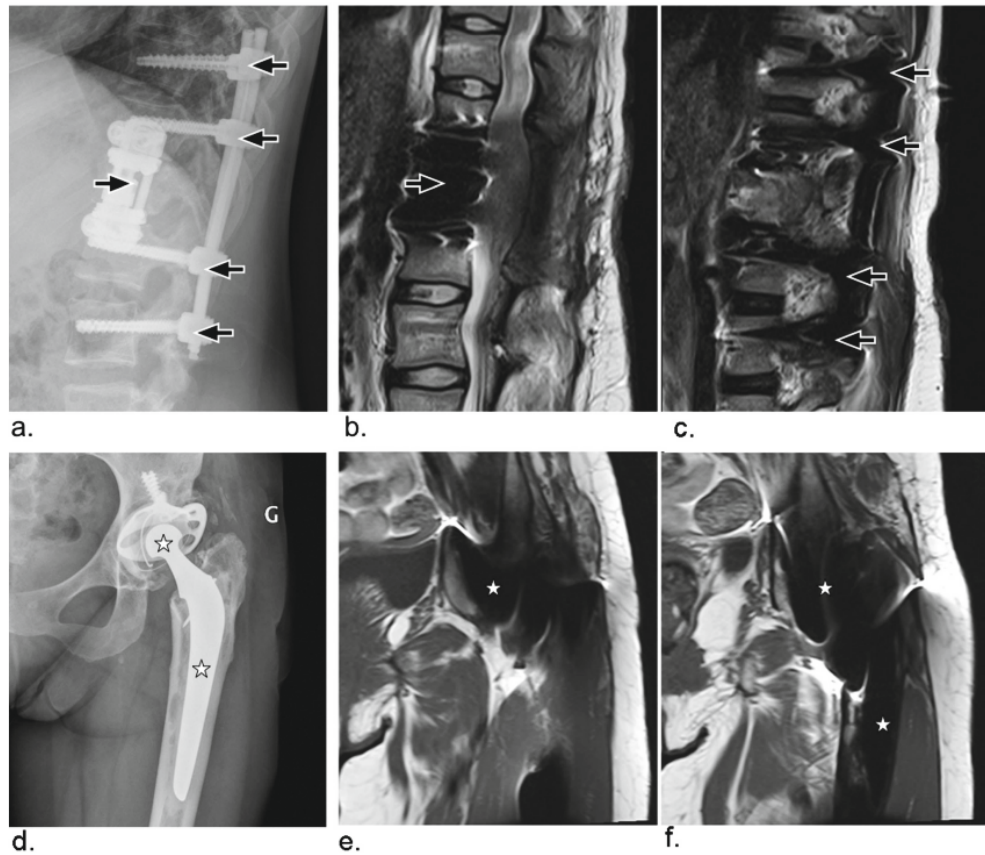


Figure 2.12: **a.** and **b.** show an MRI of the spinal cord (sagittal plane) and femur head (coronal plane) with endoprosthesis, respectively, imaged with UTE for best results. **b.** **c.** **e.** and **f.** show the same endoprosthesis imaged with standard sequences to show the induced material artifacts. Arrows and stars mark the landmarks of the endoprosthesis across the images. [16]

These artifacts originate from spatial encoding mistakes due to the high magnetic susceptibility of metallic items. The linearity between the connected space and frequency is lost, causing a spatial encoding offset error along the gradient's slope in the image. This means the signal is lost at one extreme of the metallic body, accompanied by a signal build-up in the front head of the error offset. This causes the mentioned pile-up artifact. The magnetic field is locally stronger at the north and south poles and weaker at the extreme boundaries of the metallic object, where the same encoding error offsets are seen, but in this case, in the opposite direction to the gradient slope. This phenomenon results in the characteristic "boomerang" appearance created by a region of signal accumulation and signal loss, as is marked in Figure 2.13 **b.** by black and white stars, respectively. Figure 2.13 shows this phenomenon visually with an MR image of a metal-filled rod and a schematic explaining the induced magnetic currents that cause the artifacts. This characteristic artifact can be seen in a more complex geometry in Figure 2.14, where a hip endoprosthesis is imaged in an MR scanner. The "boomerang" shape of the artifacts is not as straightforward as in Figure 2.13 since they overlap all through the geometry. Nevertheless, the pile-up artifacts and the signal-less areas are clearly seen. For more clarity, they are also signified by black and white stars. The induced through-plane artifacts can likewise be seen in Figure 2.14 **c.** [16, 18]

2 Theoretical Background

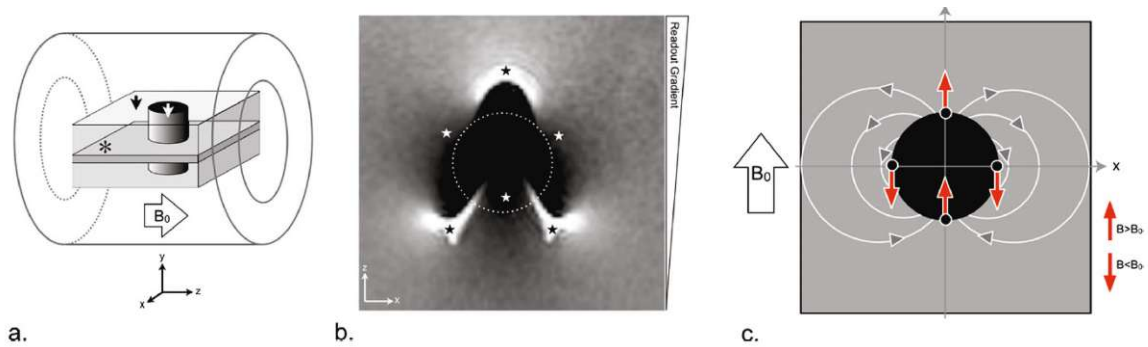


Figure 2.13: **a.**: Schematic of a metal rod (white arrow), surrounded by gelatinous water (black arrow), in the bore of an MR scanner, showing the static magnetic fields in the z -direction as well as the scanning direction and plane. **b.**: MR image of the metal rod described in **a.**, a dotted line indicates the actual position of the rod in space. Black stars denote signal pile-up, and white stars signal loss. The readout gradient is shown along the z -axis. **c.**: Schematic of the image shown in **b.**, with lines and arrows representing the direction of the induced magnetic field inside the metal rod, by the scanner. The red arrows show the direction of the highest field points, explaining the signal loss and pile-up.[16]

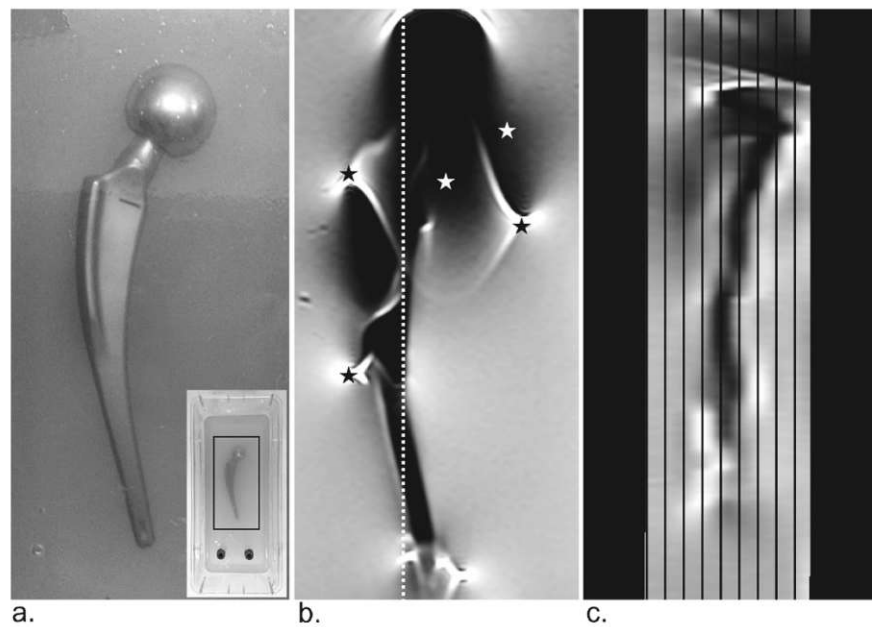


Figure 2.14: **a.**: Photograph of a cobalt-chrome alloy hip endoprosthesis suspended in a gelatinous agar-water mixture. **b.**: Coronal MR scan of **a.**, showing pile-up artifacts (black stars) and signal loss areas (white stars) **c.**: Sagittal image of through-plane artifacts across the dotted line seen in image **b.**.[16]

There are several ways and techniques to reduce metal-induced artifacts, like the use of spin echo (SE) instead of gradient echo (GE) since SE is less susceptible to inhomogeneities in the field. This difference can be viewed in Figure 2.11. Even more effective are shorter echo time sequences like UTE to avoid premature signal loss. Other available techniques are the increase of the gradient read-out bandwidth to reduce the in-plane artifacts in a straightforward manner, increasing slice selection bandwidth to lessen through-slice artifacts, or more complex fat suppression techniques. Furthermore, newer methods regarding the MR sequences used when scanned are started to be used, like multi-acquisition variable-resonance image combination (MAVRIC) view angle tilting (VAT) and slice encoding metal artifact correction (SEMAC). A closer explanation of the origin of these artifacts and the optimization methods of the sequence parameters to reduce them can be found in the following literature since they go beyond the scope of this thesis.[16, 18, 19, 20]

2 Theoretical Background

Another artifact source is electronic components since some patients with more critical or acute conditions require life-supporting machinery. This could be breathing aids or even an electrocardiogram (ECG). These machines can distort the measured characteristic frequencies of the tissues, inducing susceptibility artifacts and decreasing the image resolution. These electromagnetic interferences (EMI) could also be induced by electrically active implants like pacemakers. However, the danger of a malfunction of the implant induced by the scanner is more critical than the created image artifacts.[21, 22]

Lastly, other types of artifacts can likewise be found in MRI, for example: Scanner related artifacts, due to malfunction of the machine, coils, or post-processing; truncation artifacts, occurring near sharp high contrast delimitation; aliasing artifacts, which locate structures outside the FOV at the opposite end of the image; chemical shift artifacts, which appear as a high contrast band at lipid-water interfaces; spike noise artifacts, caused by static electricity from acrylic clothing materials, among others. Nevertheless, they are either less common or relevant when imaging or less critical for this thesis's scope.[18, 19, 20]

2.2.3 Motion Artifacts

One type of MRI artifacts that was not mentioned in 2.2.2 are motion artifacts. These are motion-induced errors due to patient transitional action, like overall muscle movement, breathing, cardiac movement, or fluid flow, as found in blood vessels. Furthermore, random non-controllable body movements, such as bowel movements or muscle twitches, can also influence the image. MA are, therefore, extremely common and of utmost importance for this thesis.[18, 23]

The patient's movement can cause blurring artifacts, also known as ghosting for more extreme movement, distorting the image by degrading the resolution or even causing a double image to appear in the final scan. This ghosting artifact can appear as a clear, less intense copy of the image for periodical movements and as incoherent blurred ghosting if the movement is less regular. In the case of more periodic motions, like breathing, the blur can also appear more unidirectional, creating banding artifacts. These named artifacts impede the visualization of details and reduce sharpness in the imaged structures. As can be seen in the image comparison of Figure 2.15, where the first image is less sharp and accurate due to peristalsis movement in the lower thorax.[1, 3, 18, 23]

2 Theoretical Background

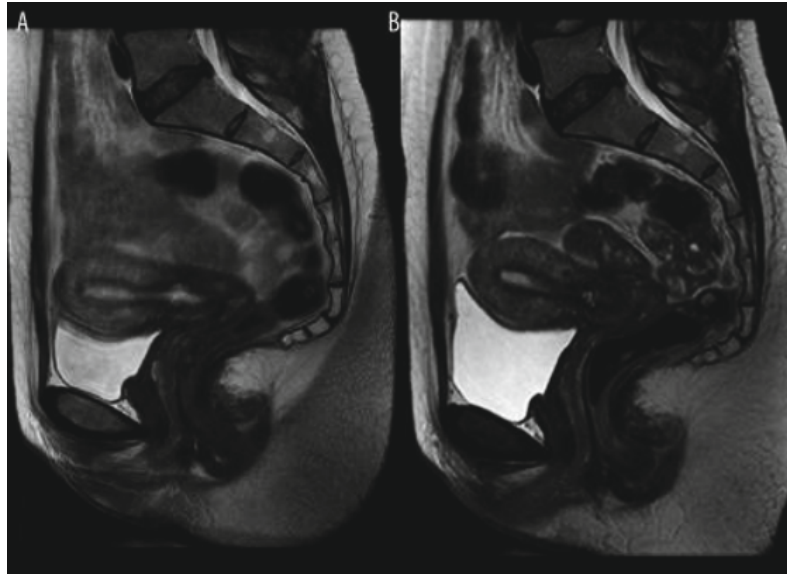


Figure 2.15: MR image in the sagittal plane of the pelvic region. **A:** Motion artifacts like banding and blurring can be observed due to peristalsis. **B:** Same imaged region as **A** but with fewer motion artifacts for comparison.[18, 23]

The caused image blur originates from a location shift of a signal voxel to another neighboring voxel, creating smears in the image. For that reason, the direction of the movement with respect to the read or slice direction of the scanning further influences the artifact's severity. The motion can influence the scanning procedure in several different ways, in contrast to other visualization methods like photography, where artifacts simply occur when the portrayed object moves during the sampling time. This causes some features in the picture to be sampled twice or not at all. In the case of MR, a similar phenomenon can occur if movement is done between the excitation pulses targeting the same ROI. This generates a high image quality overlap with blurred neighboring regions, as seen in the schematic of Figure 2.16.[1, 3, 24]

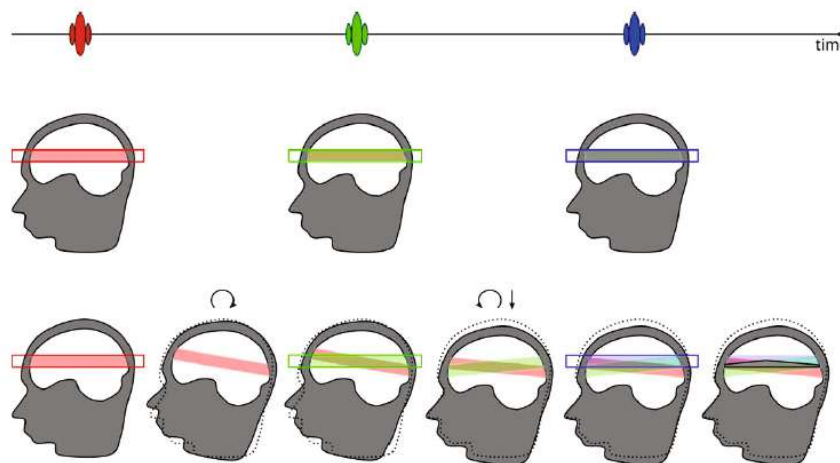


Figure 2.16: Schematic of pulse excitation on brain MRI. Three different pulses excite the same brain region over time, fully overlapping in the top row to create a high-quality image. The bottom row shows how the overlap can move through rotational and translational movement between each pulsation step. This creates a small region of total overlap, with the rest only partially overlapping or being recorded by just one excitation pulse. Which generates blurring, ghosting, and banding artifacts.[23]

Yet other error mechanisms due to motion can also influence the image, like the dephasing of nuclei spins when moving in the same axis as the gradient fields. This causes variability in phases for the same ROI creating inconsistencies in the k-space and, therefore, data

2 Theoretical Background

corruption in the image. The k -space, or Fourier space, can be further distorted by a movement against the k -space sampling trajectory, like rotation for a rectilinear sampling. Other sampling schemes like radial or spiral can decrease the artifacts at high contrast edges if it starts at the peripheries of the k -space. However, it cannot overcome all artifacts, only change their type, location, or relevance. Being able to acquire information from large areas with each acquisition makes it more robust against motion and flow but more susceptible to magnetic field disturbances. Since the k -space relation to the image pixel is not singularly defined, meaning that an intensity change in a pixel can affect the whole k -space and vice versa. Nevertheless, data corruption at the center of the k -space induces more critical artifacts than corruption near the periphery. A simulation of movement severity increase for different types of k -space acquisitions can be seen in Figure 2.17.[1, 6, 23, 24]

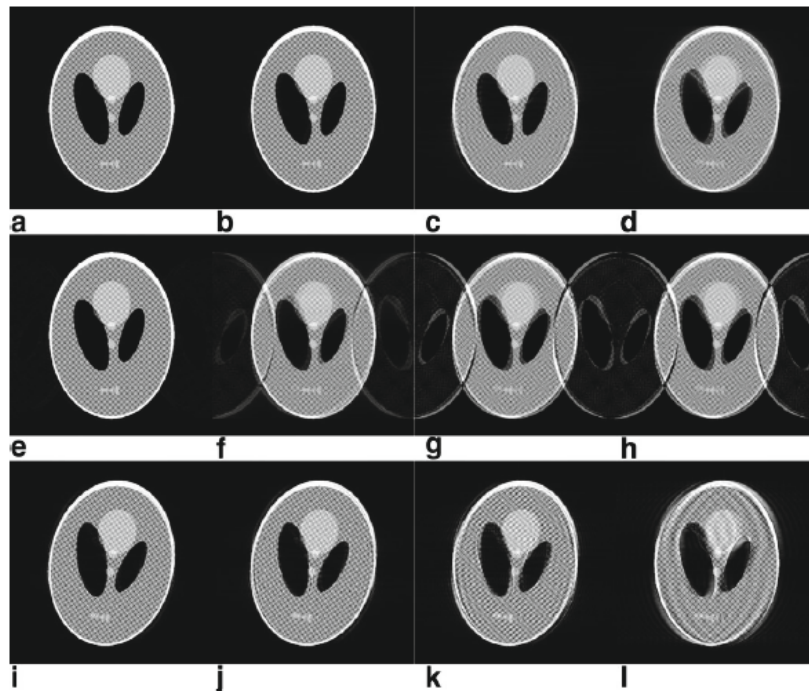


Figure 2.17: MRI simulated images of an anatomic phantom. The level of recorded inconsistencies increases with every column from 12,5 % to 25 %, 37,5 %, and 50 % inconsistent data. The linear k -space acquisition is used for the first row and the two-shot interleaved acquisition in the middle row. The bottom row is the centric reordering of the middle row with an increase in data inconsistency from 50% to 62,5 %, 75 % till 87,5 %.[23]

As already seen, not only the signal readout process can be hindered by motion, but also the signal generation within the pulse time can be modified by movement. Even motion that is not inside the ROI can affect the image by affecting B_0 inside the bore due to the magnetic susceptibility of the field. Likewise, the B_1 fields could change due to body position displacement or positional shifts of the RF coils with respect to the body. All these interactions make the patient's motion one of the major quality-reducing and artifact-inducing factors in MRI. Explaining why so much effort is put into reducing its influence and making it the end goal of the research that this thesis is part of. Further measures to minimize movement during the scan, lessen its impact when data is acquired, and increase quality posteriorly are described in Section 2.4.[3, 23, 24]

2.3 Imaging Phantoms

Phantoms are specialized items or equipment used in the medical imaging sector to represent human tissues, organs, or whole-body sections. Phantoms can be tailored to specific imaging modalities such as X-ray, CT, ultrasound, or MRI. They may include anatomical structures, realistic tissue textures, or dynamic elements representing physiological motion. The imaging method, body part, and the individual application or research goal determine the type of phantom used.[25]

Overall, MRI phantoms are significant tools in medical imaging for a variety of applications since they enable quality assurance, calibration, standardization, education, and innovation in the sector. They contribute to improving MRI examination accuracy, repeatability, and safety, eventually leading to better results, refining patient care, and expanding scientific understanding in the area.[26]

2.3.1 NMR Phantoms

As mentioned above, there are specific phantoms for each imaging modality, with different limitations and purposes. MRI phantoms are composed of materials that have magnetic resonance characteristics similar to human tissues. Examples of these materials are water-based solutions, gels, and other compounds that may imitate the relaxation times and signal properties found in the human body. They can simulate the qualities of tissues in the brain, blood vessels, tumors, and other biological structures. Phantoms may also be used to evaluate motion artifacts by including processes replicating physiological motion during imaging. Ferromagnetic materials must be avoided at all costs since they can cause damage to the machine and harm to any patient or medical personnel around it. This is due to the strong constant B_0 magnetic field that is always present in the scanner and can impose high movement velocities on the magnetic objects. The gradient magnetic fields can also further move or heat the objects up due to induction. Even non-ferromagnetic metals should be avoided, as they cause artifacts, as explained in more detail in section 2.2.2.[3, 25, 26]

MR phantoms have several uses, one of the main ones being quality assurance. Therefore, being used to evaluate and assure the accuracy and signal-to-noise ratio of MRI scanners. Operators can check the resolution of the images, detect artifacts, and ensure that the MRI scanner is operational by imaging the phantom. Furthermore, operators can calibrate the scanner settings and sequences using phantoms with known homogeneous relaxation durations and signal intensities. A calibration phantom with different samples that possess specific relaxation times can be seen in Figure 2.18. This calibration can also be done for equipment such as motion monitoring or other scanning add-ons.[2, 3, 26]

2 Theoretical Background



Figure 2.18: **a:** Photograph of a vial filled with an MR-based biomarker. **b:** Multiple different vials placed in a phantom holder filled with deionized water. **c:** The MR-based biomarker solution for each vial can be estimated using MRI. In this example, values are (beginning at the 12 o'clock position and moving counterclockwise) 0, 5, 10, 15, 20, 30, 40, and 50%.[26]

In addition, MRI phantoms are extremely useful research tools. They make it possible to simulate specific clinical settings, evaluate new imaging algorithms, and validate innovative MRI technologies. They are also being utilized to create and improve novel MRI pulse sequences. Where researchers can utilize phantoms to assess the efficacy of alternative imaging sequences and replicate certain tissue features or diseases. This helps to improve imaging techniques and protocols in a controlled environment before they are used on patients in clinical trials.

2.3.2 NMR Motion Phantoms

Motion phantoms (MP) are used to imitate and research different forms of motion seen in clinical MRI imaging, such as respiratory motion, cardiac activity, and movement related to other organs or anatomical structures. As mentioned above, they are used to investigate and refine imaging techniques, analyze motion artifacts, and develop motion correction algorithms. An example of such a motion phantom can be seen in Figure 2.19.[27]

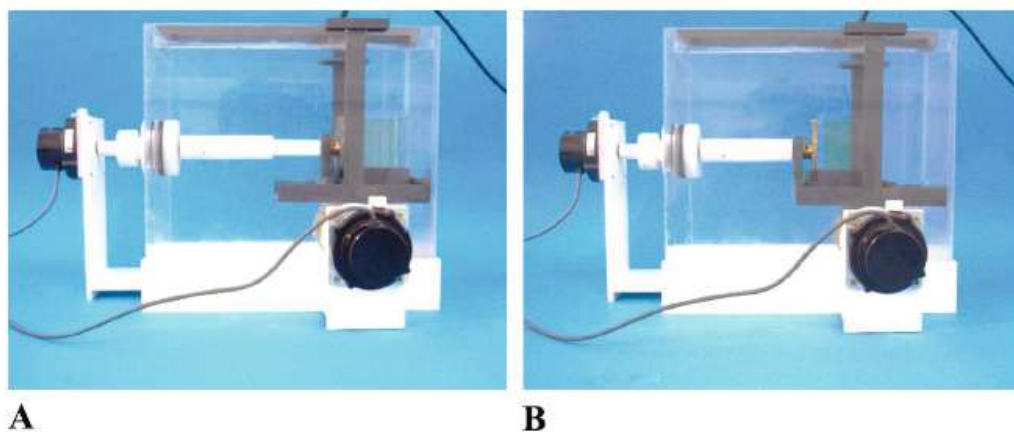


Figure 2.19: Photograph of an MR motion phantom, which can convey movement to an MR-visible phantom cube, in the X-axis (from left to right in the Figure). **A:** extended telescopic shaft. **B:** collapsed telescopic shaft.[27]

2 Theoretical Background

In order to mimic the respiratory motion caused by the patients' breathing, such as breast expansion and contraction or inner organ compression, mechanical systems consisting of flexible material are used. Cardiac motion is similarly achieved, just in a more pulsatile movement pattern. Achieving this motion through motors or hydraulic/pneumatic systems is the main challenge since these have to be either non- or low-magnetic to function without interferences in the scanner room.[27, 28]

Moreover, there are also dynamic phantoms, which are used for imitating dynamic processes or changes in the body that occur over time. The most common type of dynamic phantoms are perfusion phantoms. These replicate blood flow and contrast agent distribution via vessels. They are frequently made up of fluid-filled tubes or vessels with specified geometrical forms. Researchers can analyze perfusion imaging techniques, confirm quantitative perfusion measures, and explore the influence of parameters such as vascular shape on perfusion analysis by adjusting the flow rate and implementing contrast agents.[26]

Motion and dynamic phantoms require thorough engineering to recreate the intended movement processes correctly. They may employ mechanical systems, flexible materials, fluid dynamics concepts, or a combination of these.

2.3.3 NMR Phantom Manufacturing Techniques

MRI phantoms are manufactured utilizing various procedures and materials to imitate the qualities of human tissues and organs. The phantom's desired qualities and applications determine the particular manufacturing technique and materials used.

The most widely used phantoms are water-based ones. They are made of distilled water combined with various additive concentrations to tune the signal intensities, electromagnetic properties, proton density, conductivity, and T_1/T_2 relaxation times. Salts, like NaCl or $MnCl_2$, and paramagnetic substances, for example, gadolinium-based contrast agents, are common additions. Tuning, for example, the conductivity of the phantoms can have severe changes in their utility and how well they are adapted to be perceived by RF coils. The phantom's material can also be modified in its consistency if needed. This can be done by mixing water with various chemicals to get the necessary tissue properties. Agar, gelatin, silicone, and polyvinyl alcohol are all common ingredients for this purpose. Additionally, contrast agents can also be combined to simulate the behavior of tissues where contrast enhancement is needed.[26]

These phantoms can also be designed to mimic the shape, structure, and composition of certain body parts or organs. Standard engineering manufacturing techniques can be employed, emphasizing polymer usage. Due to its optical and mechanical characteristics, a widely used material type is acrylic, which is often heat bent to create more natural shapes and plastic welded to make water-tight recipients. For silicones and rubbers, molding and casting processes can be used to achieve desirable results. Furthermore, these phantoms are frequently built utilizing additive manufacturing techniques. Medical imaging data, such as CT or MRI images of real patients, may be used to generate 3D models to get anatomically realistic geometries. The phantoms can then be printed using materials that closely approximate the anatomical characteristics of interest, such as thermoplastics, resins, or elastomers, which can then be filled with water-based compositions. There are even novel additive manufacturing materials that possess good MR visibility due to having liquid-filled

2 Theoretical Background

micro compartments inside them. A selection of commonly used materials for phantom manufacturing can be seen in Figure 2.20.[26, 29]

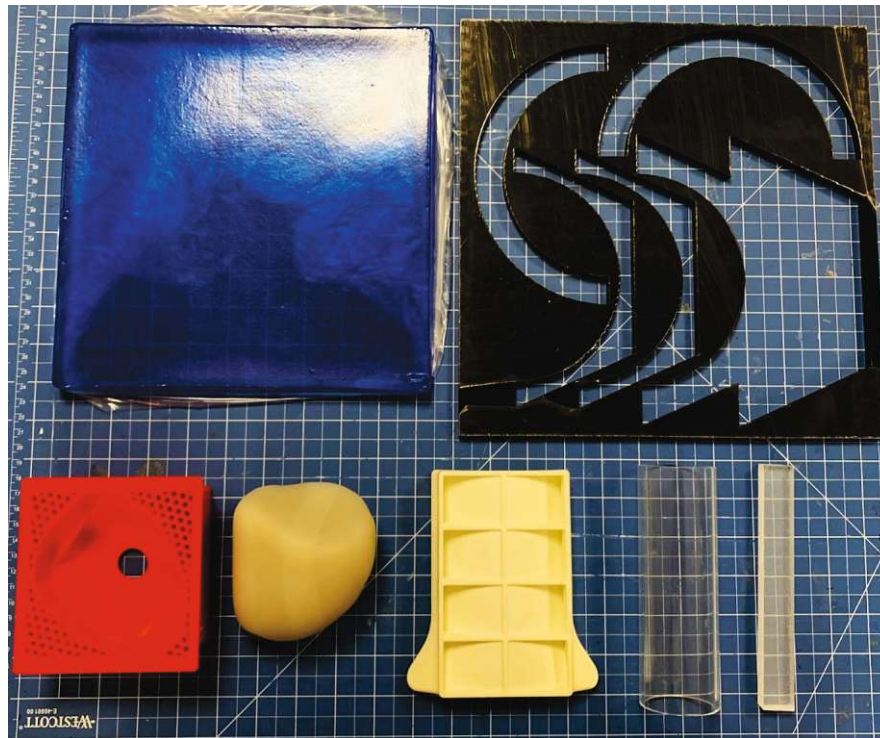


Figure 2.20: Photograph of a selection of commonly used materials in MR phantom manufacturing. Starting from left to right. **Top row:** Elastic polyurethane fiber pad (gel mat), polypropylene board. **Bottom row:** Polylactic acid (PLA) used in FDM printing, MR visible polymer used in SLA printing, polyamides (PL) used in SLS printing, Polymethyl methacrylate (PMMA/ Acrylic) in cylindrical or plate form.

MRI motion phantoms are manufactured utilizing specific procedures and materials to properly simulate physiological motion, varying by the type of motion replicated. Flexible materials like silicones, rubbers, and latex are used to achieve the freedom of movement required in the phantom. These flexible materials are able to respond to external forces and be deformed in a realistic way, mimicking the expansion and contraction that can be found during the breathing or cardiac cycle. In order to achieve these external forces that act on the motion phantom, several approaches can be utilized. The most common ones are pneumatic systems or non-/low-magnetic motors of different types. Pneumatic devices can inflate and deflate soft elastic bodies to replicate respiratory/cardiac motion, as well as actuate pistons in mechanical systems to mimic pulsatile actions. Fluid-filled tubes or vessels can also be used to imitate blood flow in the case of dynamic phantoms. This air or gas flow is controlled by valves or pumps in these systems, which can be placed outside the scanner room. Placing the systems outside the scanner room is a big advantage since metal parts can then be present. As stated above, the biggest limiting factor for these movement-inducing equipment is metal parts' avoidance. This is non-trivial, considering there is a heavy reliance on metal for engineering. Metal bearings, springs, screws, and other normed parts must be replaced by non-metallic counterparts.[26, 27, 28]

It is necessary to highlight that the production of MRI motion phantoms is a specific subject that involves knowledge of engineering, material science, and imaging physics. Making MRI phantoms requires careful material selection, exact additive measurements, and controlled

2 Theoretical Background

mixing procedures. The developed phantoms have to be subjected to validation and quality control procedures. This involves testing the phantom's motion accuracy, evaluating its electromagnetic characteristics, and guaranteeing its endurance and stability over time as well as the precise geometric measurements of the intended duplicated tissue features.[27, 28]

It is important to note that the area of MRI phantom fabrication is constantly growing, with continuing research and development to produce increasingly realistic and complex phantoms. For now, there is not one single best MR phantom, just a good one to fit the specific problem or challenge as best as possible. Therefore, standardization approaches are tried to be achieved in the research community to optimize and simplify the phantom manufacturing and testing procedure.[26]

2.4 Motion Reduction, Measurement and Correction

As mentioned in Section 2.2.3, patient motion is one of MRI's most significant image-degrading sources. Motion is very common since patients have to try to remain still inside a tight, loud space (scanner bore) for long scan times (5 minutes up to 1 hour). Studies suggest that 20% of MR scans in US hospitals have to be repeated due to artifacts, one of them being motion artifacts [30]. These artifacts can obscure the view of small structures or defects from pathologies or even be mistaken for non-existing illnesses. This is true for most medical imaging modalities. Still, MRI possesses one of the most extended scan times as well as a particular Fourier-based acquisition of data, making it more susceptible than others.[23]

The simplest way to reduce motion artifacts is to reduce the patient's motion before it happens, either by immobilizing the patient or increasing their comfort during the scan, along with reducing the scanning time. This can be achieved by several procedures, depending on the patient's age and vitality, as well as on the measurement type. Table 2.1 lists several motion prevention techniques that usually aim to constrict the movement or help the patient remain still by themselves. Nevertheless, some of these methods decrease the patient's comfort in the bore, which could be counterproductive over a longer scan time. Also, the sedation of patients, overall, complicates the measurement and increases the risk for the patient. Therefore, not all these methods are always viable and do not totally prevent motion such as involuntary actions like breathing, cardiac or bowel motion.[23, 24]

Motion prevention	Artifact reduction	Motion correction
Training	Faster imaging	Navigators
Distraction	Insensitive sequences	Self-navigated trajectories
Feed and wrap (for babies)	Gradient moment nulling	Prospective correction
Foam restraints	Saturation bands	Retrospective correction
Sedation	Triggering and gating	
Bitebars/head holders	Phase reordering	
Breathhold		

Table 2.1: Table of motion artifact mitigation strategies classified by their type and application time during the image acquisition progress.[23]

Breath-holding is a standard technique used to reduce movement in MR acquisition phases under 30 seconds (which usually excluded high-resolution scans of larger anatomical areas). Even if not all patients (pediatric, geriatric, sedated, or critical) can hold their breath for the measurement, it is an easy way to prevent a movement that influences nearly all types of scans, with significant importance in thorax MRI. Nevertheless, as seen in Figure 2.21, when the breathing motion is nullified, the cardiac motion becomes more apparent, which can not be prevented. In these cases where motion can not be prevented, the artifact reduction and motion correction methods listed in Table 2.1 play an important role.[18, 23]

2 Theoretical Background

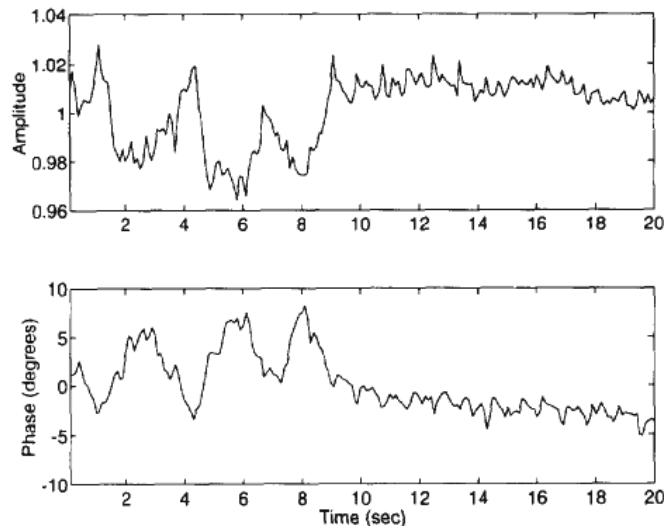


Figure 2.21: Two diagrams of the recorded movement of a patient inside an MR scanner. The X-axis in both diagrams is the time in seconds. A breath hold was done after about 9 seconds. **Top:** Y-axis is the amplitude of the motion in m. **Bottom:** Y-axis is the Phase change in degrees.[24]

Some of the artifact reduction techniques mentioned in Table 2.1 are not only targeted to motion artifacts but help with flow, FOV misalignments, or material artifacts, among many other issues. The easiest and most effective way to reduce the influence of motion in the image before or during the measurement is to reduce the measurement time through careful sequence choice. These sequences can be quicker, as well as less sensitive to movement. Examples of this short time of sequences are UTE and ZTE, already mentioned in Point 2.2.1.[2, 3, 18]

Further correction techniques can be applied if the desired resolution and contrast level in the scan is still insufficient due to motion. One of these techniques is the use of a navigator. As a navigator, it is usually meant using an added ultra-short sequence in the scanner during the imaging procedure that maps the location of the scanned body with respect to a reference over the imaging time. This recorded information can either be utilized prospectively or retrospectively.[23]

Prospective correction applies the real-time motion information to tailor the magnetic gradients and RF pulses to rectify the ROI position and maintain the data quality during the acquisition. Meanwhile, retrospective correction aims to improve the recorded data after the acquisition, either through the usage of navigator data or iterative algorithms. These methods try to undo the changes related to the patient's motion.[3, 23, 24, 30]

Alongside the high computational intensity of these methods, both of them usually rely on using tracking devices to get the patient's motion data, differing on the moment in time when this movement is corrected. The tracking can either be done by in-sequence navigators or external motion tracking systems. There is a variety of possible external trackers, such as stereo camera systems, ultrasound arrangements, RF probes, or on-patient motion sensors, among many others. Most of these approaches require something to be attached to the patient, either trackers or sensors, which could prolong the scanning time or increase the subject's discomfort. An approach that seems to solve some of these restrictions is the use of a Pilot Tone, which can record the patient's movement data during the scan in a wireless way, with just the need for an antenna being attached near the scanner's bore. In this approach, a signal close to the Larmor frequency is sent into the scanner and picked up by the RF coils. If the patient or the coils move, the signal's amplitude and coil load change due to alterations in

2 Theoretical Background

the path length between the coil and antenna. Through these alterations in the signal, the movement can then be measured simultaneously with the MR signal. This method can then help to do a retrospective motion correction (as is seen in Figure 2.22). More information on a similar movement recording technique, Beat Pilot Tone, which is being developed in parallel by the same research team as the motion phantom, can be found in the following reference [31]. The developed motion phantom is needed in order to prove, assess, calibrate and validate this and all other upcoming techniques without the use of patients in a regulated, tunable environment, with fixed, known motions, in a fixed time frame.[1, 3, 23, 24, 32]

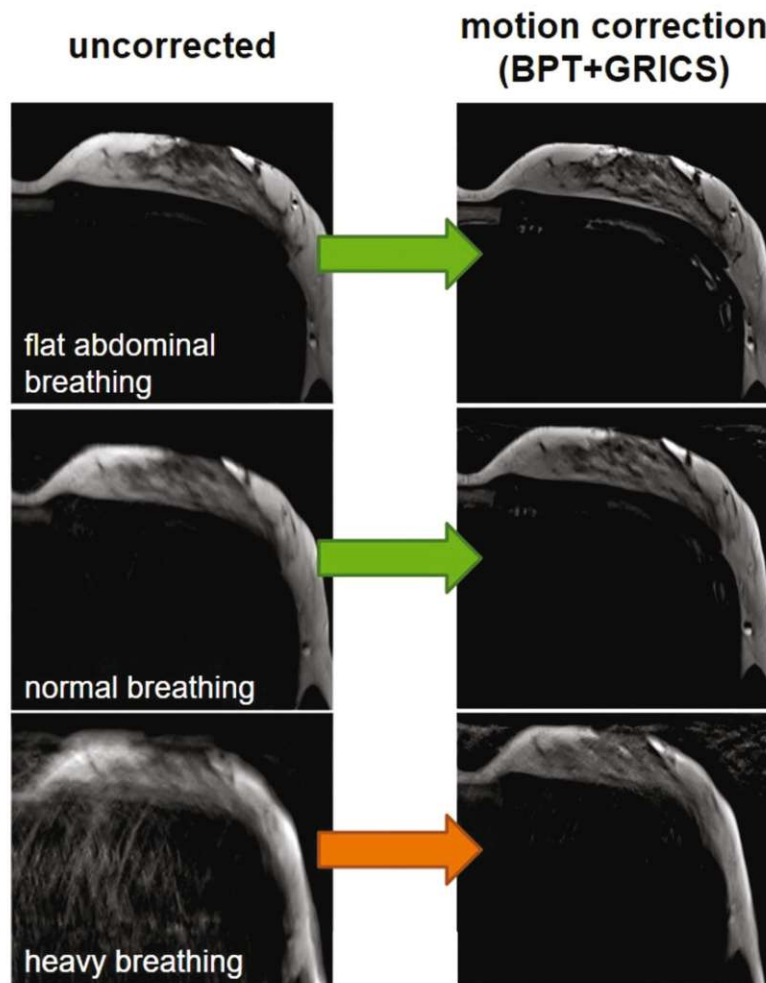


Figure 2.22: Comparison between MR breast scans with three degrees of breathing intensity, before and after the motion correction, with data acquired by the Beat Pilot Tone (BPT) system and corrected through generalized reconstruction by inversion of coupled systems (GRICS).

Since the mentioned motion and artifact reduction techniques by themselves have noticeable limitations, combining them is the most effective approach to achieve better scanning results. Given that, every imaging situation is unique due to the singularity of each patient, ROI, user, method, scanning parameters, and scanner. Therefore, it is convenient to have various suitable methods to choose from, to achieve precise data from which a more accurate diagnosis can be drawn.[1, 3, 23]

3 Phantom Design and Development

In the following section, the primary work of this thesis will be described. The developed MP is divided into modules with different functions or representing different body sections. Each module's requirements, design process (and iterations), as well as the manufacturing procedure and techniques, will be explained and reasoned.

3.1 Motion Phantom Overview

The aim of the development of the MP in this thesis was to create a torso-like phantom that is MR-compatible while mimicking the torso's cardiac and breathing motion in a simplified, defined manner. This precise definition of movement will then be used to investigate and validate new patient motion-tracking methods and devices, such as the aforementioned Beat Pilot Tone technique, which is a method that tracks the movement without on-patient hardware or special changes to the scanner.

3.1.1 Requirements

There are several requirements that the designed torso MP had to achieve. The first and most important characteristic was MR compatibility. The MP is not even permitted to enter the scanner room without good compatibility. This means that no ferromagnetic parts were allowed in the build, and preferably no metallic parts at all. Which highly constrained the phantom development. Following the material composition of the MP, the parts of the phantom that are in motion or simulate highly visible tissues which need to produce a strong signal to be seen in a standard 3T scanner. Related to the signal strength for T_1 and T_2 weighted images, it was desirable to have physiological conductivity values in the moving parts to better track the motion with the RF coils.

Geometrically the MP had to not only be able to fit in the bore of the scanner but have approximately the external measurements of an average human torso. Load stability must be reassured inside these geometric boundaries since a liquid-filled phantom can be substantially heavy. Along with a leak-free cleanable hygienic environment since this phantom is to be used in a medical MR scanner where also patients are tested.

Furthermore, the mechanical control of the MP had to be done in a non-/low-magnetic way on top of the patient's table or with the use of ferromagnetic parts from outside the scanner room. The created movement had to have enough strength to displace the phantom organs/tissues while being able to cover the desired distances and rates for breathing and heart motion. All this while keeping a mm accuracy range.

The final devised layout of the MP in the bore of the scanner with its external motors and its pneumatic and digital control outside of the scanner room can be seen in the Figure below.

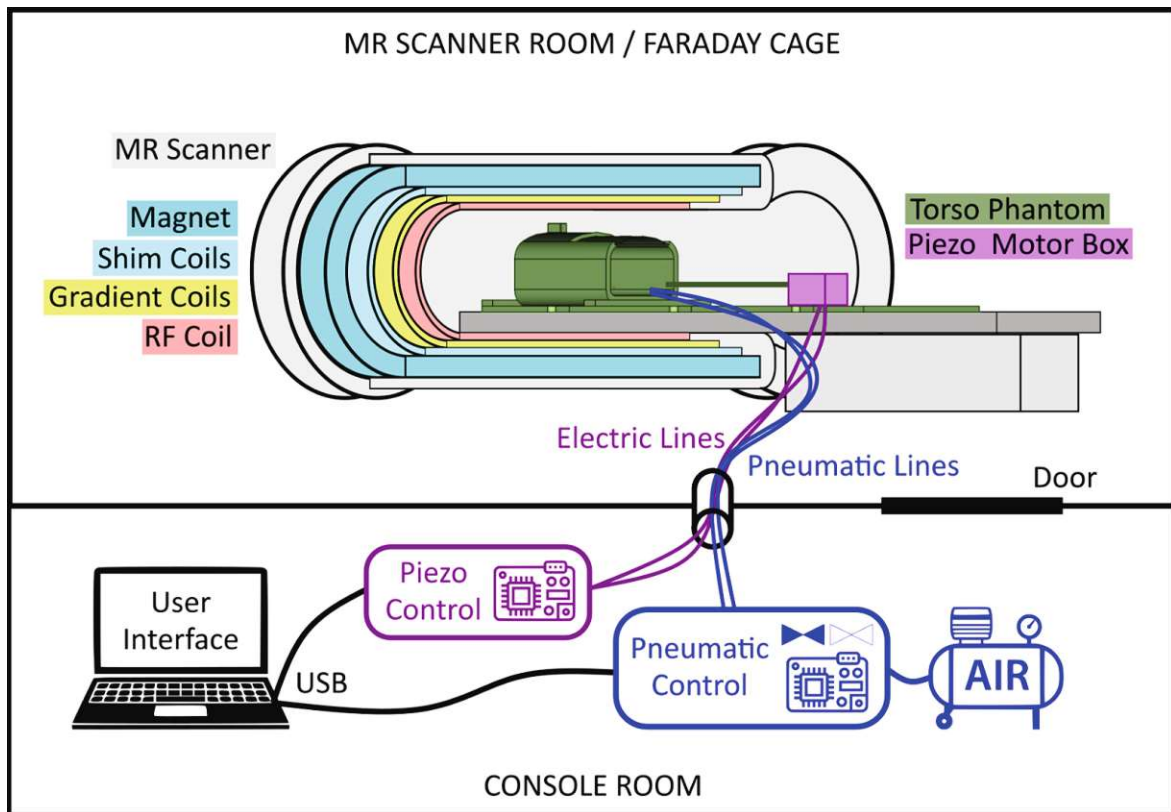


Figure 3.1: Schematic of the final devised layout of the MP with actuators in the scanner bore and controlling systems outside the scanner room.

3.1.2 Modules

The mentioned requirements can be achieved in various ways, depending on the approach and limitations encountered along the way. This is clear when seeing the evolution of the MP concepts at the start and end of the development process, as portrayed in the following images. Figure 3.2 portrayed a schematic of the MP before the process was started at the proposal stage. Figure 3.3 shows the MP at the start of the development, contrasting with Figure 3.4, which shows the final concept of the MP. These differences point out the iterative nature of hardware design.

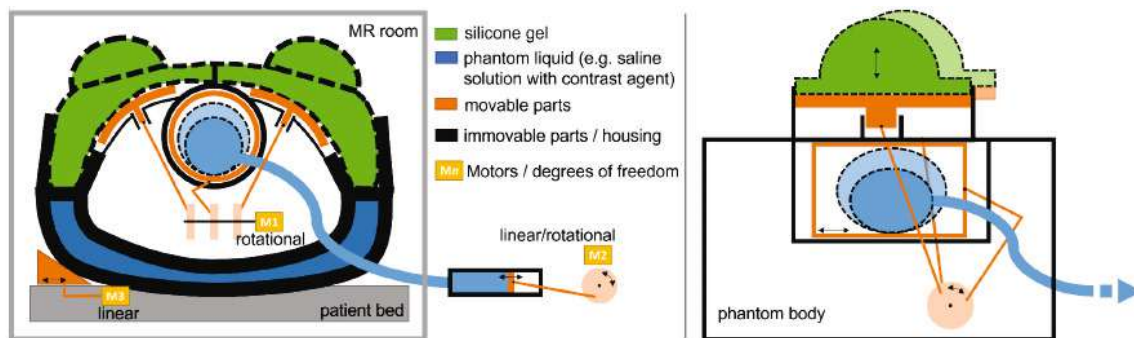


Figure 3.2: Schematic of the MP and its different modules and parts in a front (left) and side view(right) at the proposal stage of the phantom development.

3 Phantom Design and Development

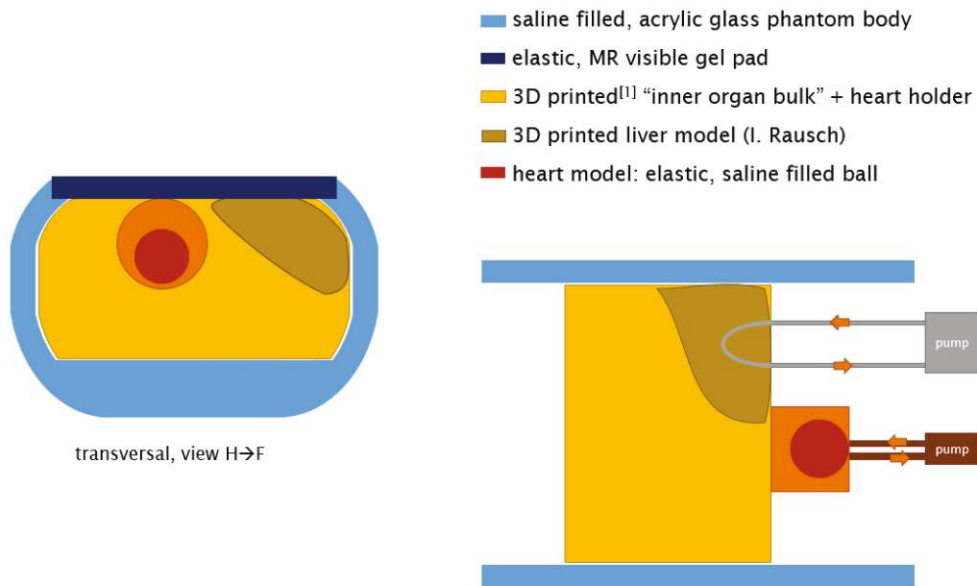


Figure 3.3: Schematic of the MP and its different modules and parts in a front (left) and top view(right) at the start of the phantom development stage.

The MP is divided into four primary modules, which can then be further subdivided. Additionally, external hardware and software are needed for the control and setup, as well as a plate where the MP and motors will be placed for stability, mount precision, and ease of carry. Nevertheless, as the MP, we will define the parts in the scanner bore, which simulate a human torso in shape, material, or movement. The four primary modules can be seen color-coded in Figure 3.4. The first module is the one that determines the outer geometry and holds all other modules in place. The Outer Shell can be seen as transparent in the Figure and is a double-walled acrylic shell with a watertight inner compartment and a large inner space for the other modules. The second module, seen as blue in the Figure, is the Chest Motion. This module comprises an MR visible gel mat, which is moved up and down by the head of a Gear Box that transduces the force and motion of the motors. This module simulates the patient's chest motion due to breathing. The third module simulates the abdominal organ motion, from head to toe, while breathing. This Abdominal Organ Bulk module is colored yellow in the Figure and consists of a monorail track and a bulk containing MR visible material and a liquid-filled liver mock-up for PET-MR studies. The last module is the Heart Motion, seen as red in Figure 3.4. This fourth module mimics the cardiac motion of the heart by shifting an MR visible additively manufactured heart with the help of a pneumatic cylinder. The Heart Motion module is attached to the Abdominal Organ Bulk to also experience the breathing motion on top of the cardiac motion.

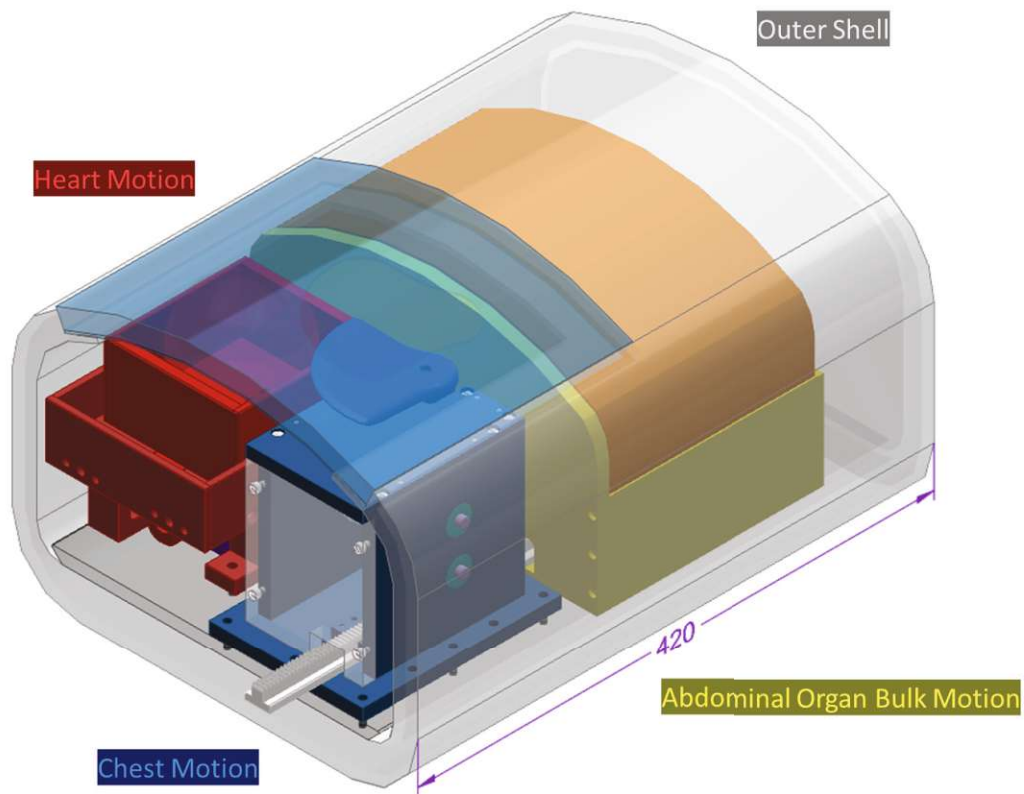


Figure 3.4: CAD render of the whole MP with length measurement in mm for scale, in isometric view. The main modules are color-coded for ease of identification. Gray/transparent → Outer Shell, blue → Chest Motion, yellow/orange → Abdominal Organ Bulk, red/violet → Heart Motion.

These modules will be further described in detail with explanations of the design selection, development, and manufacturing processes, in the following Sections.

3.1.3 Design and Manufacturing Tools

The design process of the modules and parts of the MP was usually started on paper for the first sketches, ideas, and dimensionalization. Nevertheless, the main design tool used in this thesis is the computer-aided design (CAD) program Solid Edge (by Siemens Digital Industry Software in its 2023 version). This program was selected due to prior experience while being one of the industry standard programs for technical CAD. This program was indispensable in order to make accurate three-dimensional (3D) parts for visualization as well as drafts for the manufacturing processes.

For most of the MP components, standard workshop manufacturing processes were used. The polypropylene and polyvinyl chloride (PVC) raw stock plates were machine cut, milled, or in the case of cylindrical parts like dowels, turned.

In the case of the Outer Shell module, acrylic manufacturing methods were used in order to get the curved double-walled watertight shell. Acrylic plates had to be laser cut, heat bent over molds of the desired curves, and chemically soldered to each other.

3 Phantom Design and Development

Additive manufacturing processes were also utilized in different ways while constructing the MP. Fused deposition modeling (FDM) printing was used to get prototypes of complex parts overnight. Besides, parts for experimental setups could be quickly manufactured, as well as variations of components to be tested. The material used in these prints was thermoplastic polylactic acid (PLA) due to its high availability, easy printability, and less brittleness compared to other FDM filament materials.

For parts in need of higher printing definition and accuracy along with water tightness, Stereolithography (SLA) was used. SLA also enabled the possibility of using a novel MR visible polymeric material. This material combines UV resin with a suspension of oil microcapsules trapped inside the hardened resin after curing [29]. When imaged in the scanner, these oil microcapsules convey a signal, making the material MR visible.

3.2 Outer Shell

3.2.1 Requirements

The Outer Shell (OS) module of the MP is defined as the form-determining and load-bearing outer structure that surrounds all other modules. Additionally, it should mimic the tissues surrounding the thoracic and ventral cavities. Meanwhile, the ample hollow space in the middle of the OS can be empty (i.e., not containing MR visible materials) since it is positioned roughly where the air-filled lungs would be in a human torso. This inner hollow space has to have enough room to encompass all other modules and have fixation points to mount them securely. Furthermore, this shell must be stable and hygienic and preferably see-through to more easily control the modules inside and identify any air pockets and changes in the filled saline solution. Good handling and resilience to the passage of time are also desirable. Lastly, a cutout and fixation sheet for the gel mat used in the Chest Motion (CM) is also required.

3.2.2 Design

In order to get a signal comparable to human tissue (e.g. skin, muscle, or fat layers) around the internal cavities, a double-layer wall with an internal space was foreseen. This gap between the walls is a watertight space that surrounds the whole circumference of the torso phantom. In this space, a distilled water solution containing salts, contrast agents, and T_1 enhancers, among other additives, can be filled to achieve a strong MR signal.

With this double wall design in mind, the general shape of the OS had to be determined. Therefore, an MR scan of the torso of an average-sized adult was used for reference (Figure 3.5). Considering this reference, as well as the limiting bore dimensions seen in Figure 3.1 and the requirement mentioned in section 3.2.1, a first model was designed in Solid Edge, which can be seen in Figure 3.6.

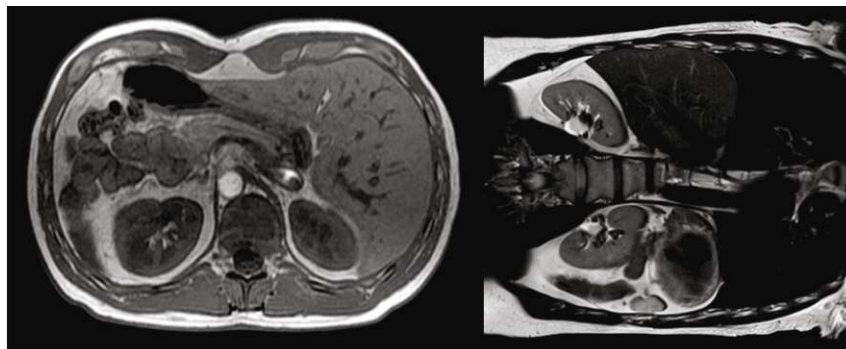


Figure 3.5: MRI image of an average adult torso used for reference for the MP. Superior (left) and lateral view (right).

3 Phantom Design and Development

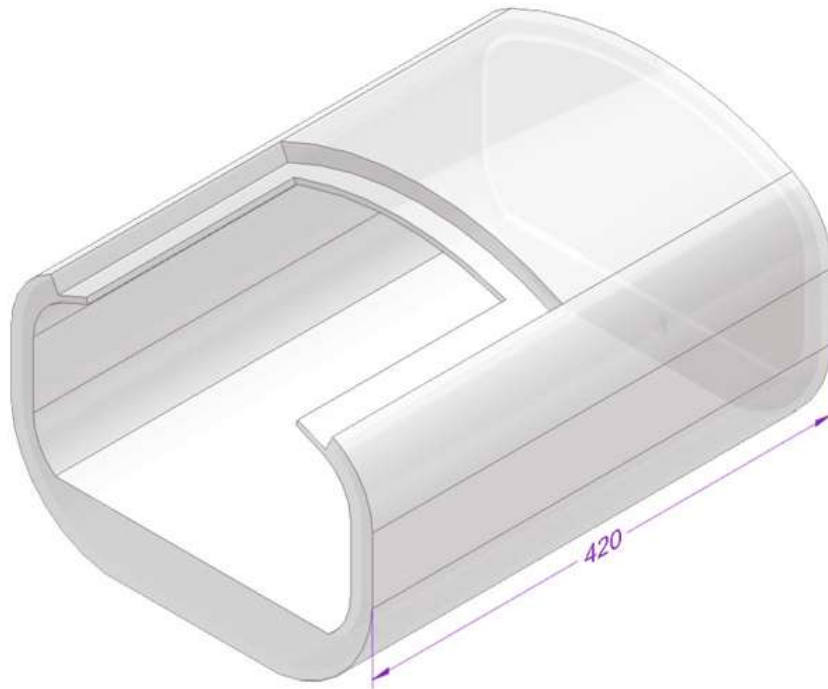


Figure 3.6: CAD render of the first OS version with its length measurement in mm for scale, in isometric view.

Several trade-offs were made in this design to optimally accommodate all features while still being able to manufacture the needed parts easily. The outer dimensions were kept at first, as much as possible, in line with the reference while smoothing out the curvatures and simplifying the forms for easier manufacturing. Considering that the material of choice for the walls was acrylic (further explanations in Point 3.2.3), a minimum wall thickness of 6 mm had to be chosen in order to maintain structural stability while keeping the thickness to a minimum. It was essential not to over-dimension the polymer parts in this build since they will not be able to generate a signal when scanned, appearing as black in the image. The water-filled interstice is modeled to be as thick as the stacking of tissues between the skin and thoracic cavity. The cranial opening of the double-walled shell is left open for ease of handling since the other modules have to be installed and actuated through this opening. In contrast, the caudal end is closed with a single acrylic board for rigidity and stability. This closing board also helps to keep the inner modules clean and dustless for longer storage times. This wall does not have to have an interstitial space since predominantly transverse slices will be imaged, and having a wide straight visible closure at the caudal end of the abdominal organs would not be anatomically similar.

Once the design of the other modules was started, it was noticed that a wider inner space with a flatter area was needed in order to accommodate all of them. Therefore, a second modified OS design was done, as seen in Figure 3.7. The height of the internal space was also increased by lowering the floor and therefore decreasing the outer curvature of the OS. This decreased the water layer at the bottom but also increased the phantoms' overall stability.

3 Phantom Design and Development

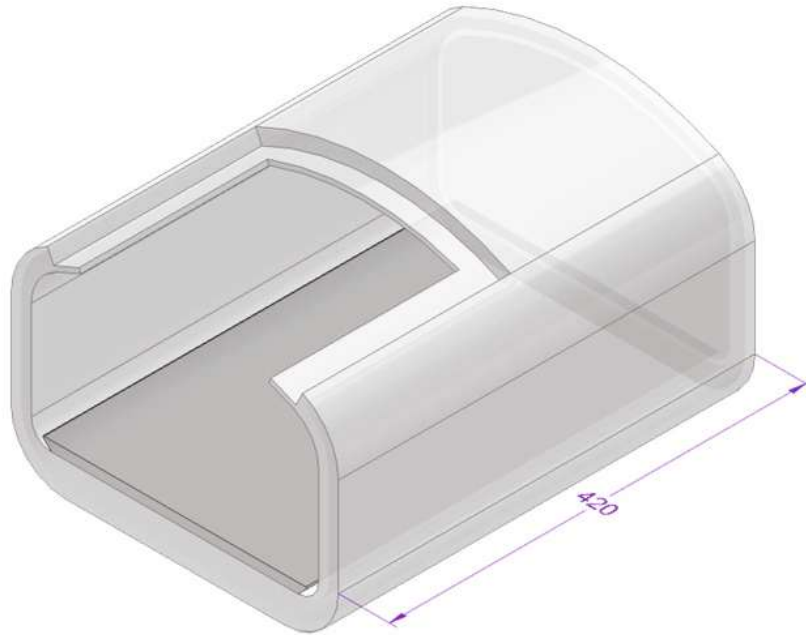


Figure 3.7: CAD render of the final OS version with a length measurement in mm for scale, in isometric view.

Considering these changes, a plate was foreseen that would interlock through an anchoring system to the inner floor of the OS. Thanks to this plate, no further modifications were required to the OS floor since all screw and dowel pinholes could be drilled into the plate to secure the other modules. This way, the MP's modularity was improved, enabling easier layout changes in the future without the need to change the whole OS. This plate can also be pulled in and out of the OS with all modules secured for easier installation. The plate can be seen in Figure 3.7 and Figure 3.8 with the drilled hole layout.

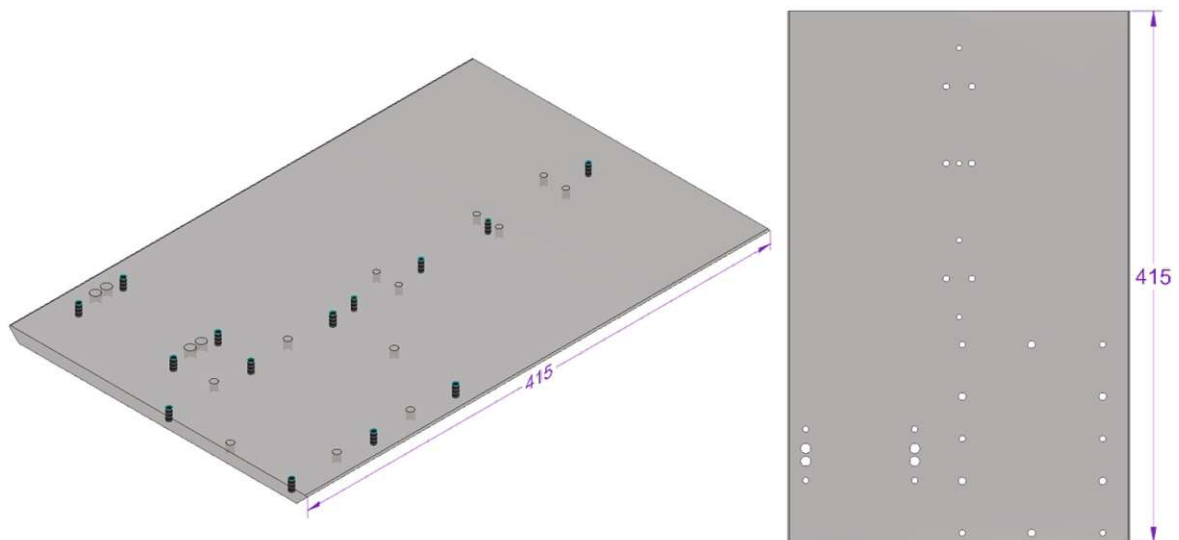


Figure 3.8: CAD render of the OS plate with length measurement in mm for scale, in isometric view (left) and top view (right).

In order to fill the interstitial space between the acrylic walls, an inlet/outlet had to be foreseen. This inlet was planned to be in the highest point of the caudal wall of the OS as a backflow valve, to be filled with the help of a hose from the top up. A venting valve is also needed in the filling process to ensure that no air bubbles are trapped in the liquid-filled

interstitial space since they would then be visible as signal-less artifacts in the scan. This venting valve was also placed extruding at the highest point of the OS, right next to the inlet valve.

Lastly, for the CM module, an MR visible gel mat is placed at the top cut-out of the OS. Since the mat is pushed from below, it is crucial for it to move and deform. Considering the needed mobility of the mat, it was chosen not to fixate it to the OS tightly but instead just lay it on top, kept in place by its weight and friction. For that reason, extensions of the acrylic plates were foreseen to hold the mat, as seen in Figure 3.7. Nevertheless, These acrylic extrusions were not enough to hold the gel mat without folding in the middle and falling through due to its high flexibility, also missing the one on top/front of the opening for manufacturability reasons. Therefore, a thin polymer sheet with the exact dimensions of the mat was fashioned to stabilize it. This sheet will be placed on top of the acrylic extrusions and held in place by the weight of the gel mat. To conclude, a cut-out had to be done to still enable the CM Gear Box to push the gel mat with its push-head from below. The cut-out has the slightly oversized shape of the Gear Boxes push-head. This polymer sheet can be seen in place in Figure 3.9. As a last design addition, the OS needs a filling valve, developed with Acrylstudio GmbH, to be filled and degassed optimally from the highest point in the OS. This is necessary to avoid air inclusions in the OS which could be viewed as artifacts in the scanned image.

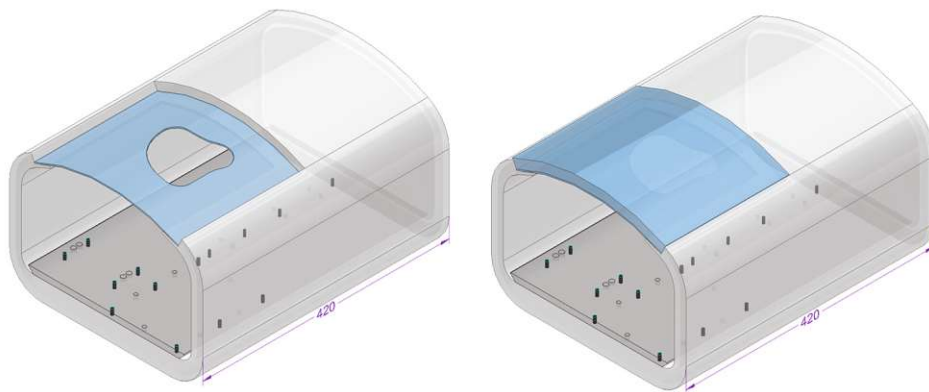


Figure 3.9: CAD render of the OS with its length measurement in mm for scale, in isometric view, with the support sheet (left) and the support sheet and gel mat (right).

3.2.3 Manufacturing and Materials

The material of choice to construct the OS walls was Polymethylmethacrylate (PMMA), most commonly known as acrylic/plexiglass, since it is a robust, water-resistant material known to be shapeable to the desired geometry. This knowledge came from the extensive production of non-motion phantoms already done in the MR-Center of the AKH. Compared to similarly strong polymers, the main extra advantage is the excellent transparency of the material, which enables one to see the watery solution inside the shell and, through that, the other modules. This facilitates the handling and testing of the phantom, as well as its quality control over time. The liquid solution, with which the OS gets filled up, is based on distilled water to get a pure liquid base to be added on and to avoid a quick deterioration of the liquid inside the phantom over time. To the distilled water, 2g/l of NaCl is added to increase its conductivity, as well as 5ml/l of a gadolinium-based contrast agent, which decreases the T_1 time of the solution to 400 ms when imaged in a 3T scanner.

3 Phantom Design and Development

Since the OS module is the base for the MP and has to bear weight as well as be leakproof, a professionally done manufacturing process was needed. This manufacturing was commissioned to the company Acrylstudio GmbH (Wr. Neudorf, Austria). This company has expertise in polymer work with usual acrylic usage. The manufacturing techniques used by Acrylstudio GmbH are the ones already mentioned in point 3.1.3, like heat bending, laser cutting, or CNC milling. They also provided expertise to make the OS watertight by acrylic soldering and with the valve selection for an air-free filling process. For ease of manufacturing, the plate where the modules are fixated is also acrylic and is manufactured in the same way by the company. By the time this thesis was submitted, the manufacturing process had started but had not been concluded.

3.3 Chest Motion

3.3.1 Requirements

The Chest Motion module (CM) is defined as the hardware parts that help simulate the chest's cyclical expanding and contracting motion caused by breathing. The chest wall is pushed in and out by muscles, like the intercostal muscles, by a couple of centimeters, which is one of the motions that expands and contracts the lungs. In the case of a person lying down, as in the MR scanner, the chest wall rises and falls with each breath. This is one of the most common motions that induces artifacts in MR images since it is not possible to entirely cease the movement over prolonged measuring sessions.

The part/material that simulates the chest wall when moving must be flexible and capable of moving consistently in an elastic manner for many simulated breathing cycles. The material has to be durable and optimally light to decrease the needed lifting force. The chest wall imitation must cover most of the thorax section and be at least 2 cm thick to simulate the thoracic wall properly.

Furthermore, it is of utmost importance that the chosen material has a T_1 and T_2 relaxation time inside a 3T scanner similar to the chest wall. The signal must also be strong enough to be in a range where it possesses good visibility when scanned next to the water inside the OS. This means that the material's signal strength has to be preferably a similar magnitude to water.

It is also required of the CM module of the MP to have a precise and controllable movement. The chest wall elevation has to be approximately 2 cm from its starting position and be precisely reproducible in every cycle in order to be able to use this movement as a calibration tool. Each “breathing” cycle has to be able to happen over 1-4 s, with a smooth movement from end to end. Preferably the movement curve should be tunable. Moreover, the lifting mechanism must be able to lift the weight of the simulated thorax wall.

3.3.2 Design

As mentioned several times, the thorax wall imitation chosen for its fulfillment of the requirements in 3.3.1 was a square-shaped gel mat with a thickness of 18 mm, which can be seen in Figure 3.16. The cut-out at the top of the OS was done to the specific size of the mat for it to fit over the acrylic extrusions, as seen in the CAD image of Figure 3.9.

In order to get the wanted motion out of the gel mat, a motion source had to be chosen. The actuator type and model were chosen first since the requirements strictly narrowed the selection. The strictest requirement was the fact that the actuator should be placed inside the scanner room, as near as possible to the MP as possible, meaning as close to the center of the scanner as it can be done. Pneumatics were discarded as an option since they are too uncontrollable during the movement, with different ramp-ups in every cycle, making a smooth movement impossible. Hydraulics can be better controlled. Nevertheless, it was undesirable to transport water in hoses over several meters into the scanner. Standard stepper motors or

3 Phantom Design and Development

other electromotors can typically not be used since they not only contain metal parts that could cause artifacts or interferences but could malfunction due to the scanner's strong magnetic field. Even polymer cast or additively manufactured stepper motors, which can be metal free, have their drawbacks. Since they usually do not achieve high movement velocities, or if done so, are prone to deterioration over time.

A more sophisticated motor that better suits the task had to be found while still within the project budget. The possibility of low-/non-magnetic piezoelectric stages was found being offered by the company Xeryon (Belgium). These motors are produced in a low-magnetic version, which can function under 1.5-2T, and a non-magnetic one. These two versions could theoretically be placed just outside the opening of the bore or directly inside it, respectively. Furthermore, this piezo stage has a maximum travel range of 100 mm, with a driving force of 3 N. A movement precision in the nm range can be achieved with it, as well as speeds of up to 200 mm/s in its closed-loop configuration. All this occupies a very small space, having dimensions of 120 x 34 x 13 mm. The linear stage outperforms the needs in some aspects, such as velocity and precision. However, the driving force of 3 N was too low to lift the gel mat. Regardless, the piezoelectric precision stages were chosen for the task of actuating the CM (Figure 3.10 + Appendix.01).



Figure 3.10: Precise linear piezo stage from Xeryon with 3 N output force in its 40 mm travel range version and magnetic model type.

At the start of the project, the low-magnetic piezo linear stages were selected due to being substantially more economical than the non-magnetic version. For that reason, the stages had to be placed at the entrance of the bore, where they would only be under a magnetic field with a strength of under 1 T. As well as being far enough away from the center of the scanner to avoid possible artifacts as a consequence of metallic parts. Taking this into account, the movement of the stage had to be transmitted into the MP by rods. Meanwhile, the motor is fixated to a scanner plate, where also the MP is fixed (further details on the Scanner Plate in Section 3.6). Since the piezo stages were linear, the movement direction had to be translated from a horizontal movement outside the MP to a vertical movement just below the gel mat. At the same time, the output force must be increased from 3 N to a lifting force of at least 10-12 N. This force is required to be able to lift the approximate 0.5 kg of net weight of the gel mat with ease, which weighs a total of 1 kg but is supported on three sides by the acrylic lips and the support sheet of the OS, reducing its net weight roughly by half. For this task, the idea of a Gear Box arose, which could increase the force through gear ratio using up the available extra traveling range, which is five times the needed 20 mm.

There were several possible solutions to the force increase and direction change. The first version was prototyped using modeling parts. This first approach consisted of a gear rack attached to the linear stage, which transmitted the movement to an interlocking pair of gears, where struts were attached at the same position along their radii. Transforming the rotational movement into a vertical one, trying to get a gear ratio out of the distance from the teeth of

3 Phantom Design and Development

the gear. This gear pair approach was pursued for several iterations, where designs were done using modified normed gears and possible additive manufactured parts. The three main iterations can be seen in Figure 3.11.

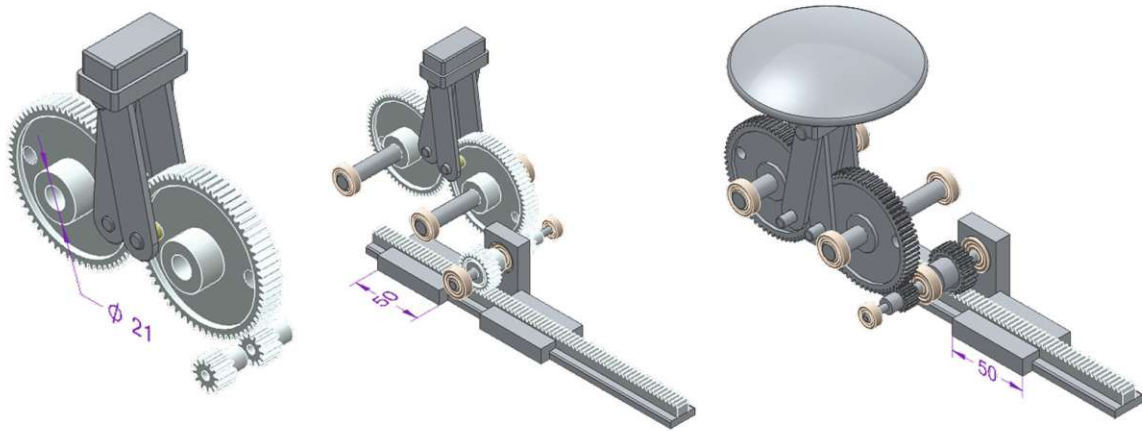


Figure 3.11: CAD render of the gear pair solution of the CM with length measurements in mm for scale, in isometric view. From left to right in order from oldest to newest iteration.

The needed traveling distance could be achieved through this method. However, the force increase was not as optimal as expected and would have required too big of a gear pair to possibly make it work. For that reason, this approach was abandoned after a preliminary design phase.

The second approach, which stuck as the final solution, was the rack and pinion approach. In this case, the linear stage is still attached to a gear rack, but the rack was interlocked to a pinion, which then could further interlock to a larger gear after a shaft transmission to get a more straightforward gear ratio with decreased travel range and increased force. This gear would then interlock to a second toothed rack, which was placed vertically, changing the movement direction. On top of this second rack, a push-head could be attached in order to contact the gel mat directly. The iterative design process can be seen in Figure 3.12, which shows how the parts and arrangement of them got more sophisticated with each step, using compound gears with the addition of bearings, guide rails, support beams, and surrounding supporting walls.

3 Phantom Design and Development

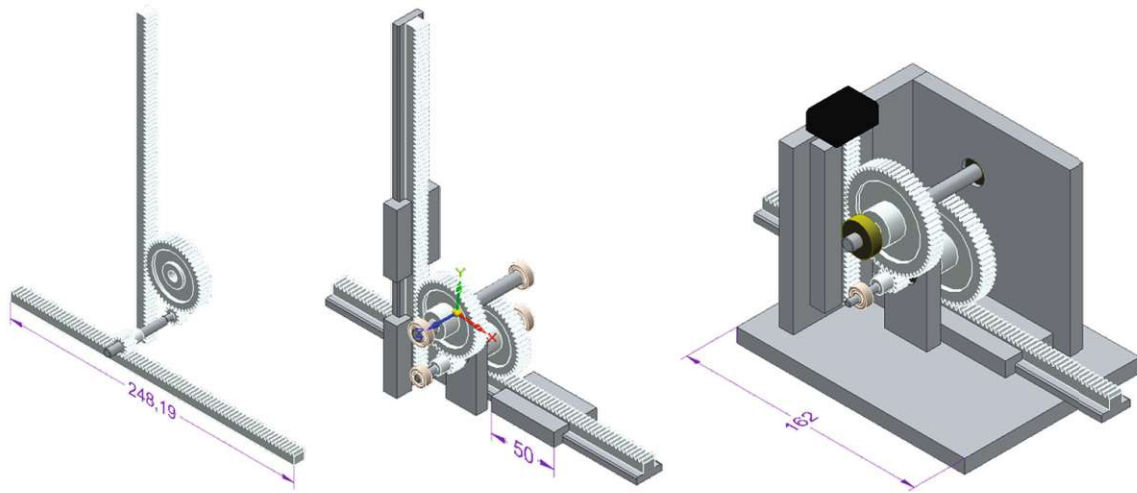


Figure 3.12: CAD render of the CM rack and pinion solution with length measurements in mm for scale, in isometric view. From left to right in order from oldest to newest iteration.

In order to create a self-sustained box capable of being stable and bearing weight, an extra gear had to be added. This also helped clear enough space for the vertical rack to move the desired length. Yet all these parts had to be fitted in as small of a space as possible to leave enough room to fit the other modules. For that reason, the walls and bought parts were also selected as small as manageable while still maintaining full functionality over time and being easily manufactured if needed.

The surrounding box was required not only for durability, to maintain clean gears, ease of handling, and to retain the modularity of the build, but also to help support the thin polymer shafts onto which the gears are fastened. The Gear Box's walls and floor also doubled as guide surfaces for the gear racks, secured in all directions but one through L-shaped tracks. All the materials used in the Gear Box are polymers, including the gears, racks, pinions, shafts, and ball bearings. These parts were fitted either as press fits in the case of the bearings, safety rings for the gears, geometrical fittings, or polymer screws and pins for the rest of the parts and the walls. The floor plate was designed as oversized to accommodate holes to fixate the Gear Box to the ground plate of the OS. This way, the box did not have to be disassembled in order to be mounted onto the MP. In that way, the module could be easily changed if needed. An acrylic plate was put in the front only to increase visibility inside the box for maintenance and instructional purposes.

The last part of the CM module is the push-head attached to the Gear Box's vertical rack and comes in direct contact with the gel mat. The first iteration was a simple stamp-like head, which was more of a placeholder, which can be seen colored as black in the right render of Figure 3.12. Nevertheless, after printing this stamp head, it was noticed that the contact surface was too small and the load was too punctual since the anatomical chest wall moves uniformly in and out. For that reason, the surface of the push head was increased. Also, the contact point of the push head was not centered with respect to the mat for space reasons since the Abdominal Organ Bulk module (AOB) was going to be actuated from the centerline of the MP. A quarter mushroom cap-like head was designed to improve this while avoiding sharp edges that could damage the gel mat, as well as strong torque forces on the vertical rack. In Figure 3.13, three iterations of this push head can be seen, with different contact curvatures of the contact surface. From the flat, convex, and concave variations, the latter one was selected since it gave the best homogenous contact with the flexible gel while pushing as

3 Phantom Design and Development

centered as possible. Also, the modularity was increased with a T-shaped press fit onto the vertical rack, with a screw hole as an optional safety, which enables the possibility of an easy change of design in the future, if needed.



Figure 3.13: FDM printed PLA push heads. The top view is in the upper row, and the bottom view is in the lower one, on a cm grid for scale. The curvature of the top contact surface of the print heads can be identified by their print layer pattern. **Left** = concave, **middle** = convex, **right** = flat.

All the mentioned design choices, among many others, achieved the final design that can be seen in Figure 3.14.

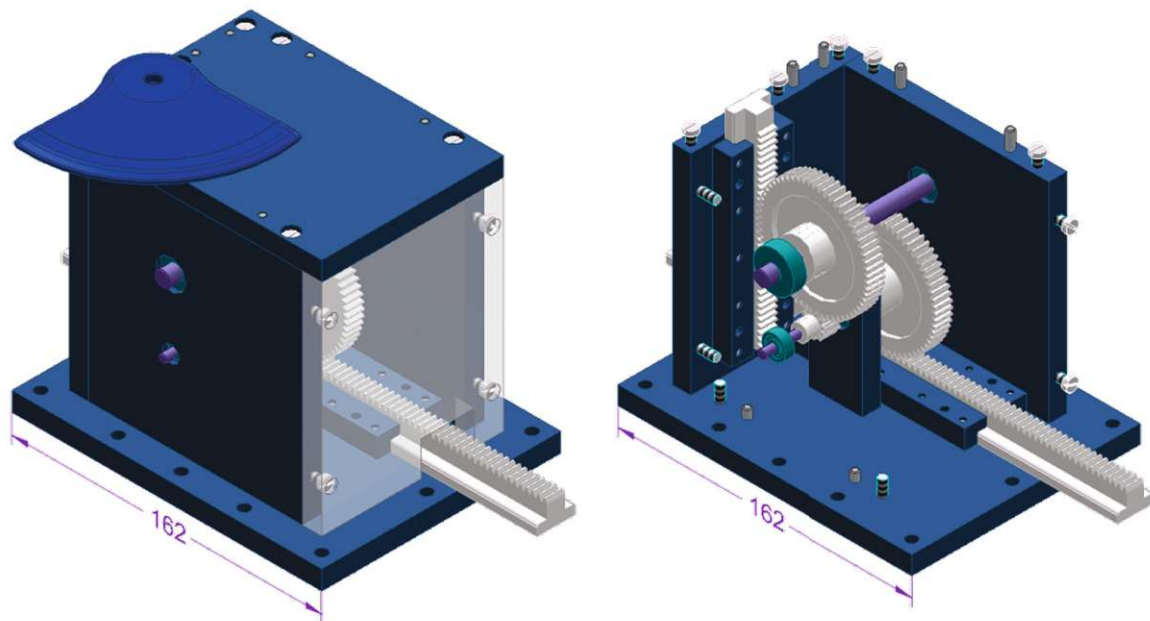


Figure 3.14: CAD render of the final rack and pinion solution of the Gear Box with length measurements in mm for scale, in isometric view. As a whole, in the left representation and with missing front, side, and top outer panels to visualize the inside mechanism.

The functional view of this approach can be viewed in Figure 3.15, where the horizontal rack, which would be attached to the piezo stage in the future, served as the input piece. The input is a motion of 100 mm with 3 N of force at a very high possible speed. This movement is then transferred to a 60-toothed gear wheel, clearing up vertical space for the vertical rack, so the rest of the mechanism can function correctly. This 60-toothed gear is part of a compound gear with a 12-toothed gear. Through this lateral movement shift, the two racks do not interfere with each other. This compound gear also has the side effect of reducing the speed of the movement, which is not an issue since the piezo stages can achieve velocities up to 200 mm/s,

which is more than sufficient. This slowing down of the movement also allows this shorter displacement to be more easily synchronized in its phase with the breathing motion of the other modules, which have a larger amplitude. This slow, controlled move is passed on from the 12-toothed gear to a second 60-toothed gear, creating a gear ratio with a factor of 5. This means that the travel range is decreased from 100 mm to 20 mm, but the force is increased from 3 N to 15 N. This movement is at last transferred to the vertical rack, which in turn pushes the gel mat with its push head, achieving the desired chest elevation of 20 mm and having more than enough force to lift the gel mat with roughly 0.5 kg net weight.

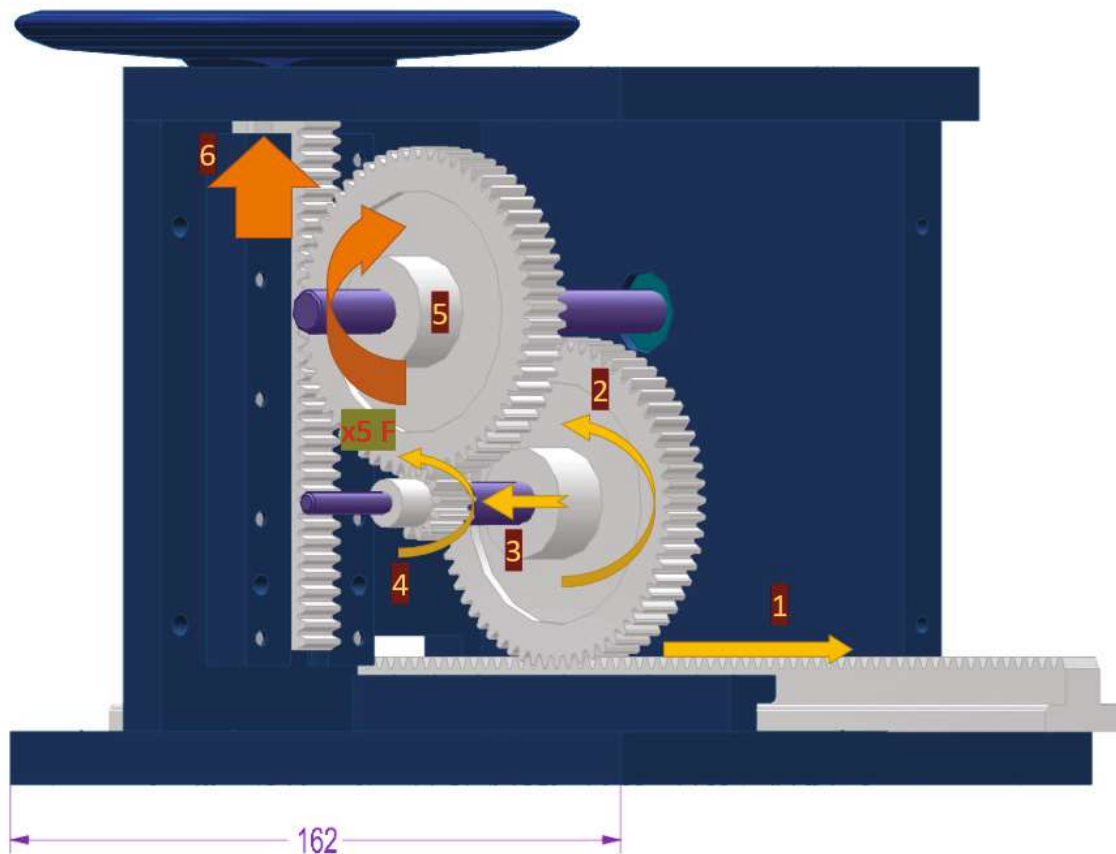


Figure 3.15: CAD render of the final rack and pinion solution of the Gear Box with length measurements in mm for scale, in an isometric edge perspective. Arrows in each movement transfer step indicate the functionality of the movement, with particular emphasis between steps 4 and 5, where through a gear ratio, the force of the movement gets increased by a factor of 5.

3.3.3 Manufacturing and Materials

As mentioned above, the selected gel mat has the required mechanical, geometrical, and MR signal characteristics. Due to its mechanical properties, the mat is, in fact, commercially used as a cushion inlay for motorcycle seats. This 25 cm by 25 cm square mat, with an approximate thickness of 18 mm and approximately 1 kg of weight, is made out of elastic polyurethane fiber. This material provides a gel-like feel while being cuttable without any flow or leakages. To avoid the stickiness of the material, the mat possesses a very thin transparent film that surrounds the whole piece, which can also be seen in Figure 3.16. Several companies offer this

3 Phantom Design and Development

product, but for this thesis the, one of the automotive components brand Aiuphing (China) was used.

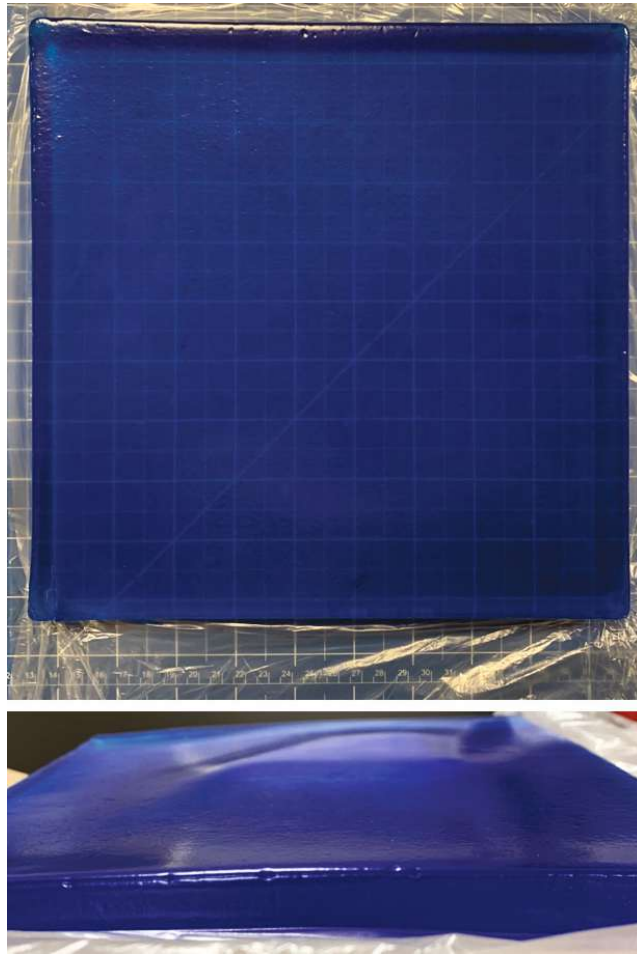


Figure 3.16: Photograph of an elastic polyurethane fiber gel mat on a cm grid for scale.

The polyurethane mat has an acceptably strong signal when measured in the 3T scanner. For usability purposes, the T_1 and T_2 times had to be also known. These were determined using the inversion recovery (T_1) and spin-echo (T_2) pulse sequences techniques described in detail in Point 2.2.1. Resulting in a T_1 of 191.0 ms and a T_2 of 120.1 ms. The corresponding plots, from which the relaxation times were experimentally derived by interpolating the measured points, can be seen in Figures 3.17 and 3.18.

3 Phantom Design and Development

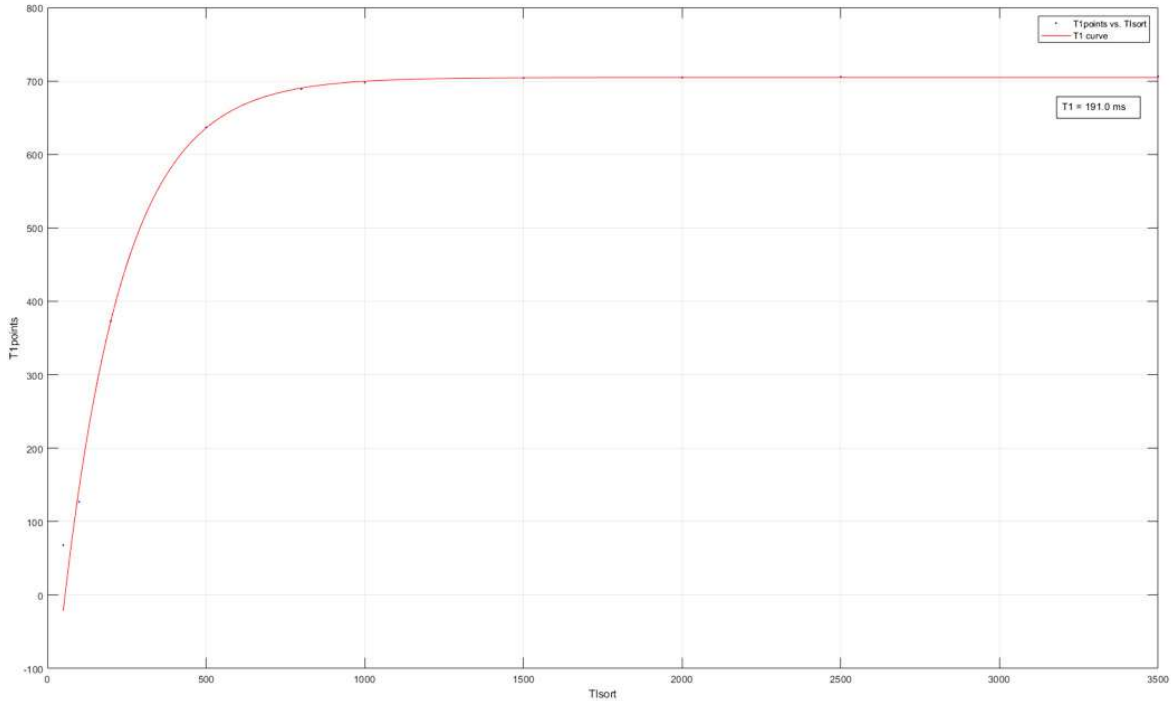


Figure 3.17: Inversion recovery measurement plot for T_1 determination of the CM's gel mat.

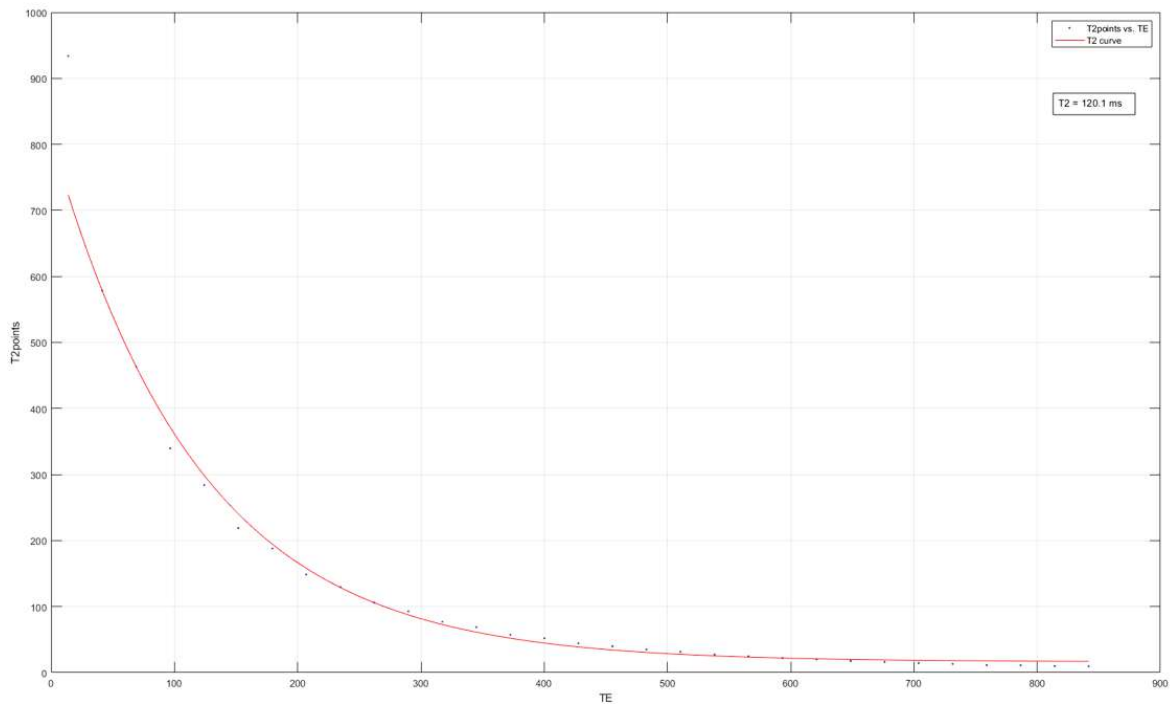


Figure 3.18: Spin-echo measurement plot for T_2 determination of the CM's gel mat.

The specifications of the ultrasonic precision piezo linear stage of the company Xeryon are already mentioned in the point above. The specific model first ordered for the CM is the XLS-3-120-1250-LM-SC, which comes with its own controller and 10 m long cables for it to be able to be controlled outside of the scanner room while being placed at the opening of the bore. This motor variant is neither a stick lip nor a stepping piezo motor, which Xeryon also offers.

3 Phantom Design and Development

This motor is an ultrasonic resonant piezo linear stage with standing wave in an open loop configuration. This means that the stage is bidirectional in movement and force production. The movement is created by the elliptical oscillation of the contact point between a small ceramic ball and the elongated ceramic slider piece, which is mounted onto bearings. The standing wave portion refers to the fact that the contact points do not move in space but just vibrate in an elliptical trajectory against the slider. A functional sketch of this movement is seen in Figure 3.19. The vibration movement is enhanced since the frequency resonates in two ways with the structure of the piezo motor. The two structural resonances produce two motions, one tangential and one perpendicular to the slider, creating the elliptical path. This movement is repeated at an ultrasonic frequency, creating a swift bidirectional action. This high frequency also has the side effect of being outside the human hearing capabilities, therefore appearing noiseless. This type of motor works for long distances and long lifetimes due to its low contact impact and low thermal generation.

It is planned to replace the aluminum top of the linear stages with exact acrylic replicas ordered to be custom-made by Acrylstudio GmbH, the same company as the OS since the acrylic will certainly not produce material artifacts in the scans.

Due to complex supplier difficulties, the low-magnetic version had to be changed to the non-magnetic one in order to ensure that the linear stages were delivered at the planned date. The exact reason is that the steel bearings of the low magnetic version could not be supplied to Xeryon, but the ceramic ones, of the non-magnetic version, could. This change was done very close to the end of the development since the ordering, manufacturing, and delivery times for this product already took several months, making the decision more critical. Nevertheless, this allows a closer placement of the motors to the opening of the OS, which will be further discussed in the outlook of the thesis. Further details on these piezo linear stages can be seen in the Datasheet in Appendix.01 or on the Xeryon website.[33]

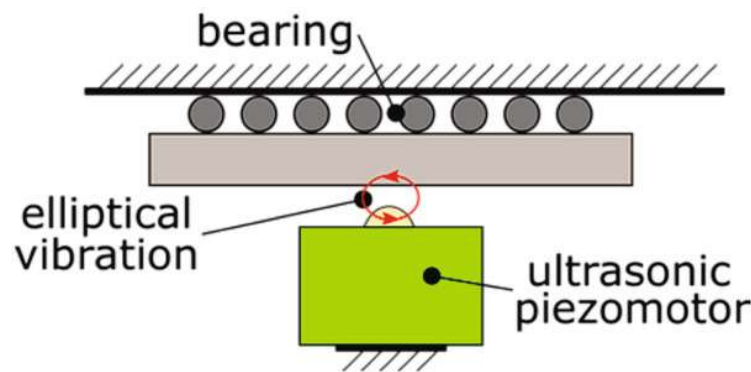


Figure 3.19: Functional schematic of the function of an ultrasonic resonant piezo motor with standing wave.[33]

The push heads seen in Figure 3.13 were manufactured in an FDM printer (Ultimaker 3, Netherlands) due to their complex geometry and to quickly get the different variations. The CAD model was sliced for the printer using Ultimaker's proprietary, open-source slicer Cura. They were printed with an infill of 60% to make them durable and stable under load for a long time. They were printed with the thermoplastic filament PLA, which generally showed good printing results from experience and possessed less brittleness than other commonly used thermoplastics like acrylonitrile butadiene styrene (ABS).

All the gears, racks, and bearings were acquired from the company igus GmbH (Germany). This company has a reputation for high-quality technical polymer products that adhere to European norms and standards for parts, which is why it was chosen. The gears and racks had

3 Phantom Design and Development

a gear tooth module of one (M1). They were all from the material iguform 270, a company-specific polyacetal variation, a strong plastic with low friction coefficients. The balls bearing consist of glass balls, with a company-specific material xirodur C160 for the rings and cages made of polypropylene.

The rest of the parts of the CM were specifically custom-made for this build in the precision workshop of the Center for Medical Physics and Biomedical Engineering (CMPBME) at the Vienna general hospital (AKH). Standard workshop machines like CNC cutters, milling machines, and lathes were utilized. The material used for the raw stock, like plates, shafts, and dowels, is hard PVC and is held together by normed DIN polyamide nylon screws. The end result of the finished Gear Box can be seen in Figure 3.20, which with the gel mat from Figure 3.16, comprises the CM.

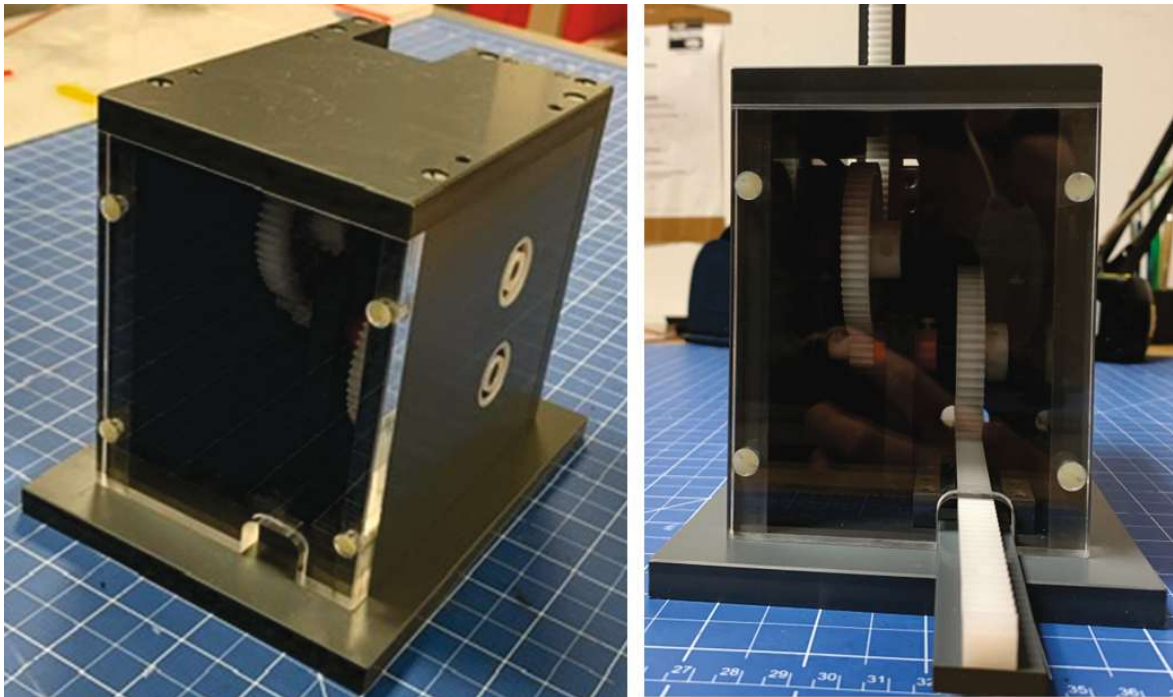


Figure 3.20: Photograph of the build Gear Box. Isometric view on the left and front view on the right. The Gear Box is placed on a cm grid for scale.

3.3.4 Test and Evaluations

For the functionality of the Gear Box to be tested, a test setup had to be designed. Since it was the first module to be built, it could not be fastened to the OS or any other part. Furthermore, the piezo stages did not arrive till the end of the thesis, so the Gear Box had to be tested with standard servos (60° rotational movement) outside of the scanner. To drive the horizontal rack of the Gear Box with a rotary servo, the rotational movement had to be converted into a linear one. An additively manufactured gear was designed and printed. It had the exact radius to produce a movement slightly over the 100mm produced by the piezo stage, with the 60° rotation that the servo was capable of. This gear was then press fitted to the moving wheel of the servo and secured with a screw. The servo was placed in a custom-printed stand precisely designed for the servo actuator. The gear then transferred its movement onto a gear rack secured to a holder piece that provided the desired elevation of the rack. This holder doubled

3 Phantom Design and Development

as a connection with the horizontal rack of the Gear Box, which was connected by using a toothed press that pushed against the teeth of both racks and tightly secured by a custom-made screw. All these parts can be seen colored in red and blue in Figure 3.21, where the test setup is shown in CAD.

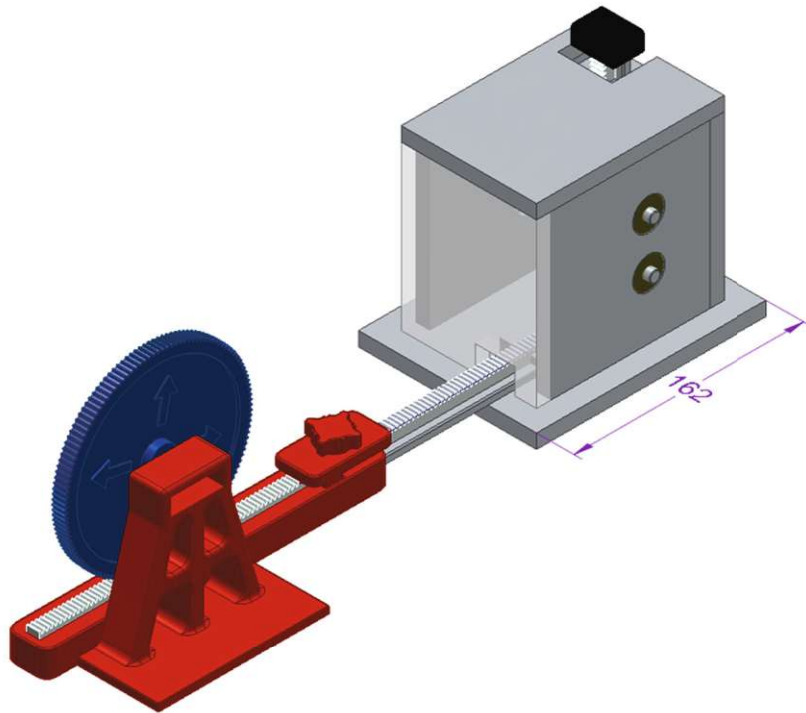


Figure 3.21: CAD assembly of the designed parts for the CM's functionality test.

All these parts were additively manufactured in order to cut costs, acquisition times and be able to make them fit the specific needs since this was only a one-time functionality test. To temporarily hold the gel mat, a cardboard box was modified to have the required height and hole sizes. The build setup with the physical manufactured parts and servo motor can be seen in Figure 3.22. The results were positive. The Gear Box provided the required force increase with sufficient travel range while working smoothly with negligible friction between the parts.

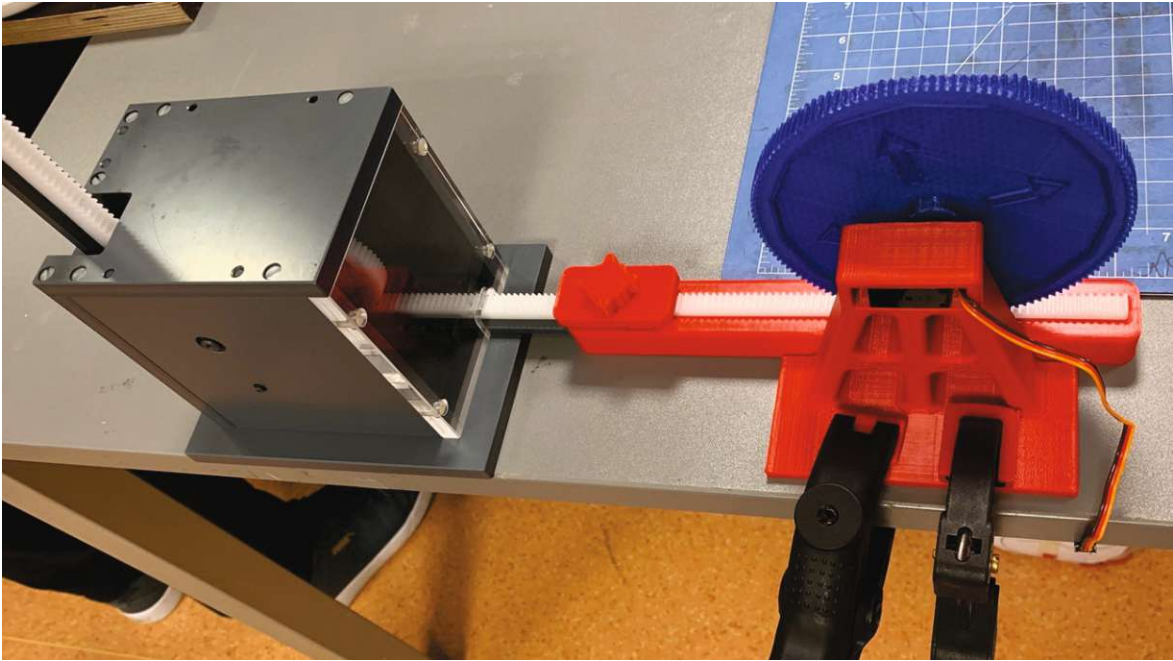


Figure 3.22: Photograph of the manufactured test parts attached to the Gear Box.

This Test setup was also used in a cross-validation test where the produced chest motion was measured by the Beat Pilot Tone motion tracking system developed in parallel. A coil was attached to the gel mat, recording the movement by the shifts in the signal sent by an antenna fixed over it. The Beat Pilot tone system measured the fixed 2cm movement, providing preliminary cross-validation to both systems.

3.4 Abdominal Organ Bulk Motion

3.4.1 Requirements

The Abdominal Organ Bulk Motion module (AOB) is the complementary module to the CM, which, in tandem, simulate the two most important movements generated during a breathing cycle. The AOB is defined as the hardware parts required to simulate the cyclical movement of the abdominal organs, caused mainly by the ascension and descent of the diaphragm. The diaphragm is the primary muscle that increases and decreases the thoracic volume during the breathing cycle, expanding and contracting the lungs. The abdominal organs get pushed in caudal direction, being compressed against the pelvis. During this movement, the abdominal organs get pressed against each other, shifting in all directions. This complex movement creates a variety of motion artifacts when scanning the abdominal region. This is one of the most common motion artifacts since this motion can not be paused over a long time period, even more since this motion is not perceived from the outside.

This complex motion was simplified for the developed MP, consisting of the simple linear movement of a bulk along the cranial-caudal line. The bulk represents the whole lower part of the internal torso, so it should be as voluminous as possible, given the space inside the OS. The entire caudal half of the inner OS space is reserved for this bulk and its motion.

In addition, this bulk should consist of a shell, which preferably ought to be MR-visible, that is hollow on the inside. This shell must be able to be easily opened, so the interior can be checked and switched often. The modularity concept of this build is also crucial for this module, for it to be outfitted depending on the necessities of the measurements. In order to get a high signal when the movement of the abdominal organs is replicated and measured, this shell should be able to be fully filled with pieces of the same elastic polyurethane fiber gel material as is used in the CM. Furthermore, inside the AOB shell, the additive printed phantom of a liver with its main input arteries should be able to be fitted securely. This liver phantom is a parallel project also at CMPBME by another research team, where the liver is perfused with a radioactively tagged fluid to be used in PET-MR as the basis for an in-vivo study. The study is about liver blood supply in a moving environment (breathing motion) for pharmacokinetic models. It makes use of the MP to optimize, assess, and validate its model. The module could accommodate other abdominal organ phantoms in the future, which should be considered with foresight.

This module also requires attachment points for the Heart Motion module (HM), which is supposed to also move at the same rate, frequency, and amplitude as the abdominal organs. Since the anatomical heart also shifts its position during the breathing cycle. The HM is supposed to be attached to the AOB instead of just being moved independently because this module also undergoes a secondary movement with a much shorter frequency and amplitude. This secondary movement is the heartbeat. In this way, there is no need to actuate the HM twice, but rather the AOB movement is reused while being precisely in tandem with the breathing cycle.

Moreover, a small aperture has to be planned for the horizontal rack of the CM to be able to move freely. This is the only part of the other motion modules penetrating the caudal half of

the OS. Given that the horizontal rack has to move a considerable distance due to the gear ratio.

Lastly, this bulk's movement must feature a range of up to 50 mm while having the same frequency as the CM, so roughly one cycle every 2-4 s. The movement is linear along the MP and should also be secured to the floor plate of the OS. This movement has to be smooth and secure since the weight of this module is substantial compared to the overall MP, so tolerances should be generous, and failure safeties should be planned. Besides, the actuator of the AOB movement should have enough force to drive the AOB and the HM along the desired length.

3.4.2 Design

At the start of the design phase, the AOB was treated as a movable volume that should be as big as the other modules permitted. Therefore, the rail system was developed first. In the first sketches, the rail system consisted of two independent rails opposing each other at the sides of the inner space of the OS. Nevertheless, this idea was quickly changed to a monorail system since the anticipated weight is substantial enough to raise concerns about the AOB sagging in the middle of a two-rail system. Also, merging the two rails saved up on the total used volume of the rail, leaving more space for the bulk.

This monorail is made up of a single, sturdy, and strong polymer piece, which runs all the way through the middle of the caudal half of the MP. Being an elongated body that produces low/no signal in the scanner could be seen as a partial stand-in for the anatomical spine, making it less intrusive than a double rail. This polymer block is securely fixed to the ground plate of the OS by four oversized screws and six pins. As a result, the block should not budge at all, even when the heavy bulk moves back and forward on it over a long time. The polymer block has an effective length of 245 mm, permitting an AOB length of 185 mm while having 50 mm moving space and 10 mm safety runway space. To further increase safety in case of a failure or overextension of the movement, two boards were positioned at the end of the rail to avoid derailing the bulk by all means necessary. For the AOB to slide over the rail, two rows of equally spaced notches were drilled into the top of the block and offset spaced notches on each side. Inside these notches, self-made polymer rolls were pressed into them. The dowel of the rolls was press fitted into place while allowing the rolling cylinders to spin freely with very low friction. Rolls were chosen instead of balls since they can bear more weight if the movement is only along a straight linear path. Due to the high amount of rolls, the heavy bulk should not have any problems gliding along the rail with very little force needed. The lateral rolls are foreseen to avoid any moment in case the force is not transmitted exactly centered or the center of gravity is too offsetted from the center. The CAD design of the monorail system can be seen in Figure 3.23.

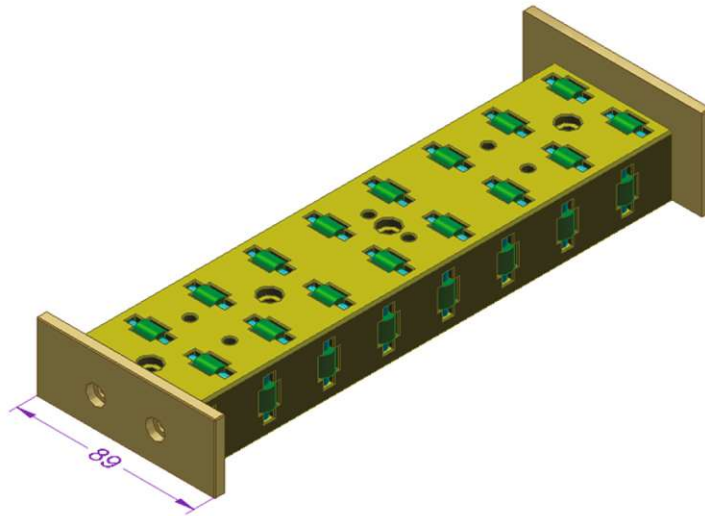


Figure 3.23: CAD render of the monorail system of the AOB, in isometric view, measurement in mm for scale.

The shell part of the AOB, where the functional liver phantom will be placed, is only defined in its outer measurements by our research team. Another team will design the inner space of the shell for their specific needs. Considering this, the AOB was planned for any possible internal shell structures. This AOB shell could even be easily replaced if needed, depending on the planned future use. Nevertheless, we worked closely with the other team to ensure that the AOB shell and inner structures did not oppose any MP requirements and had an optimal design and functionality.

In order to not have the need to screw or attach the AOB shell in any way, the idea of a “wagon” where the bulk could be placed in and moved along the rail was developed. This wagon was made out of polymer plates, as thin as they could be managed for the bearing load and manufacturability. This wagon can be seen in Figure 3.24. Its walls come close to the OS walls permitting the AOB shell to fill as much space of the caudal half of the MP with as small of a gap as possible between the visible water in the OS and the MR visible material inside the AOB. The walls that make contact with the rail are thicker due to them supporting the weight load. This is also the case for the front (cranial) wall, which fills the whole cross-section of the inner OS space. This wall must also bear the HM module's weight since this one is attached here. The attachment holes for the screws and pins can be seen on the left side of the plate (cranial viewing direction).

Furthermore, an opening at the other side of the HM attachment points was foreseen. This hole is necessary for the free movement of the horizontal rack of the CM. Lastly, an attachment piece was tightly and securely screwed to the wagon's base plate, where the movement and force can be transmitted through a linear stage push-pull motion. The force transmission point is precisely in the centerline of the AOB to avoid moments and tilts. This piece has to be reworked once the linear stages are available.

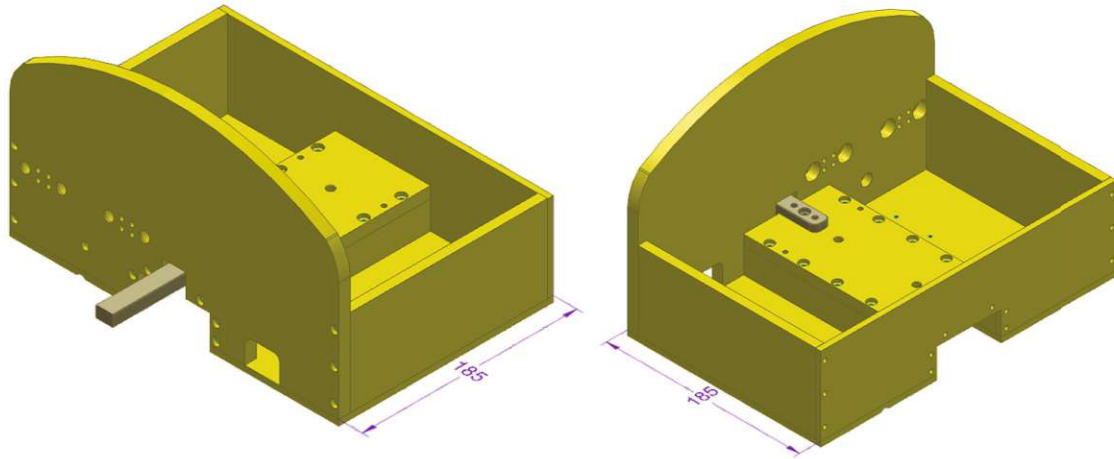


Figure 3.24: CAD render of the AOB wagon, measurement in mm for scale. Both views are from the same part in isometric views. The left one is seen from a cranial-lateral direction, and the right one from a lateral caudal direction.

The actuating motor planned for the movement of the AOB is the same as the one used for the CM module. The movement needed for the AOB is also a simple straight linear movement. For the reasons mentioned in Section 3.3, the linear piezo stage fits the requirements optimally.

The shell of the AOB can be viewed in Figure 3.25. This shell was planned to be additively manufactured due to its complex shape, which needed to fit precisely into the walls of the wagon and inside the OS. This piece fits perfectly onto the wagon and only possesses cutouts where they are necessary, such as the rail system, the horizontal rack, or the motor attachment point. Two pinholes were designed at the bottom to further secure this bulk when moving and to better transfer the movement and force. The top of the shell will be removable in order for it to be filled with the phantom organs and stuffed with MR visible material to get a high amount of MR visible volume, as well as for shimming purposes (Shimming is the process of making the static magnetic field in the MR scanner as homogeneous as possible even if materials with different magnetic susceptibility are present. It is automatically performed by hard- and software included in the MR scanner, but typically has limitations with air gaps). This allows access to the inner of the AOB for measurements without the need to fully dismantle the whole module.

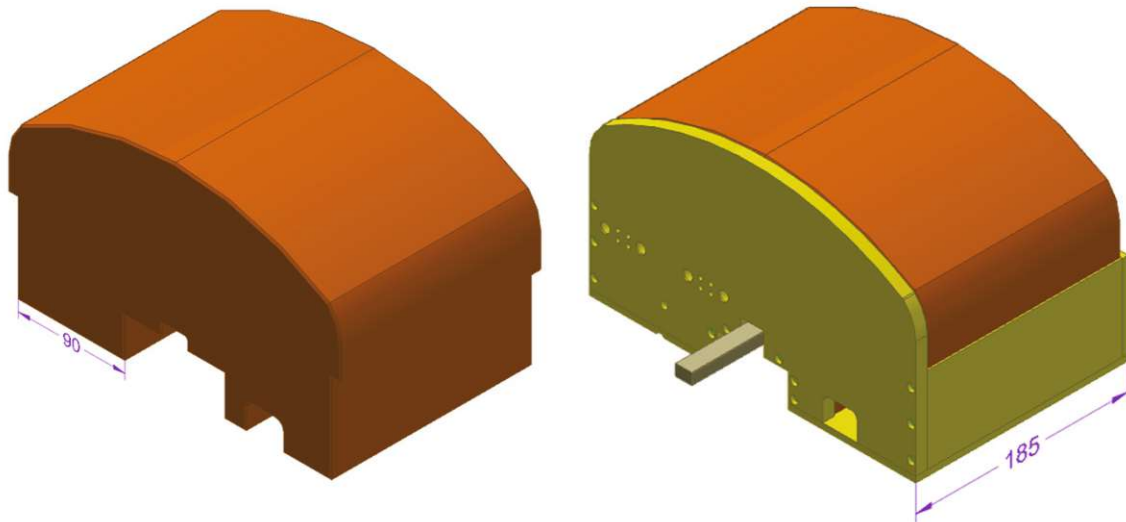


Figure 3.25: CAD render of the AOB shell, in isometric view, with measurements in mm for scale. Left image as a singular piece, and the right one with the shell fitted inside the AOB wagon.

Inside this AOB shell, the liver phantom will be housed. This liver is additively manufactured in an SLA printer as a thin transparent solid hull. This process was chosen by the other team in order to manufacture this highly complex geometry while maintaining water tightness. The liver has three chambers, the liver chamber, the portal vein, and the vena cava chambers. These three chambers can be filled separately with the use of surgical valves. The filling substance is mainly distilled water, with minimal amounts of a radioactive isotope marker for the PET MR tests. The vena cava is there just for anatomical reference, while the portal vein compartment is the one being measured. The concentration of the radioactive substance in the portal vein chamber against its surrounding volume is what is being measured. The liver phantom underwent several iterations. The current one by the time of the writing of this thesis can be seen in Figures 3.26 and 3.27.

3 Phantom Design and Development

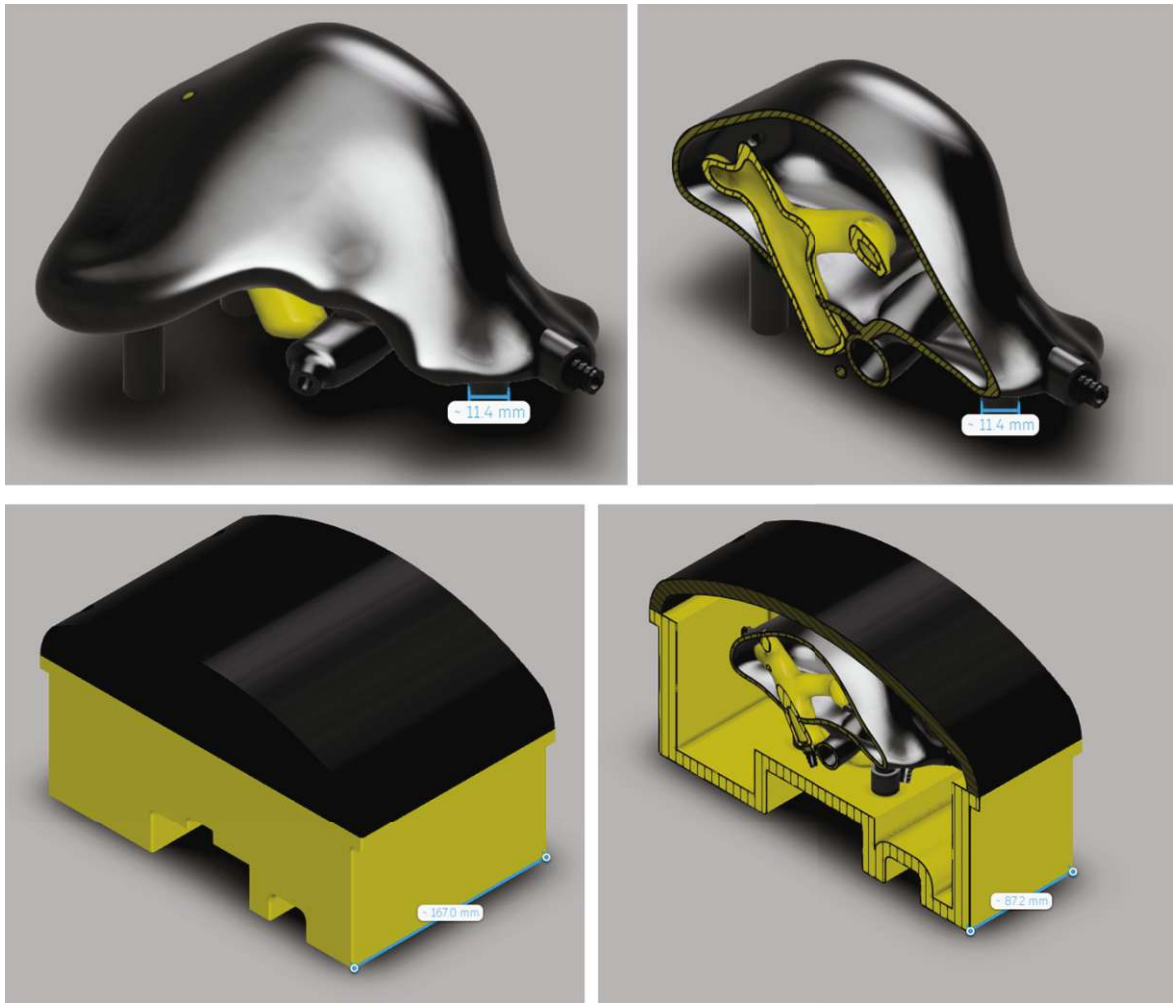


Figure 3.26: CAD render of the AOB liver phantom, in isometric view, with a measurement in mm for scale. The main liver body is colored gray, while the veins are colored yellow. The left top image is the whole phantom, while the phantom can be viewed through an intersectional cut on the right top. The bottom images are of the AOB shell with the phantom inside, as a whole, and with a viewing cut, respectively (left and right).

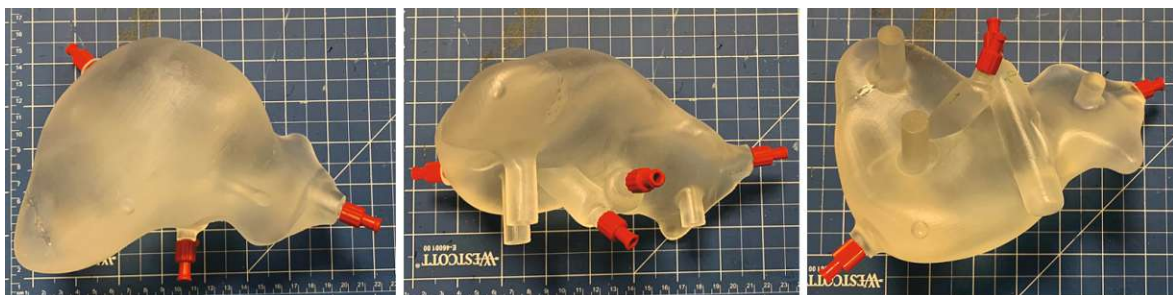


Figure 3.27: Photograph of the final additively manufactured liver phantom filled with a water solution on a cm grid for scale. **Left** = top view, **middle** = front view, **right** = bottom view.

3.4.3 Manufacturing and Materials

Most of the manufacturing processes and materials of the AOB module are the same ones as those used in the CM module. The polymer raw stock parts, like pins and plates, are made of hard PVC, fixated with normed DIN polyamide nylon screws. The rail rolls were precisely lathed out of polycaprolactam (PA 6), also known as Nylon 6. All this standard work on the AOB monorail and wagon was also done at the precision workshop at CMPBME. The tolerances for this module had to be under a fraction of a mm in the case of the monorail with its rolls and contact surfaces. This was achieved, leading to a smooth low friction linear motion. The manufactured monorail can be seen in Figure 3.28, and the wagon in Figure 3.29.

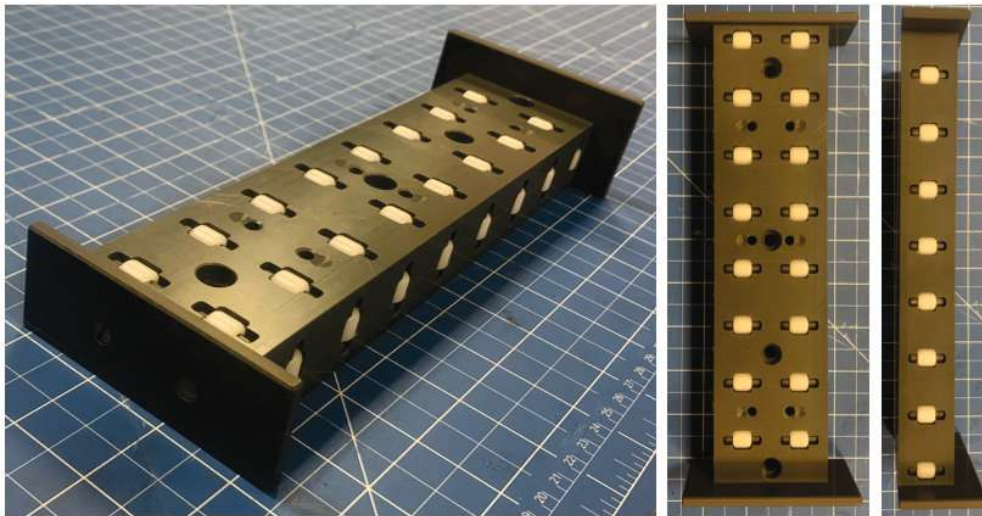


Figure 3.28: Photograph of the manufactured AOB monorail on a cm grid for scale. **Left** = isometric view, **middle** = top view, **right** = side view.

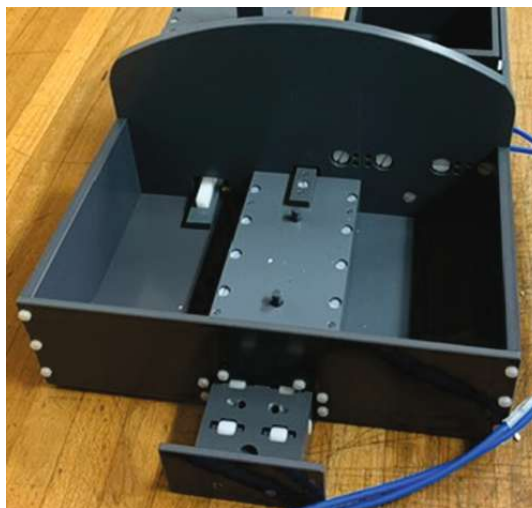
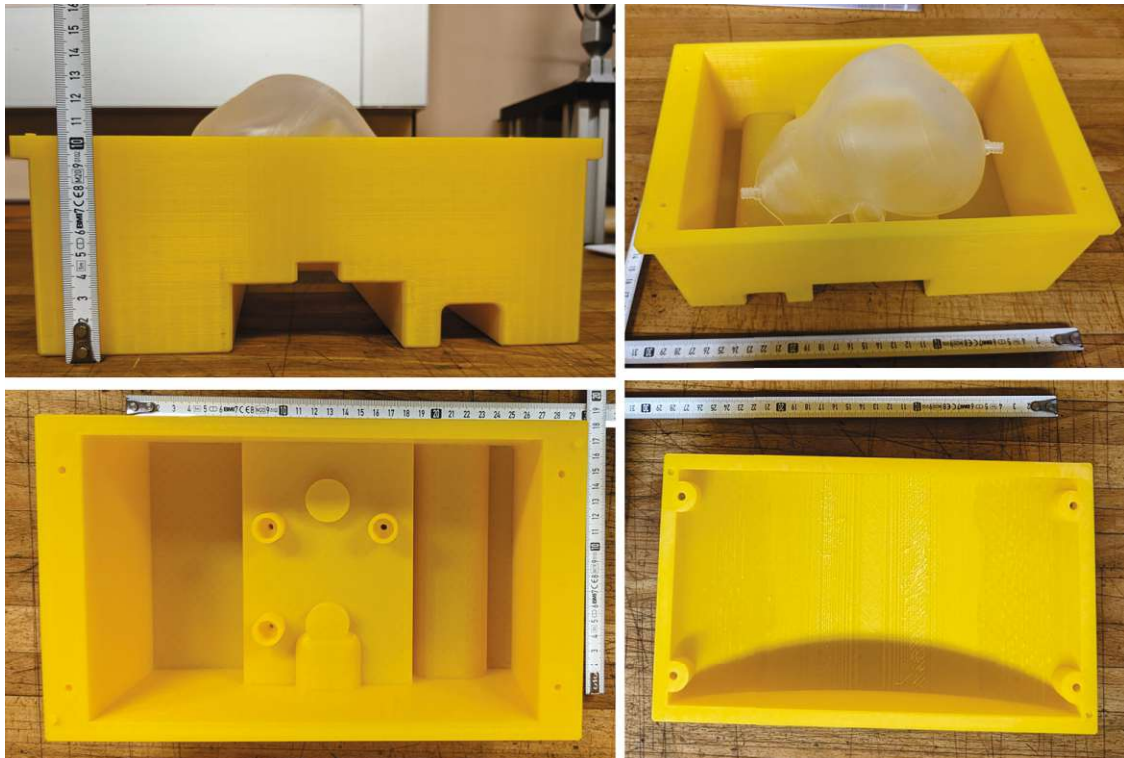


Figure 3.29: Photograph of the manufactured AOB wagon on the monorail, viewed from the caudal end.

The bulk shell of the AOB was planned to be manufactured with a novel MR visible to minimize the non-MR-visible space. Nevertheless, due to its size, the bulk required too much of this hand-manufactured novel material, as well as the need for a bigger 3D printer. In the end, it was printed on the Raise3D Pro2 Plus (California, USA) FDM printer with a building space dimensions of 305×305×605 mm, proving big enough to be built as two pieces, the

3 Phantom Design and Development

main body, and lid. The CAD model was sliced for the printer using Ultimaker's proprietary, open-source slicer Cura. It was printed using standard PLA with a 20% infill to save weight, material, and printing time since this part does not need to bear a big load. The printed and two-part AOB shell can be viewed in Figure 3.30.



*Figure 3.30: Photographs of the printed AOB shell. **Top left:** front view of the main body with the liver phantom. **Top right:** back-top view of the main body with the liver phantom. **Bottom left:** top view of the main body. **Bottom right:** bottom view of the shell lid.*

This bulk was filled with the liver phantom of Figure 3.27, which was printed on a Formlabs Form 3 (Formlabs, USA) printer using the Formlabs Clear V4 resin. If needed, the rest of the space inside the AOB shell will be packed tightly with elastic polyurethane gel mat pieces, like the ones seen in Figure 3.16.

As stated in Point 3.4.2, the movement was produced by the same linear piezo stages as the CM. Their characteristics are the same, but the AOB stage only has an amplitude of 50 mm for their movement range. Therefore, the length of the stage is only 80 mm instead of 120 mm, making the exact model the XLS-3-80-1250-LM-SC. Further characteristics can be seen in Appendix.01. This linear stage is capable of the movement required since it has enough movement range and velocity for one cycle in about 1-4 s. In the case of the required force, the motor only has 3 N to move a several kg heavy load. However, this should not be a problem since, in this case, the load does not need to be lifted but just moved along low friction rolls. Therefore, no gear ratio or any other force/movement transformation is required.

It should be considered to do a slowing down motion after accelerating the whole AOB plus the HM module since, with its heavy weight, it carries a substantial amount of momentum along the rail. This can be integrated into the sinusoidal moving pattern programmed onto the piezo stage controller.

3.5 Heart Motion

3.5.1 Requirements

The Heart Motion (HM) module is defined as the hardware parts that simulate the beating motion of the heart. This motion was first envisioned as a pulsatile or expanding soft body motion. Instead, this idea was replaced by a simpler, short, straight-lined motion of a rigid heart-shaped MR visible material. This change reduced the complexity of the module and made it easier to develop and work with the rest of the MP. The short motion of a rigid body is more than sufficient for the first test and validation attempts planned for this MP. This short high-frequency simulated motion should be a linear 20mm displacement in cranio-caudal direction with a frequency of 1-2Hz, which should be enough movement to be measured by external devices. Nevertheless, the module should be designed to be easily replaceable by more advanced heart models. The heart also has a second main motion besides the heartbeat. This is its positional shift with each breath due to the expansion of the chest wall and, in turn, the lungs. In conclusion, the heart needs a short high-frequency heartbeat motion, as well as a more extended breathing motion, which should be in tandem with the AOB and CM motion.

Therefore, a heart-shaped rigid MR visible part is needed. This part should not be liquid-filled to avoid the sloshing of the water with its high-frequency movement. This heart phantom must then be actuated for two distinct motions, with different frequencies and amplitudes, in the same axis of movement. Given that this movement does not need to be as controlled and precise as the movement of the last two breathing modules (amplitude and time course), there is no need for it to be highly configurable since the amplitude can stay the same, and only the frequency should be variable. Furthermore, the linear piezo stages could produce artifacts if placed inside the already very limited MP space. Nevertheless, having them outside creates difficulties when transducing the movement from a fixed position to an already moving module. Therefore, there is no need for a sophisticated piezo linear stage. Considering that, another type of linear movement actuation is to be used, instead of the expensive piezo stages, in order to save project resources that can be used elsewhere.

Since this is the last developed module, it needs to fit in its entirety in the empty quarter of the inner space of the OS, which roughly corresponds to the anatomical heart location.

Keeping with the modularity approach of this MP in order to maintain its usefulness over time and in different projects, this module should be easily modifiable or exchangeable. In the future, it is planned for this module to be modified to do multi-phase MR elastography on an elastic sphere-like heart phantom, filled with pressurized fluid for a project of another cooperating team. They want to identify tissues' stiffness and shear modulus under static and cyclic pressure. Accordingly, the elastic heart needs to be vibrated through the CM gel mat for this MR elastography technique, which also needs to be considered when positioning the rigid heart version.

3.5.2 Design

As stated in the requirements, several modularity aspects must be foreseen. First, it was decided that the MR visible heart phantom should be placed inside a box-shaped receptacle. Therefore, the heart phantom does not need any attachment points or a defined shape. This receptacle box has an inner space of 100x100 mm. With these measurements, the planned MR elastography sphere with a 100mm diameter could be snugly placed inside. It is also positioned in the OS space at a height where the sphere can barely touch the gel mat. Nevertheless, the heart phantom used in the scope of this thesis for MR motion creation does not require such specific measurements. For this thesis, it was decided to do an additively manufactured print of the scaled-down version of a scan of a heart. In its first iteration, the heart was printed using a novel patented MR visible SLA printing material. It uses microcapsules of paraffine oil trapped in the resin to produce a signal inside the scanner. This part can be seen in Figure 3.31, right next to the image of its first MR scan. During this scan, the relaxation times of this material in this format were determined by the technique explained in Point 2.2.1. This resulted in a T_1 of 269.7 ms and a T_2 of 183.2 ms. The corresponding plots, from which the relaxation times were experimentally derived by interpolating the measured points, can be seen in Figures 3.32 and 3.33. With this data, as well as viewing the image of the scan next to the scanned image of the CM gel mat, it was noticed that the signal strength of the material is very low. This could be a problem when being scanned inside the MP with a high signal, water-filled shell surrounding it, which could overwhelm and “suffocate” the produced signal. Therefore, a second approach was selected and developed.

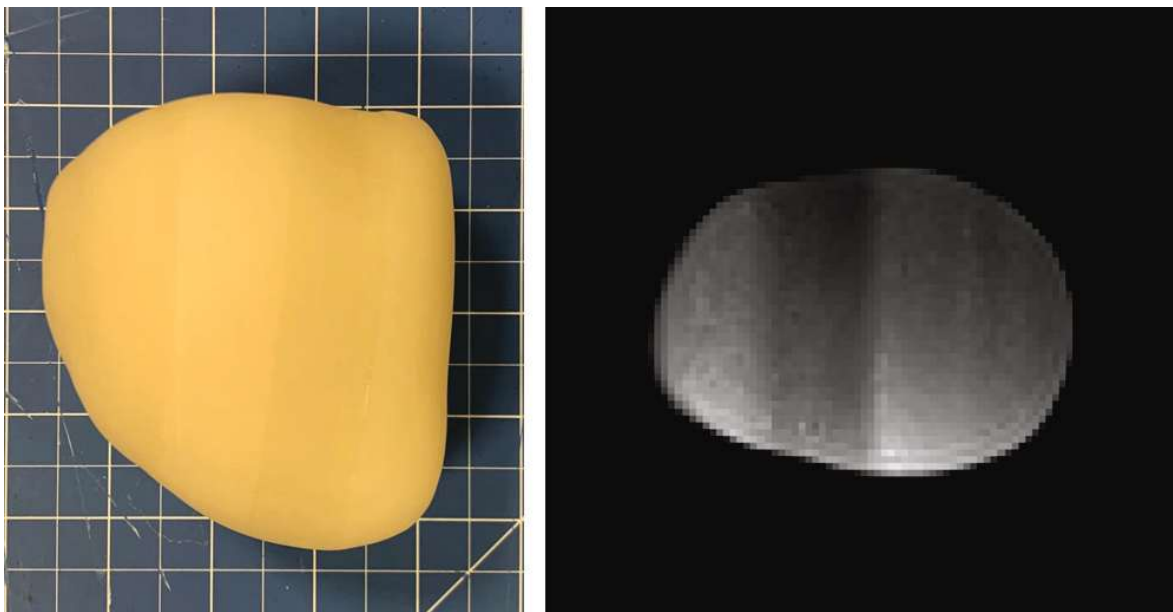


Figure 3.31: **Left:** Photograph of the first iteration of the heart phantom, produced on novel MR visible additive manufacturing material, on a cm grid for scale. **Right:** MRI scan of the same heart phantom as the left image, in its transversal plane.

3 Phantom Design and Development

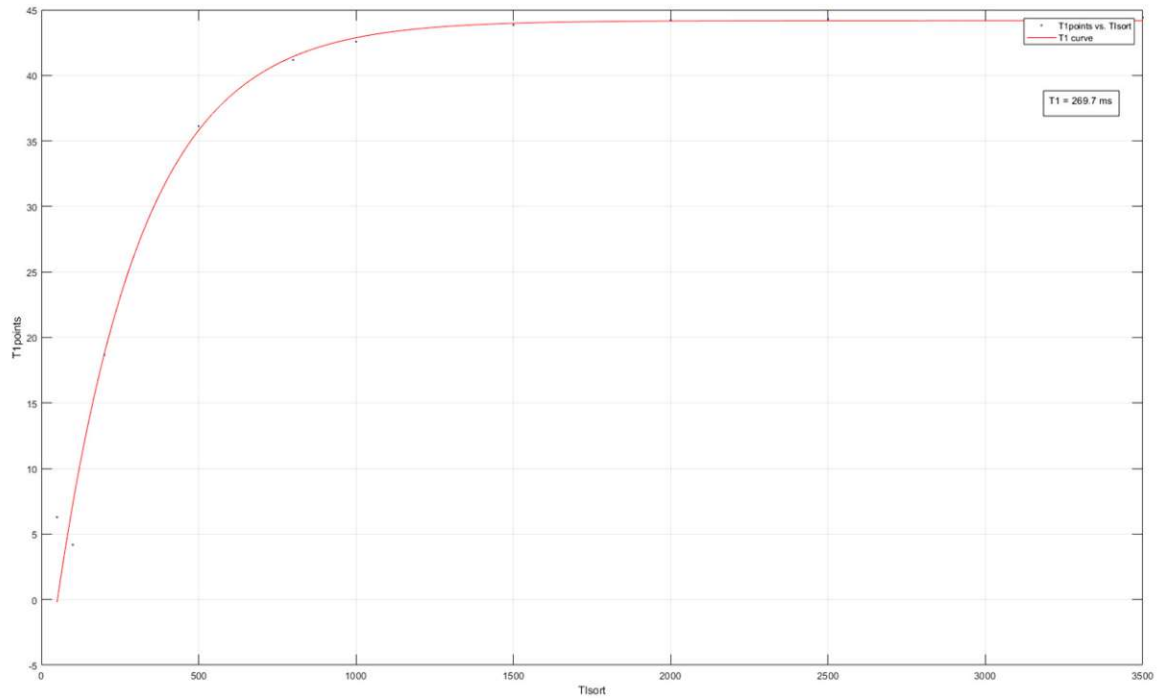


Figure 3.32: Inversion recovery measurement plot for T_1 determination of the additively manufactured MR visible heart phantom.

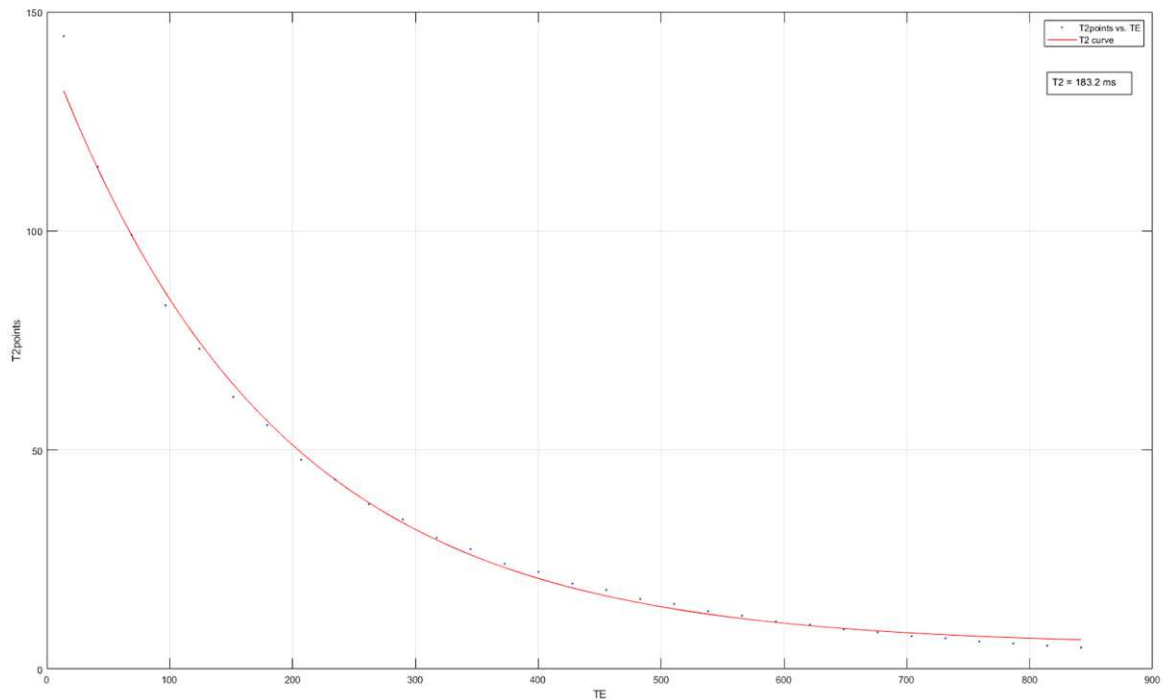


Figure 3.33: Spin-echo measurement plot for T_2 determination of the additively manufactured MR visible heart phantom.

On this second heart phantom approach, it was decided to print a hull with the same scanned heart shape, using the same procedure and material as for the liver phantom of the AOB. This resin is not MR visible. For that reason, the hull will be filled with a stiff gelatinous substance similar to the fluid in the OS with the addition of agar (exact recipe and ratios in Point 3.5.3) to achieve a rigid substance that movement will not displace. This gelatin has already been

3 Phantom Design and Development

successfully tested and used in various older MR phantoms [34]. Therefore, it is trusted to perform with optimal phantom characteristics. For the gelatinous substance to be filled inside the hull, an opening was foreseen on the heart shape, with a screwable top to provide closure to the body.

A fitted inlay was designed for the heart phantom to fit into the receptacle box without any instability or shaking while the box moves. This inlay perfectly fits the box on its sides. The surface on which the heart sits was designed using the heart shape as the cutting tool. Therefore, the heart phantom can sit inside a negative projection of its shape for the purpose of denying any movement, fitting tightly inside. This complex shape was printed with an FDM printer with some modified tolerances to optimize the fitting of the print. This inlay approach was already developed for the first heart phantom and was only optimized and adapted for the second iteration. The CAD of the final heart phantom and inlay can be seen in Figure 3.34.



Figure 3.34: CAD render of the second iteration heart phantom with its inlay, measurement in mm for scale. Colored in red is the main heart body, yellow for the closing screw top, and gray for the heart inlay. **Left:** isometric view of the heart phantom. **Middle:** isometric view of heart phantom inside the inlay. **Right:** side view with a sagittal cut of the heart phantom inside the inlay.

Once the MR visible part is finalized and its position in space is fixed, its actuation system has to be developed. As mentioned, no piezo stage will be used for the heartbeat movement since it is not necessary and saves resources, as well as being very inconvenient to transfer the movement to an already moving module. Furthermore, if placed in the already limited space inside the MP could lead to material artifacts even in their non-magnetic configuration. MR-compatible stepper motors were also discarded for their insufficient speed and possible high price. This left us with the choice between developing an MR-safe hydraulic system or a pneumatic one. The final selection was a pneumatic system since the tolerances and safeties for a hydraulic one are too high to confidently avoid a fluid leak inside the scanner in case of failure. This is not the case for pneumatics since only air is required. Pneumatic systems can not lift as much weight as hydraulics and are less controllable in their movement, only providing two stable positions during the movement. Nevertheless, this was enough for the requirements of the movement, where only a short high-frequency vibration-like movement was needed in the case of the heartbeat motion. Facilitating this way, the creation of the HM. Now, an MR-safe pneumatic system had to be developed, given that no MR-safe pneumatic pistons are widely commercially available. The pneumatic system does not only need to be MR-safe but also free of metal since it will be placed inside the MP. The position of the piston is to be placed underneath the recipient heart box since it is the only free space left inside the OS. It could have also been placed outside the OS as the piezo stages are. Still, when placed inside, it not only makes the system more compact and ordered but also eliminates the need for a long movement transmission piece, enabling a smoother, safer, and more homogenous pull-push action on the already moving heart box.

3 Phantom Design and Development

The developed piston was roughly based on the whole metal compact double action cylinder model ADN-S from the company Festo GmbH (Germany). A double-action piston was developed to avoid a metal spring for the piston to retract. This way, there was only the need for a DIN normed double solenoid valve (Festo GmbH, Germany), electromagnetically actuated, to be positioned outside of the scanner room, from where two (3 mm inner diameter) polymer rigid tubes had to go into the bore and supply each side of the pneumatic cylinder with pressurized air. This pressurized air comes from an air compressor from the brand Adler (Austria), which has a capacity of 150l and a possible maximal pressure of 11 bar. This compressor is more than enough to actuate the piston over a long time period since only a pressure between 1.5-2bar is needed. The piston has an outer size of 50x50 mm, with only a small chamber of 32 mm diameter by 28 mm length and a relatively high surface area in comparison. The surface area is 8.04 cm² on the non-shaft side (A) and 6.91 cm² on the shaft side (B), being the shaft 12 mm in diameter and 8 mm in width. Therefore, the chamber has a volume of 0.016 dm³ (A) and 0.014 dm³ (B), with a thrusting force of 121 N (A) and 104 N (B). Furthermore, since all the utilized materials are polymers, and the piston is held together with polyamide nylon screws, higher forces could create a piston rupture. The piston chamber is drilled out of a solid polymer rectangular stock piece, making it stronger against the pressure. Onto this chamber, a cover is screwed on and closed by sealing O-rings and machine grease. This grease not only prevents air escape but also reduces the friction of the piston shaft against its opening. A CAD model of the piston can be seen in Figure 3.35.

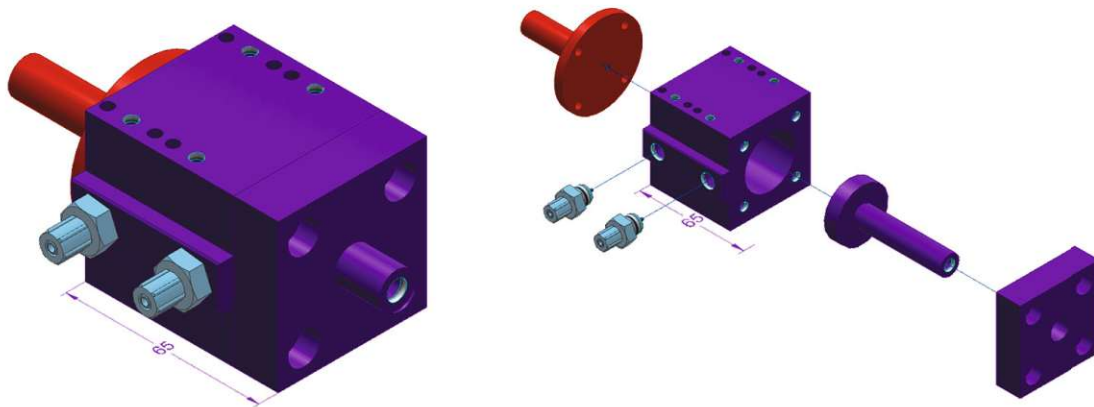


Figure 3.35: CAD render of the HM pneumatic piston with a measurement in mm for scale. Colored in dark blue are the piston chamber, lid, and shaft. Colored light blue is the air vents, and red is the supporting shaft. It can be viewed assembled on the left side as a whole and on the right as an explosion view to better illustrate the connections and inner parts.

Since the piston is under the box containing the heart phantom, the force, and movement had to be transmitted from below. Taking this fact into account, a two-platform design was created for the heart box to sit and glide along. Considering that the heart phantom is not too heavy, the piston has more than enough force for the load, and the PVC plates used for them have a low friction coefficient, it was decided that no rolls or bearings were needed in the case of this movement, which turned out to be correct for this short displacement. The piston was then suspended from below the plates, being attached by screws on each side of the gap separating the plates. Therefore, the module is as compact as possible, and the force transmission between the piston and the box can be short to ensure that no moments arise, which could degrade the module's integrity over time. (See Figure 3.36)

In the first sketches, it was thought that the connection between the heart phantom box and

3 Phantom Design and Development

the moving shaft of the pneumatic piston was to be attached by a reinforced plate. The piston shaft emerges in the cranial direction and moves along the cranio-caudal line. Therefore, the plate would be connected through the gap between the guiding plates and the box's cranial side. This solution raised concerns about the created moments and the asymmetry of the push-pull motion. In turn, this led to the design of a three-plate fork force transmission. This connecting system consists of three plates and a supporting shaft. This extra shaft was secured to the back of the piston. An elongated plate was then fixated along the whole bottom surface of the heart box, between the gap of the supporting pair of plates, using them as guides and rails in the movement. This attached plate is then fixed to two vertical plates at each end. One of these vertical plates is positioned to glide along the length of the supporting shaft, while the other plate is securely attached to the end of the pneumatic piston shaft. This solution transfers homogeneous movement along an extensive surface area while being supported on both ends by shafts to decrease moments as much as possible. The solution can be seen in Figure 3.36.

Since this movement can be somewhat erratic and uncontrolled due to the nature of pneumatics, where air fills the piston chamber in different ways each pulse, safety measures had to be implemented. Therefore, thin walls were positioned around the sliding plates even though little room was left to spare inside the OS. These plates not only help constrain the heart box's movement in case of failure but also increase the rigidity and stability of the two main plates.

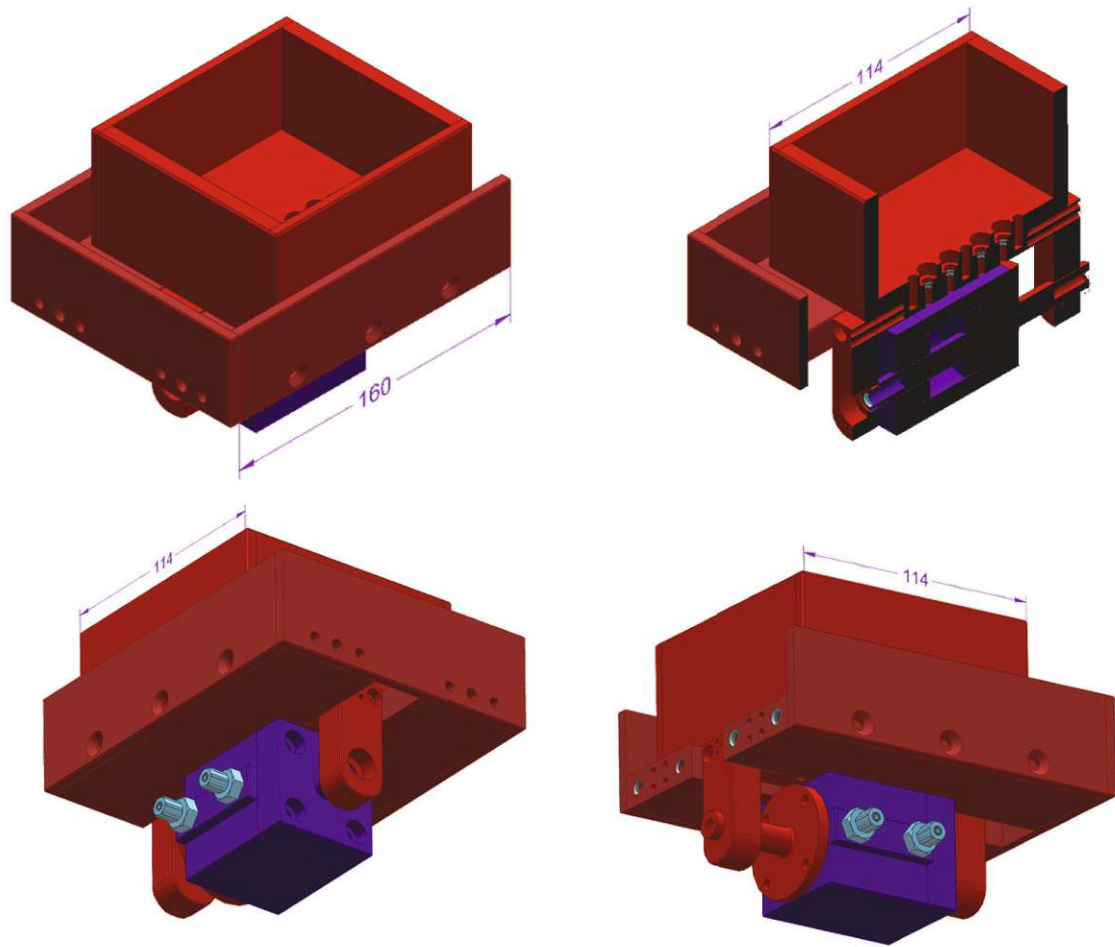


Figure 3.36: CAD renders of the HM module with measurements in mm for scale, colored for better differentiation. Red for the heart phantom box, supporting shaft, and connecting plates. Dark red for the guiding plates and safety constraining plates. Light blue for the pneumatic vents. Dark blue for the piston housing and piston shaft. **Top left:** top-front isometric view. **Top right:** same as top left but with a sagittal cut for better visualization. **Bottom left:** bottom-side isometric view. **Bottom right:** bottom back isometric view.

With the structural parts in place, the controller for the heartbeat motion had to be selected and developed. The pressurized air came from the compressor through rigid tubing to the valves of the piston inside the MP, passing through the controller valve. This valve redirects the air through the closing and simultaneous opening of the airflow of each tube, enabling the filling and emptying of each piston chamber with each pulse. This valve is controlled by a data acquisition (DAQ) card from the company National Instruments (USA). This DAQ card, with the model NI-USB-6001, enables a signal to be coded in a computer program such as MatLab (MathWorks, USA) and be transferred to control and power the valve. The basics of the encoding are simple, taking into account the refreshing rate of the card, a Matrix is established with 1's and 0's, representing the open or closed state of each side of the valve. This two-column matrix has as many values as the control rate per second. This way, how many times per second the state of each side of the valve should change to actuate the piston can be coded, even being able to code a slight delay to avoid an overlap in the open state of both openings. That way, the signal can be controlled to achieve a 1-2Hz movement. This mentioned code and signal can be found in Appendix.02 and 03.

3 Phantom Design and Development

The second motion necessary for this HM module is the breathing motion, as is also found in the CM and AOB. The CM movement has different characteristics, but the AOB motion has the same requirements as the breathing for the HM. Furthermore, it is preferable for all the breathing motions to be synchronized in their phase and frequency for their physiological accuracy. Therefore, it was opted to “recycle” the movement of the AOB. The AOB module is large and has a considerable vertical surface in its cranial end to be able to attach the whole HM, which is smaller and lighter than the AOB. Since this connection was already envisioned while designing the AOB module, the cranial wall was planned accordingly, over-dimensioned in its thickness to support the HM module. The attachment points of the two modules can be seen in Figure 3.25, at the left side of the module, when viewed from the cranial direction, as well as already attached in Figure 3.38. The two supporting plates of the AOB are also substantially thick to support the whole AOB and have enough space for enough screws and pins for the attachment. Furthermore, the additional supporting shaft of the piston was also screwed against the AOB plate to avoid moments and create a more stable three-point support. This connection can be viewed in Figure 3.36.

Through this attachment, The HM can have a short and fast high-frequency motion while having a secondary slower motion with a longer amplitude. This way, it does not matter that the motions are dephased and can be separately controlled and adjusted for future testing needs.

Since the whole HM module is floating over the ground plate to be able to move with the AOB, it is not supported at all against the OS base plate. Although the weight of the HM does not surpass the weight of 1 kg, which is about 4-5 times less than the AOB, it still creates a tilt and a moment onto the AOB. This will aggravate the AOB bulk's sliding motion against its monorail, which could lead to a non-smooth movement across the rolls, even being able to damage them. In a worst-case scenario, the whole structure could lean or even tip over since the HM also creates forces with the heartbeat motion. To ensure that this is not the case, two supporting rolling pillars were designed to support the HM while allowing linear horizontal movement. This way, it is guaranteed that no tilting actions can occur. The two supporting pillars are carefully manufactured to be the exact height in order to barely touch the base of the two support plates. The pillars have each one roll to allow for a smooth movement of the whole HM module in the cranial-caudal direction. The rolls were reused from the AOB monorail design. The left pillar (from a cranial perspective) came in the way of the pneumatic pistons input valves if it were designed with the same simple structure as the right one. To avoid this collision, it was constructed to have a C-shape to gain enough clearance space while being symmetrically positioned to the right one. This support also helps reduce the strain on the piezo stage that will move the AOB and HM combined module, which is advantageous since the piezo stage has a low force. In this way, the linear motor only needs to pull and push a rolling weight instead of lifting or supporting it. The supporting pillars can be seen in Figure 3.37 in the assembly.

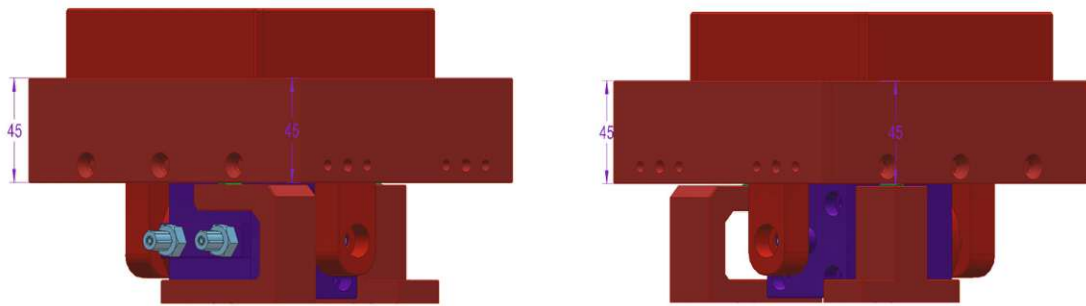


Figure 3.37: CAD render of the HM module with the two different supporting pillars, with a measurement in mm for scale. Both renders are viewed from a cranial-side direction. The left render shows the C-column in the front and the right one the standard column.

The final movement functionality of the HM module is indicated in Figure 3.38 for clarity.

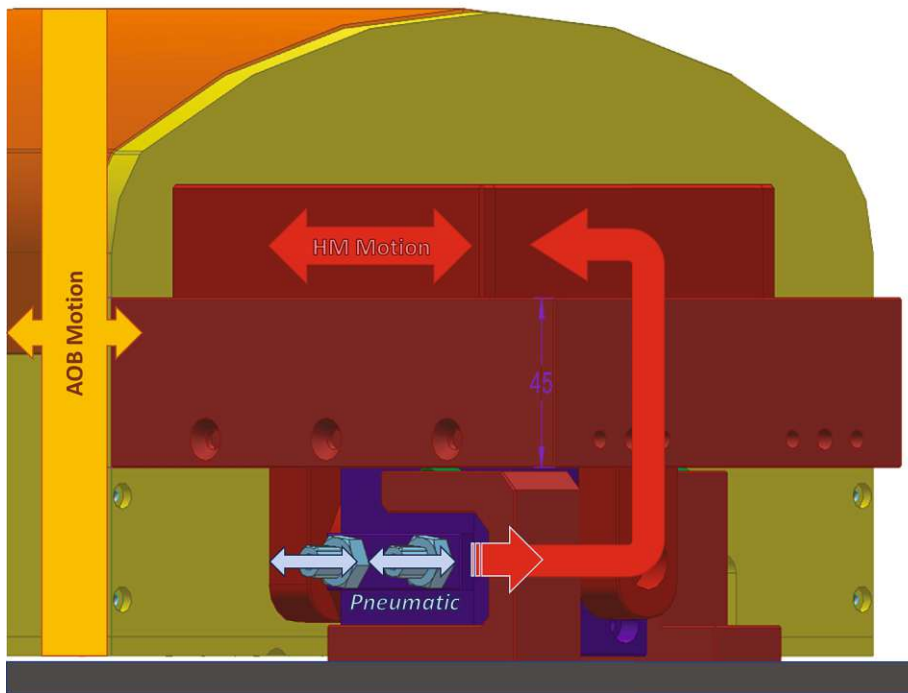


Figure 3.38: CAD render of the HM module attached to the AOB, with supporting pillars and base plate, in isometric edge view, measurement in mm for scale. Arrows are added to emphasize functionality and motion.

3.5.3 Manufacturing and Materials

For the first heart phantom iteration, a novel patented material is used. This material consists of the Anacubic UV resin with a suspension of paraffin oil microcapsules with a diameter of 0.8-10 μ m, where the microcapsules create the signal. Due to the heavy weight of the part, it had to be split into four slices and glued together. Each slice was printed in the Anacubic Photon M3 SLA printer. As shown in Figure 3.31, the slices have inhomogeneous signal strength due to manufacturing inconsistencies in this new process. The inhomogeneity can be

3 Phantom Design and Development

explained by the sedimentation of the microcapsules during the printing of each slice, lowering the capsule density and, therefore, the signal.

The second heart iteration was printed using the same materials and methods as the liver phantom. Therefore the heart shell was printed in Formlabs Form 3 SLA printer, making use of Formlabs Clear V4 resin. The stiff gel inside the heart shell is a mixture of 3.5% Agarose to enhance T_2 and create the gel-like consistency, $100\mu\text{mol/kg}$ of gadopentetic acid (gadolinium-based) to enhance T_1 , 0.1% of NaCl to increase the conductivity and 0.05% of NaN_3 to increase the longevity of the solution against decay. All these chemicals are diluted in distilled water, filled in the phantom, and let to stiffen up to its stiff gelatinous consistency. This gelatin then possesses similar relaxation times as the simulated heart muscle, achieving a T_1 of 1.2 s and a T_2 of 45 ms.

The heart phantom inlay form was printed in an Ultimaker 3 FDM printer using the Polymaker PLA. The Cura slicer was used for all printing jobs to get the STL-files ready for printing. The manufactured heart phantom, filled with water to show water tightness, and the printed heart inlay can be seen in Figure 3.39.



Figure 3.39: **Left and middle:** Photograph of the printed final iteration of the heart phantom filled with water, side and front view, respectively. **Right:** Photograph of the printed heart phantom inlay in isometric view.

For the pneumatic controls, the mentioned DAQ card and compressor were used. The solenoid valve that splits the pressurized air to each piston chamber was a 5/2 way solenoid valve with the model VUVG-LK14-B52-T-G18-1H2L-S. Before the air comes from the compressor to the solenoid valve, it passes through an on/off valve (MS4-EM1-1/8-S) and gets reduced in its pressure from 11 bar to 1.5 bar by a pressure regulator (MS4-LR-1/8-D5-AS). All the commercial pneumatic components are from the company Festo GmbH (Germany). The pneumatic controller setup, with an additively manufactured holder and box, which would sit outside the scanner room, can be seen in Figure 3.40.

3 Phantom Design and Development

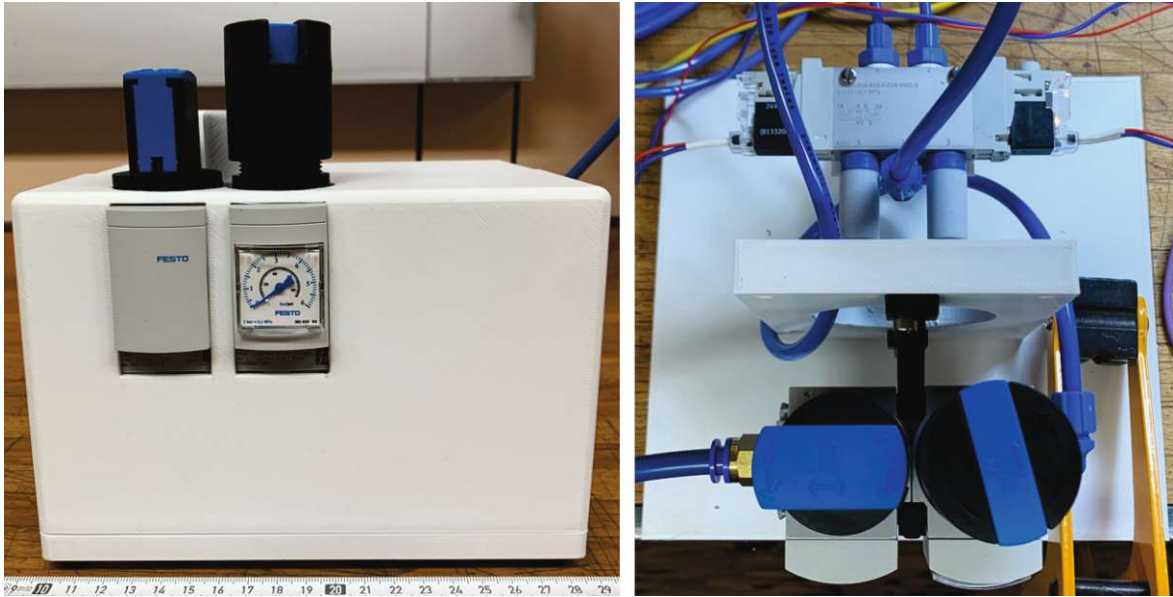


Figure 3.40: Photographs of the pneumatic controller setup. **Left:** front view with casing. **Right:** top view without casing.

The rest of the raw stock used in this module is processed the same way as previously stated in the sections of the other modules. It is in its majority hard PVC, except for the piston shaft and the pillar rolls, which is PA 6 due to its lower friction and higher hardness.

The manufactured HM assembled and attached to the other modules can be viewed in Figures 3.41 and 3.42.

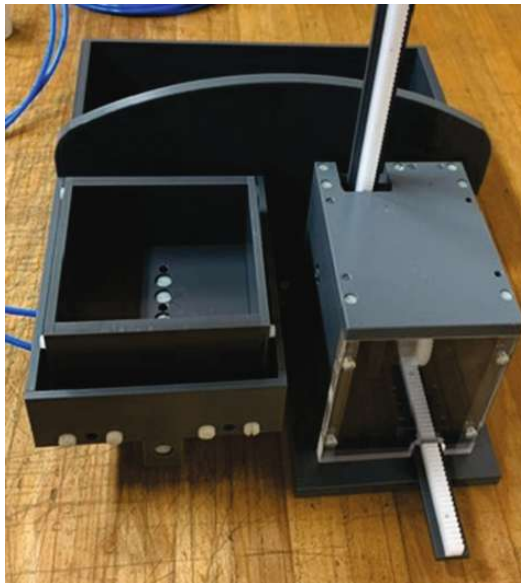


Figure 3.41: Photograph of the manufactured HM attached to the AOB and next to the CM's Gear Box.

3.5.4 Test and Evaluations

In order to ensure the functionality of the HM, a motion test had to be done. In the case of this module, all the actuating and controlling hardware and software were already available by the time it was manufactured. Therefore, the DAQ card could be attached to the computer for the aforementioned MatLab code, with the chosen signal to be inputted (see Appendix.02). The DAQ card then controls the solenoid valve, which in turn splits the reduced pressure (1.5 bar) from the compressor alternatingly into the two piston chambers. The signal length was shortened sequentially to assess the maximum frequency achievable through the pneumatic system. The system enabled full movement up to a frequency of 3 Hz. Over this threshold, the piston still functioned correctly but did not achieve a movement with full amplitude. This means that the piston shaft did not arrive at the second stable position before it was actuated to return to its starting position. This happened even when increasing the pressure up to 2.5 bar, which is the chosen safety threshold.

This phenomenon also illustrates the more “uncontrolled” nature of this movement actuation since the motion is only regulated by its frequency, while the amplitude-curve is not fully controllable by the user. The start and end positions are fixed, but the velocity and the movement pattern from one point to the other can not be determined due to the compressive nature of air and, therefore, pneumatics.

Another discovered characteristic is that the piston needs an additional external force to start its first motion after very long periods of disuse. This is probably due to the fact that the piston's face gets compressed against the sealing gasket as well as the machine grease, creating an adherence effect. Yet, this can be easily solved, by positioning the piston manually in a center position for longer idleness or storage periods, avoiding the mentioned adherence.

Lastly, a final test was done in the workshop, testing the pneumatic movement while actuating the breathing movement of the AOB and CM. During this test, the three mentioned modules were attached to a self-made base plate, as a stand-in for the ordered OS base plate. Since the piezo stages were not available by the time of the test, this combined breathing movement was actuated by a CNC machine. Usually, the CM and AOB have to be actuated separately since the CM needs a longer amplitude and higher velocity due to the gear reduction of the Gear Box. Along with the dephase in both movements for the same reason. In this test, the HM was attached to the AOB, uniting the two independent motions, for ease of testing. The test setup in CMPBME's workshop can be seen in Figure 3.42. In conclusion, the test worked as planned, with smoothed and controlled motions. Nevertheless, this test has to be repeated once the final parts of the MP are manufactured or delivered, such as the piezo stages and OS parts.

3 Phantom Design and Development

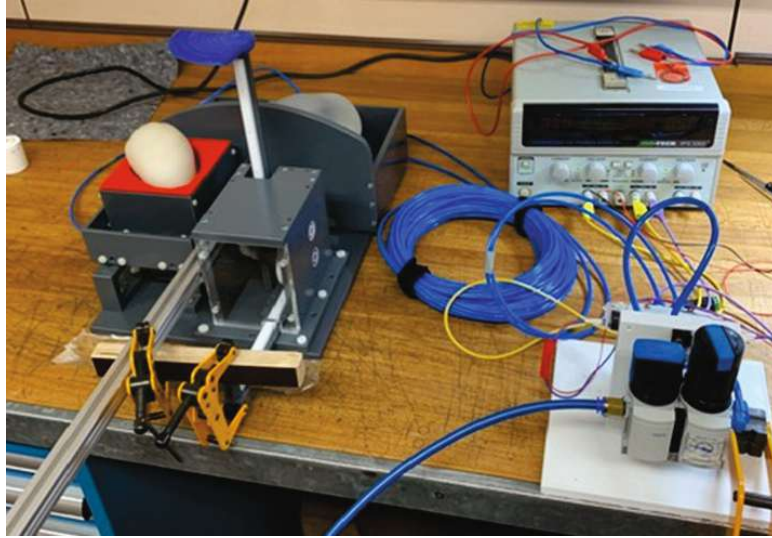


Figure 3.42: Photograph of the functionality test actuated by the final pneumatic system and CNC machine as a stand-in for the piezo stages. This test was done directly in the workshop at CMPBME.

3.6 Scanner Plate (and extra Hardware)

3.6.1 Requirements

To make the handling of the MP easier, as well as to simplify the alignment of the piezo stages to the MP, a Scanner Plate (SP) was foreseen. This SP should fit in the inlay of the 3T MR scanner patient bed. To improve handling, some holders or cutouts should be designed for the SP to be carried by two persons with the whole MP fixed on top. Therefore, an attachment for the MP should be designed. Furthermore, a hole grid should be foreseen for the piezo stages mount to be attached and arranged, as well as the supports for the force and movement transmission from the piezo stages to the MP.

3.6.2 Design

For the design of the SP to correctly fit in the foam inlay of the scanner's patient bed, some side cutouts had to be done. These cutouts also doubled as positioning holes to get a more precise and repeatable placement of the whole SP in the scanner, as well as functioning as carrying holders to ease the handling of the long SP. Clamping bars with an adjustable rail system were developed to mount the OS onto the SP.

These features can be seen in the CAD illustration provided by the manufacturing company in Figures 3.43 and 3.44.

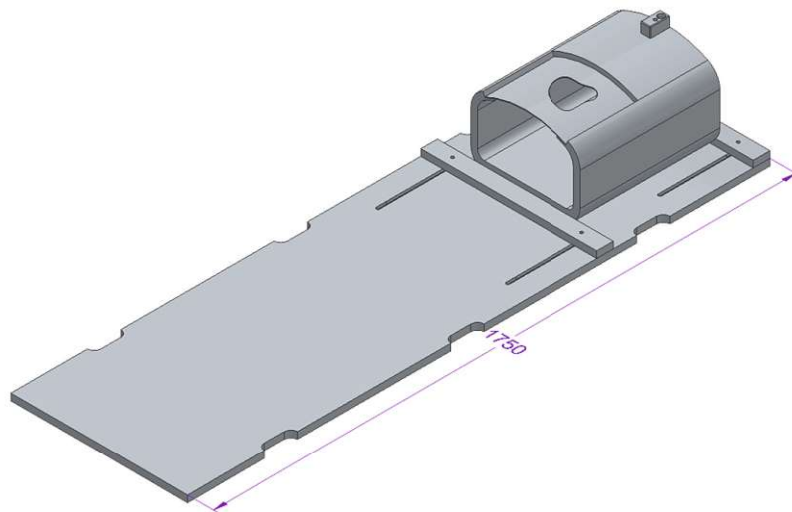


Figure 3.43: Functional CAD render of the MP with its filling vent, SP, and clamping system provided by Acrylstuido GmbH, with a measurement in mm for scale.



Figure 3.44: Visual CAD renders from the MP with its filling vent, SP, and clamping system provided by Acrylstudio GmbH.

These are all the developments done for the last parts of the MP at the time of the writing of this thesis.

3.6.3 Manufacturing and Materials

The manufacturing of this module is foreseen to be done by the polymer company Acrylstudio GmbH, the same as the OS. The main material used for this part will be hard PVC, which can already be found also being used in every other main module of the MP. The remaining parts will be designed once the piezo stages are delivered. These parts are the motor transmission rods and their supports, as well as the piezo stage mounts and the pneumatic tube holders.

4 Discussion

In the scope of this thesis, the MR compatible MP with three degrees of freedom (2x breathing motion & 1x cardiac cycle) was fully conceptualized, and all modules were successfully designed in detail. The manufacturing process was nearly finished, waiting only for the delivery of the OS, SP, and piezo stages. Nevertheless, the development will still go on when these parts arrive. Furthermore, this unique product will be used as a research tool, capable of adapting and modifying to future experimental needs. Regardless, some limitations and optimizations for the future can already be observed.

4.1 Assessments and Limitations

4.1.1 Evaluation of Module Design

The MP design, conceptualized in sketches and created in CAD, was an exact way to deliver precise designs, which could be virtually assembled using DIN parts. Through the use of a technical program such as Solid Edge, the parts conformed to workshop standards. Nonetheless, in this type of iterative process, where the prototype is sometimes already the final product, some compromises have to be made, and limitations are encountered which could be optimized in future iterations.

The OS, SP, and CM designs were optimal as far as could be seen in this stage of the development process. When the planned tests are done, parts such as the pushing head of the CM could be further optimized.

Potential optimizations could already be identified for future iterations of the AOB module. However, its functionality is more than sufficient for the first trials, fulfilling all requirements. The monorail of the AOB could be improved by offsetting the two upper roll columns, making them asymmetrical, to ensure constant contact of the end of the AOB wagon with the rail rolls. This avoids the slight tilt of the wagon when it steps out of contact. Another development point to keep in mind when the piezo stages arrive is the programming of the movement curve. Due to the weight of the AOB, a non-abrupt breaking in the movement has to be foreseen in order to ensure that no parts endure too much force from the momentum of the AOB. Planning a smooth breaking and acceleration movement of the motors to take care of and preserve the parts involved in the movement. Lastly, the horizontal hole where the CM rack goes into the AOB could be minimized by precisely timing the two movements, in case this air pocket induces artifacts.

The HM module was surprisingly reliable and functional, even though it was the first try to produce a custom metal-free pneumatic system. The movement was reproducible with adjustable frequency with the help of the controlling system. Still, some aspects should be observed with more detail when the final system is tested. One of these is the effect that the HM motion has on the AOB motion, as a consequence of being attached to each other, which could induce further forces on the piezo stages, shifting the AOB motion.

4 Discussion

Overall, the MP design was satisfactory, and no further iterations were needed, being also very translatable from the CAD design to the physical parts. This translation can be seen in the following Figures, where the overall CAD assembly can be viewed next to the manufactured assembly as far as it was completed by the time of this thesis.

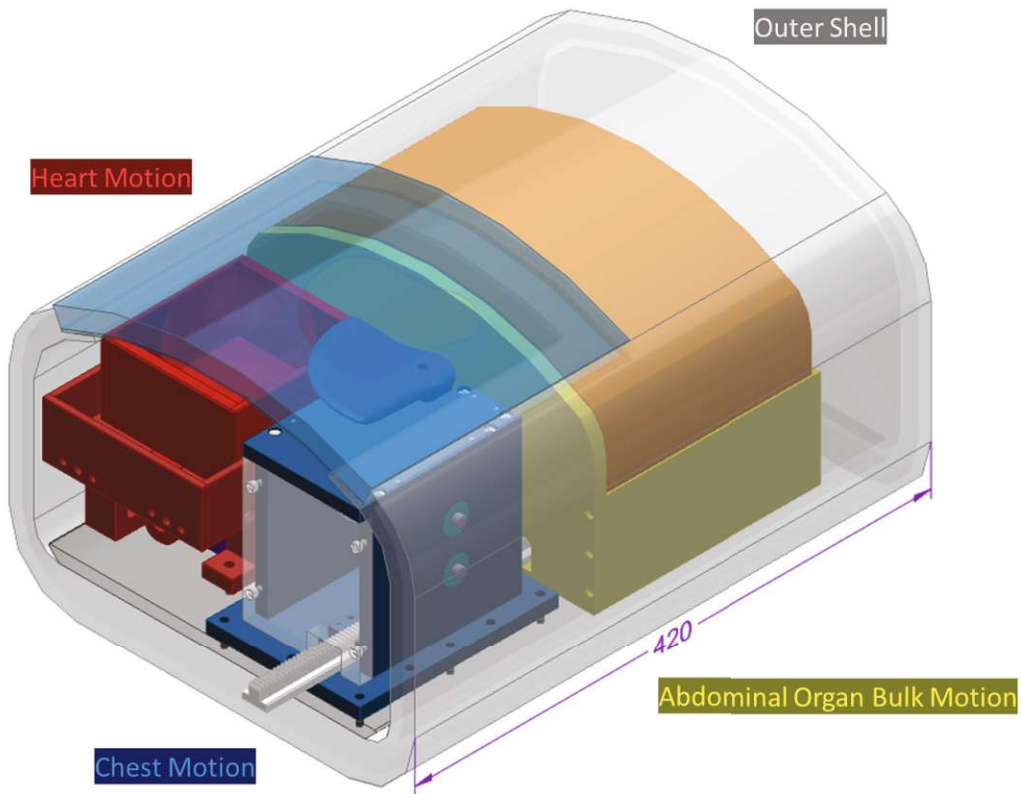


Figure 4.1: CAD render of the final design of the whole MP with length measurement in mm for scale, in isometric view. The main modules are color-coded for ease of identification. Gray/transparent → Outer Shell, blue → Chest Motion, yellow/orange → Abdominal Organ Bulk, red/violet → Heart Motion.

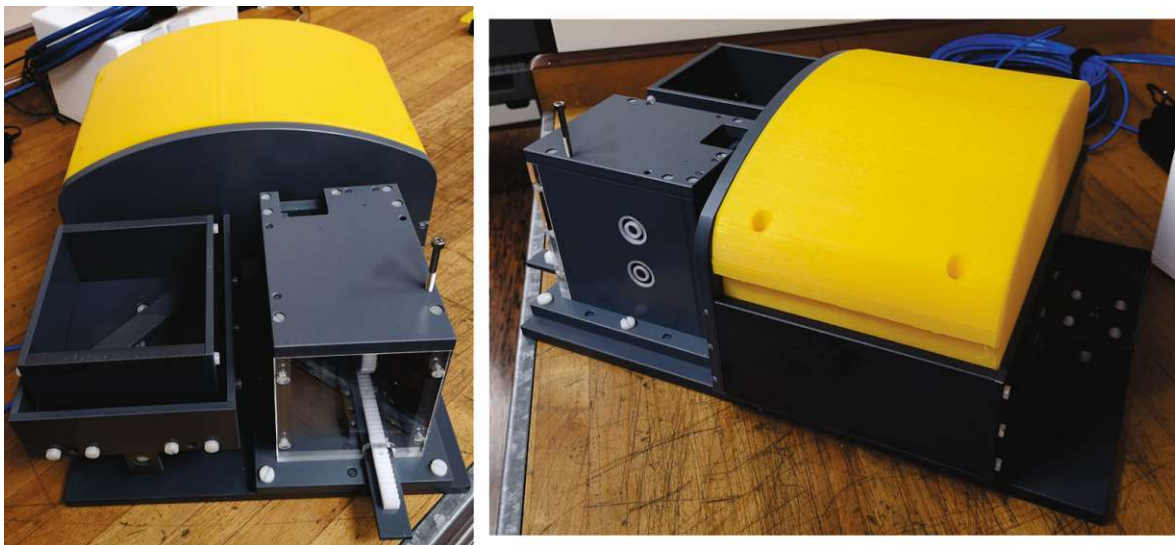


Figure 4.2: Photographs of the assembled MP with the AOB printed shell placed inside. Front (left) and side (right) view.

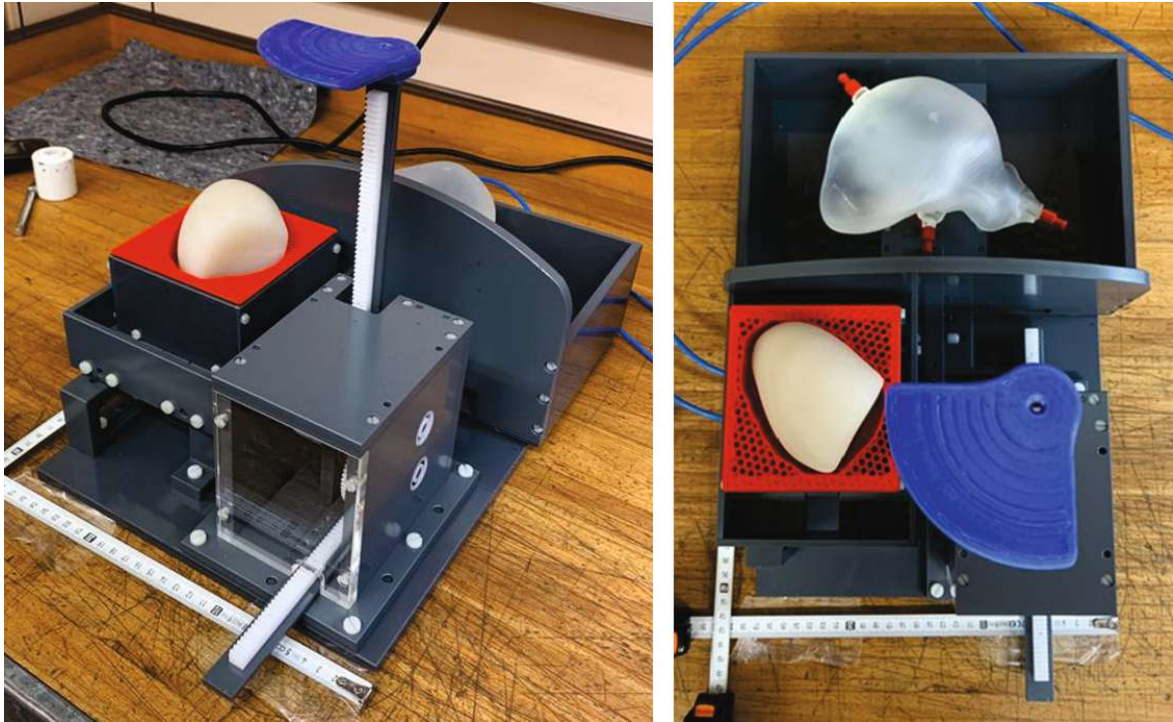


Figure 4.3: Photographs of the final assembly of the MP with all the manufactured parts by the time of the preliminary functionality tests, with first heart phantom iteration, liver phantom, push head (to be shortened based on the exact dimensions of the OS after fabrication), and temporary base plate. Isometric (left) and top (right) view.

4.1.2 Evaluation of Module Manufacture and Materials

All the manufacturing processes that could be controlled for this project were done at a high professional level, achieving optimal results for the required purposes. All the structural parts that could be done by standard manufacturing methods or needed accurate tolerances were done at the precision workshop at CMPBME. Also, large FDM prints or refined watertight SLA prints were done there. Non-structural parts that did not require tight form tolerances were done with the FDM printer of the RF-Lab, in order to hasten the process.

Some material limitations were observed during the preliminary test done on the single modules or parts of the MP. During the cross-validation test with the Beat Pilot Tone, it was noticed that the CM gel mat did not have high enough conductivity characteristics for the movement to be measured with the desirable sensitivity by the Beat Pilot Tone. This is not a problem when the coil is attached or placed on the surface, which is the case for the BraCoil, which will be used in the scope of the MP tests. Nevertheless, this conductivity issue is non-trivial since salt can not be added to increase it like it is done in the solution of the OS. Therefore, it should be addressed if it is needed in future tests.

This conductivity issue also arose in the additively manufactured heart phantom since no salt could be dissolved in the paraffine oil microcapsules. For this reason, as well as the low and inhomogeneous signal intensity produced by this material (Figure 3.31), due to possible microcapsule sedimentation during the printing process, the heart phantom was changed. In its second iteration, with just an SLA-printed shell filled with an agar-based gel, the conductivity and signal intensity can be adjusted to the required needs.

4 Discussion

To further optimize the AOB monorail, on top of the factors mentioned in 4.1.1, some manufacturing and material adjustments can be made. To achieve an increase in smoothness of the linear rail movement, the rolls could be made adjustable. Due to material and manufacturing processes, the tolerance of a fraction of millimeters can already be noticed in the transition contact from roll to roll. However, this enhancement might be too resource-consuming for the slight improvement it would achieve.

4.1.3 Evaluation of Project Management

Although this project was very demanding on its design part, with some manufacturing and post-processing procedures, also management aspects substantially contributed to the overall workload. Since several research groups in the AKH will use this project's result, their needs and feedback had to be acquired and assessed.

The MP is a testing tool that is going to be offered to a large multi-disciplinary team at the physics and radiology department of the AKH. Their future needs and current suggestions were obtained through numerous meetings and discussions to try to accommodate them as early as possible in the development process. Nevertheless, due to the large variety of needs, there were also competing interests in the MP features, such as the movement or material type of the HM. To acknowledge these cases, the MP was developed as modular and interchangeable as possible to avoid disuse after the first tests. Some of the parts and modules that were done in cooperation with other teams are the whole HM, the printing of MR visible material, the SLA printing of anatomical scans, the liver phantom destined for PET-MR, the pneumatic controller acquisition and coding, as well as the cross-validation with the Beat Pilot Tone system.

This was not the only management process that went into the project. After the search for MR-compatible components and teams/companies that could manufacture or deliver them, the orders had to be managed and supervised. This meant, for example, weekly meetings with the CMPBME workshop to ensure that the parts were manufactured to the specific requirements. However, more challenging were the meetings with external companies, like those manufacturing and delivering the piezo stages or the acrylic OS parts. Compromises, mostly on delivery time, were not easy since this changed the development timeline severely in some cases, prolonging the development of the MP by weeks or even months.

External factors, such as international rulings, policies, and catastrophes that influenced the companies' ability to deliver on time or get specialized parts, also influenced the MP. For example, due to delivery shortage, it was decided to increase the expenses on the piezo stages to get the non-magnetic version instead of the low-magnetic one. This ensured that the already lengthy delivery of six months did not further increase the project's length to take more than a year to be finalized. This, in turn, improved the MP by decreasing in size and possibly reducing metal artifacts of the low magnetic piezo stages.

4.2 Outlook

4.2.1 Phantom Development Outlook

Given that one of the main characteristics of the MP development is its modularity, the development only stops when there is no more need for this MP. This means that if a team of the AKH needs a torso motion module with specific characteristics in the future, it can be made to work in the context of the MP.

Nevertheless, by the time of this thesis, the initial equipment of the MP is not finalized. The piezo stages still have to be delivered, and a movement/force transmission has to be designed for them, as well as connections to the modules and dedicated support for them in the SP. The OS is still on delivery and must be filled and tested. When these parts arrive and are completed, a final motion test and a functionality examination inside the MR scanner have to be performed. Only after this test can it be determined that all the single parts do not create artifacts as a whole assembly and give the necessary signal where needed. Other characteristics besides motion and signal must also be checked, such as shimming, in the more spacious parts, and be filled with MR visible material if required.

Besides the future module development and some of the part optimization already mentioned in the Sections above, some future changes could be made to the standard module layout of the MP.

The gel mat could be custom-made in order to increase its conductivity for better movement pick-up by the RF coils with Beat Pilot Tone. The AOB could be guided on top of sunk ball bearings instead of a monorail to minimize the air gap to the base plate and erase the need for a bulky monorail. Decreasing, therefore, the non-MR-visible space. If needed, the heart motion could be made more complex by adding a heart rotation on top of the translational motion for the movement to be closer to the physiological one. If this motion is still too simplified, a liquid-filled pulsatile heart phantom could also be developed.

4.2.2 Phantom Use Outlook

As mentioned above, the MP will be further developed in the future for upcoming needs. Some of these needs are already known, arose as new ideas while developing the phantom, or got attracted from other teams when the functionalities of the MP were presented.

The first uses for the MP will be the further cross-validation and tuning of motion tracking methods, such as Beat Pilot Tone and the motion correction algorithm GRICS (Generalized reconstruction by inversion of coupled systems) using the Beat Pilot Tone data, or other future motion tracking methods, such as optical real-time motion corrections.

Through this MP, a reproducible, quantifiable motion can be done, which could help the motion tracking systems achieve an absolute motion value determination. Being able to assess precisely the amplitude and frequency of distinct patient motions. Which could severely help in future motion/motion artifact reduction studies.

The MP will also be used for testing and developing wireless RF coils, for instance, optical data transfer systems. In order to increase the precision of this absolute motion value

4 Discussion

movement, the CM gel mat could be replaced by a rigid breast mat that does not have an elastic inaccuracy.

As for future module ideas, the PET MRI liver phantom could be made to be perfused in real-time. Therefore, acquiring flow values that could help TIPS (Transjugular intrahepatic portosystemic shunt) patients, on which the liver study is being done because of the liver shunt, which is needed in their therapy.

Further uses of the AOB system could be the study of the kidneys in motion through breathing, employing renal MRI since a kidney phantom could be easily placed in the still-free space of the AOB.

Furthermore, the HM module is already planned to have an alternative version for MR elastography in the form of an elastic pressurized balloon. Other possible alternative versions could be the creation of a more anatomical-shaped heart with its internal chambers or the development of an internally liquid-flowing heart phantom in a stationary or pulsatile version.

To conclude, even non-MRI final uses could be included. For instance, a spine model could be included, which could be used as image registration in radiation therapy planning, adapting the used material according to its X-ray absorption and therefore getting a more precise radiation emission location.

Lastly, the MP could also be used in totally different cases that have yet to be considered.

5 Conclusion

This thesis presents the successful development process of an MRI-compatible torso motion phantom. This MP had to be able to recreate the chest elevation and abdominal organ compression of the breathing motion, as well as the movement of the heartbeat. Additionally, it needed to contain a liver phantom for liver perfusion studies. All this while being optimally MR-visible as close to the anatomical reference as possible. At the same time as being metal-free, in order to be MR-safe and free of material artifacts, limiting the tools available when building a professional engineering machine. All along, achieving reliable, reproducible, and exact movement to develop, validate and calibrate MR motion tracking and correction systems.

It starts with an early conceptual phase which quickly flows into an extensive design stage, which through the use of CAD, managed to create a precisely defined digital model divided into distinct functional units. This model accomplished the requested requirements and provided a highly modular design that could be easily translated into a physical phantom thanks to its nature of accurate dimension. The iterated designs could be used by trained manufacturing personnel and companies or even directly inputted into additive manufacturing printers to create the desired parts. All the different precise methods were needed to create a medical laboratory standard research tool.

Furthermore, novel manufacturing methods or custom-made pieces had to be used in order to achieve the MR compatibility required, which was the major constraining factor in the development process. The physical MP could not be finalized due to delivery restrictions from part of external suppliers. Nevertheless, the concept and design of a functional modular MP were adequately finalized, as well as the complete ordering of parts and the final manufacturing of most modules.

The HM was fully built, and its controlling system was developed and tested. The CM and AOB are manufactured, waiting on their actuating systems. Lastly, the OS and SP are fully designed and ordered. These designed and manufactured parts can be seen in Figures 4.1, 4.2, and 4.3. The remaining steps for the completion of a working MP are outlined and will be followed till completion in the future.

Concluding, for the time constraint of a diploma thesis, a complex novel and unique research tool such as the MP was developed very far, with only a small team working on it, while the request and cooperation of other investigators and professionals had to be managed. Expectantly this MP will be of use not only for their first trials of improving motion tracking and correction systems but will provide helpful, through its conceptualized modularity, interchangeability, and adaptability, for many studies and investigations to come. Proving a valuable and meaningful research and development tool in the area of torso MRI and maybe even for medical imaging or medicine in general in the upcoming future.

List of References

- [1] KUPERMAN, V.: *Magnetic Resonance Imaging: Physical Principles and Applications*. Elsevier, **2000**; ISBN 9780080535708.
- [2] BROWN, R.W.; CHENG, Y.-C.N.; MARK HAACKE, E.; THOMPSON, M.R.; VENKATESAN, R.: *Magnetic Resonance Imaging: Physical Principles and Sequence Design*. John Wiley & Sons, **2014**; ISBN 9780471720850.
- [3] SPRAWLS, P.: *Magnetic Resonance Imaging: Principles, Methods, and Techniques*. Medical Physics Publishing Corporation, **2000**; ISBN 9780944838976.
- [4] REISER, M.F.; SEMMLER, W.: *Magnetresonanztomographie*. Springer-Verlag, **2013**; ISBN 9783642560446.
- [5] SUETENS, P.: *Fundamentals of Medical Imaging*. Cambridge University Press, **2017**; ISBN 9781107159785.
- [6] HENDRIX, A.: Siemens Medical Solutions: *Magnets, spins, and resonances: an introduction to the basics of magnetic resonance*. Siemens-Aktiengesellschaft, Berlin, **2003**.
- [7] LIPTON, M.L.: *Totally Accessible MRI: A User's Guide to Principles, Technology, and Applications*. Springer Science & Business Media, **2010**; ISBN 9780387488967.
- [8] FRERICKS, B.B.; MEYER, B.C.; MARTUS, P.; WENDT, M.; WOLF, K.-J.; WACKER, F.: *MRI of the Thorax during Whole-Body MRI: Evaluation of Different MR Sequences and Comparison to Thoracic Multidetector Computed Tomography (MDCT)*. *J. Magn. Reson. Imaging*, 27: 538–545, **2008**; <https://doi.org/10.1002/jmri.21218>
- [9] RÖMER, P.B.; EDELSTEIN, W.A.; HAYES, C.E.; SOUZA, S.P.; MUELLER, O.M.: *The NMR phased array*. *Magn Reson Med*, 16: 192-225, **1990**; <https://doi.org/10.1002/mrm.1910160203>
- [10] OBERMANN, M.; NOHAVA, L.; ROAT, S.; FRASS-KRIEGL, R.; LAISTLER, E.: *BraCoil - a Wearable One-Size-Fits-All Breast Coil for 3 T MR Mammography*. In Proceedings of the ISMRM, **2022**.
- [11] HENOUMONT, C.; LAURENT, S.; VANDER ELST, L.: *How to Perform Accurate and Reliable Measurements of Longitudinal and Transverse Relaxation Times of MRI Contrast Media in Aqueous Solutions*. *Contrast Media Mol. Imaging*, 4: 312–321, **2009**.
- [12] ZIEGLER, S.; BRAUN, H.; RITT, P.; HOCKE, C.; KUWERT, T.; QUICK, H.H.: *Systematic Evaluation of Phantom Fluids for Simultaneous PET/MR Hybrid Imaging*. *J. Nucl. Med.*, 54: 1464–1471. **2013**.
- [13] DU, J.; MA, G.; LI, S.; CARL, M.; SZEVERENYI, N.M.; VANDENBERG, S.; COREY-BLOOM, J.; BYDDER, G.M.: *Ultrashort Echo Time (UTE) Magnetic Resonance Imaging of the Short T2 Components in White Matter of the Brain Using a Clinical 3T Scanner*. *Neuroimage*, 87: 32–41 **2014**.

List of References

- [14] LARSON, P.E.Z.; HAN, M.; KRUG, R.; JAKARY, A.; NELSON, S.J.; VIGNERON, D.B.; HENRY, R.G.; MCKINNON, G.; KELLEY, D.A.C.: *Ultrasbort Echo Time and Zero Echo Time MRI at 7T*. MAGMA, 29: 359–370, **2016**.
- [15] WEIGER, M.; PRUESSMANN, K.P.; HENNEL, F.: *MRI with Zero Echo Time: Hard versus Sweep Pulse Excitation*. Magn. Reson. Med., 66: 379–389, **2011**.
- [16] DILLENSEGER, J.P.; MOLIÈRE, S.; CHOQUET, P.; GOETZ, C.; EHLINGER, M.; BIERRY, G.: *An Illustrative Review to Understand and Manage Metal-Induced Artifacts in Musculoskeletal MRI: A Primer and Updates*. Skeletal Radiol., 45: 677–688, **2016**.
- [17] FILLI, L.; LUECHINGER, R.; FRAUENFELDER, T.; BECK, S.; GUGGENBERGER, R.; FARSHAD-AMACKER, N.; ANDREISEK, G.: *Metal-Induced Artifacts in Computed Tomography and Magnetic Resonance Imaging: Comparison of a Biodegradable Magnesium Alloy versus Titanium and Stainless Steel Controls*. Skeletal Radiol., 44: 849–856, **2015**.
- [18] KRUPA, K.; BEKIESIŃSKA-FIGATOWSKA, M.: *Artifacts in Magnetic Resonance Imaging*. Pol. J. Radiol., 80: 93–106, **2015**.
- [19] WEGNER, F.; VON GLADISS, A.; HAEGELE, J.; GRZYSKA, U.; SIEREN, M.M.; STAHLBERG, E.; OECHTERING, T.H.; LÜDTKE-BUZUG, K.; BARKHAUSEN, J.; BUZUG, T.M.: *Magnetic Particle Imaging: In Vitro Signal Analysis and Lumen Quantification of 21 Endovascular Stents*. Int. J. Nanomedicine, 16: 213–221, **2021**.
- [20] STRADIOTTI, P.; CURTI, A.; CASTELLAZZI, G.; ZERBI, A.: *Metal-Related Artifacts in Instrumented Spine. Techniques for Reducing Artifacts in CT and MRI: State of the Art*. Eur. Spine J., 18 Suppl 1: 102–108, **2009**.
- [21] WU, V.; BARBASH, I.M.; RATNAYAKA, K.; SAIKUS, C.E.; SONMEZ, M.; KOCATURK, O.; LEDERMAN, R.J.; FARANESH, A.Z.: *Adaptive Noise Cancellation to Suppress Electrocardiography Artifacts during Real-Time Interventional MRI*. J. Magn. Reson. Imaging, 33: 1184–1193, **2011**.
- [22] MISIRI, J.; KUSUMOTO, F.; GOLDSCHLAGER, N.: *Electromagnetic Interference and Implanted Cardiac Devices: The Medical Environment (part II)*. Clin. Cardiol., 35: 321–328, **2012**.
- [23] ZAITSEV, M.; MACLAREN, J.; HERBST, M.: *Motion Artifacts in MRI: A Complex Problem with Many Partial Solutions*. J. Magn. Reson. Imaging, 42: 887–901, **2015**.
- [24] NOLL, D.C.; SCHNEIDER, W.: *Theory, Simulation, and Compensation of Physiological Motion Artifacts in Functional MRI*. In Proceedings of the Proceedings of 1st International Conference on Image Processing, 3: 40-44, **1994**.
- [25] KATO, H.; KURODA, M.; YOSHIMURA, K.; YOSHIDA, A.; HANAMOTO, K.; KAWASAKI, S.; SHIBUYA, K.; KANAZAWA, S.: *Composition of MRI Phantom Equivalent to Human Tissues*. Med. Phys., 32: 3199–3208, **2005**.
- [26] KEENAN, K.E.; AINSLIE, M.; BARKER, A.J.; BOSS, M.A.; CECIL, K.M.; CHARLES, C.; CHENEVERT, T.L.; CLARKE, L.; EVELHOCH, J.L.; FINN, P.: *Quantitative Magnetic Resonance Imaging Phantoms: A Review and the Need for a System Phantom*. Magn. Reson. Med., 79: 48–61, **2018**.

List of References

- [27] SAGIAS, G.; YIALLOURAS, C.; IOANNIDES, K.; DAMIANOU, C.: *An MRI-Conditional Motion Phantom for the Evaluation of High-Intensity Focused Ultrasound Protocols*. Int. J. Med. Robot., 12: 431–441, **2016**.
- [28] DRANGOVA, M.; BOWMAN, B.; PELC, N.: *Physiologic Motion Phantom for MRI Applications*. J. Magn. Reson. Imaging, 6: 513–518, **1996**.
- [29] VALLADARES, A.; OBEROI, G.; BERG, A.; BEYER, T.; UNGER, E.; RAUSCH, I.: *Additively Manufactured, Solid Object Structures for Adjustable Image Contrast in Magnetic Resonance Imaging*. Z. Med. Phys., 3: 466–476, **2022**.
- [30] HASKELL, M.W.: *Retrospective Motion Correction for Magnetic Resonance Imaging*. Harvard University ProQuest Dissertations Publishing, **2019**; 28235969.
- [31] ANAND, S.; LUSTIG, M.: *Beat Pilot Tone: Exploiting Preamplifier Intermodulation of UHF/SHF RF for Improved Motion Sensitivity over Pilot Tone Navigators*. In Proceedings of the ISMRM: Meeting and Exhibition Abstract, **2021**.
- [32] WELCH, E.B.; MANDUCA, A.; GRIMM, R.C.; WARD, H.A.; JACK, C.R.: *Spherical Navigator Echoes for Full 3D Rigid Body Motion Measurement in MRI*. Magn. Reson. Med., 47: 32–41, **2002**.
- [33] XERYON: *How do piezo motors work?*, (recalled on **27.06.2023**), <https://xeryon.com/technology/how-do-piezo-motors-work/>.
- [34] WOLETZ, M.; ROAT, S.; HUMMER, A.; TIK, M.; WINDISCHBERGER, C.: *Technical Note: Human tissue-equivalent MRI phantom preparation for 3 and 7 Tesla*. Med. Phys., 48: 4387-4394, **2021**; <https://doi.org/10.1002/mp.14986>

List of Figures

2.1: Left: Schematic illustration portrayed by arrows of the precession movement around the z-axis of the static magnetic field M_0 , with most spins in the lower energy state parallel to M_0 [4]. Right: Schematic illustration of the Zeeman effect, portraying the split of the energy levels depending on the spin's new orientation in a static magnetic field [2]._____ 4

2.2: Schematic illustration of the types of RF coils used in MRI for each body location and their corresponding level of picked-up noise [3]._____ 6

2.3: Schematic diagram of the major components of an MRI system [3]. _____ 6

2.4: a: Photograph of a torso RF coil for breast cancer screening (BraCoil), made to be as flexible and comfortable as possible. b: Schematic view of the single coil arrays of the BraCoil [10]. _____ 7

2.5: Schematic diagram of MR image quality characteristics influenced by the selection of protocol factors [3]. _____ 9

2.6: Top: Graph with magnetization relaxation percent on the y-axis and time frame in ms on the x-axis - **(left)** MR transversal Brain image - **(right)** of T_1 relaxation times according to the tissue [6]. **Bottom:** Graph with magnetization relaxation percent on the y-axis and time frame in ms on the x-axis - **(left)** MR transversal Brain image - **(right)** T_2 relaxation times according to the tissue [6]._____ 10

2.7: Left: Schematic of an inversion recovery pulse sequence. **Right:** Diagram showing an exemplary T_1 definition graph with magnetization relaxation percent on the y-axis and time frame in ms on the x-axis.[11] _____ 11

2.8: Left: Schematic of a spin-echo pulse sequence. **Right:** Diagram showing an exemplary T_2 definition graph with magnetization relaxation percent on the y-axis and time frame in ms on the x-axis.[11] _____ 11

2.9: Tabular evaluation of different phantom fluids (rows) tested for PET/MR with different MR sequences (columns) [12]._____ 13

2.10: MRI image with an anterior distorted cruciate ligament reconstruction on a knee's sagittal plane using stainless steel screw. The image is highly distorted in its quality due to an artifact originating in the screw.[18]_____ 15

2.11: Comparison of a 50-year-old male patient's left complete hip replacement (Cr-Co) coronal MR image with T_1 Gradient echo in **a.** and T_1 Spin echo **b.** Although there are spatial distortions in the two pictures, the gradient-echo sequence **b.** exhibits a significantly decreased distortion signal.[16] _____ 15

2.12: **a.** and **b.** show an MRI of the spinal cord (sagittal plane)and femur head (coronal plane) with endoprosthesis, respectively, imaged with UTE for best results. **b. c. e.** and **f.** show the same endoprosthesis imaged with standard sequences to show the induced material artifacts. Arrows and stars mark the landmarks of the endoprosthesis across the images.[16] _____ 16

List of Figures

2.13: **a.:** Schematic of a metal rod (white arrow), surrounded by gelatinous water (black arrow), in the bore of an MR scanner, showing the static magnetic fields in the z-direction as well as the scanning direction and plane. **b.:** MR image of the metal rod described in **a.**, a dotted line indicates the actual position of the rod in space. Black stars denote signal pile-up, and white stars signal loss. The readout gradient is shown along the z-axis. **c.:** Schematic of the image shown in **b.**, with lines and arrows representing the direction of the induced magnetic field inside the metal rod, by the scanner. The red arrows show the direction of the highest field points, explaining the signal loss and pile-up.[16] _____ **17**

2.14: **a.:** Photograph of a cobalt-chrome alloy hip endoprosthesis suspended in a gelatinous agar-water mixture. **b.:** Coronal MR scan of **a.** showing pile-up artifacts (black stars) and signal loss areas (white stars) **c.:** Sagittal image of through-plane artifacts across the dotted line seen in image **b.**[16] _____ **17**

2.15: MR image in the sagittal plane of the pelvic region. **A:** Motion artifacts like bandaging and blurring can be observed due to peristalsis. **B:** Same imaged region as **A** but with fewer motion artifacts for comparison.[18, 23] _____ **19**

2.16: Schematic of pulse excitation on brain MRI. Three different pulses excite the same brain region over time, fully overlapping in the top row to create a high-quality image. The bottom row shows how the overlap can move through rotational and translational movement between each pulsation step. This creates a small region of total overlap, with the rest only partially overlapping or being recorded by just one excitation pulse. Which generates blurring, ghosting, and banding artifacts.[23] _____ **19**

2.17: MRI simulated images of an anatomic phantom. The level of recorded inconsistencies increases with every column from 12,5 % to 25 %, 37,5 %, and 50 % inconsistent data. The linear k-space acquisition is used for the first row and the two-shot interleaved acquisition in the middle row. The bottom row is the centric reordering of the middle row with an increase in data inconsistency from 50% to 62,5 %, 75 % till 87,5 %.[23] _____ **20**

2.18: **a:** Photograph of a vial filled with an MR-based biomarker. **b:** Multiple different vials placed in a phantom holder filled with deionized water. **c:** The MR-based biomarker solution for each vial can be estimated using MRI. In this example, values are (beginning at the 12 o'clock position and moving counterclockwise) 0, 5, 10, 15, 20, 30, 40, and 50%.[26] _____ **22**

2.19: Photograph of an MR motion phantom, which can convey movement to an MR-visible phantom cube, in the X-axis (from left to right in the Figure). **A:** extended telescopic shaft. **B:** collapsed telescopic shaft.[27] _____ **22**

2.20: Photograph of a selection of commonly used materials in MR phantom manufacturing. Starting from left to right. **Top row:** Elastic polyurethane fiber pad (gel mat), polypropylene board. **Bottom row:** Polylactic acid (PLA) used in FDM printing, MR visible polymer used in SLA printing, polyamides (PL) used in SLS printing, Polymethyl methacrylate (PMMA/Acrylic) in cylindrical or plate form. _____ **24**

2.21: Two diagrams of the recorded movement of a patient inside an MR scanner. The X-axis in both diagrams is the time in seconds. A breath hold was done after about 9 seconds. **Top:** Y-axis is the amplitude of the motion in m. **Bottom:** Y-axis is the Phase change in degrees.[24] _____ **27**

List of Figures

- 2.22:** Comparison between MR breast scans with three degrees of breathing intensity, before and after the motion correction, with data acquired by the Beat Pilot Tone (BPT) system and corrected through generalized reconstruction by inversion of coupled systems (GRICS).____28
- 3.1:** Schematic of the final devised layout of the MP with actuators in the scanner bore and controlling systems outside the scanner room. _____30
- 3.2:** Schematic of the MP and its different modules and parts in a front (**left**) and side view(**right**) at the proposal stage of the phantom development._____30
- 3.3:** Schematic of the MP and its different modules and parts in a front (left) and top view(right) at the start of the phantom development stage._____31
- 3.4:** CAD render of the whole MP with length measurement in mm for scale, in isometric view. The main modules are color-coded for ease of identification. Gray/transparent → Outer Shell, blue → Chest Motion, yellow/orange → Abdominal Organ Bulk, red/violet → Heart Motion._____32
- 3.5:** MRI image of an average adult torso used for reference for the MP. Superior (**left**) and lateral view (**right**)._____34
- 3.6:** CAD render of the first OS version with its length measurement in mm for scale, in isometric view. _____35
- 3.7:** CAD render of the final OS version with a length measurement in mm for scale, in isometric view. _____36
- 3.8:** CAD render of the OS plate with length measurement in mm for scale, in isometric view (**left**) and top view (**right**). _____36
- 3.9:** CAD render of the OS with its length measurement in mm for scale, in isometric view, with the support sheet (left) and the support sheet and gel mat (right)._____37
- 3.10:** Precise linear piezo stage from Xeryon with 3N output force in its 40mm travel range version and magnetic model type._____40
- 3.11:** CAD render of the gear pair solution of the CM with length measurements in mm for scale, in isometric view. From left to right in order from oldest to newest iteration. _____41
- 3.12:** CAD render of the CM rack and pinion solution with length measurements in mm for scale, in isometric view. From left to right in order from oldest to newest iteration. _____42
- 3.13:** FDM printed PLA push heads. The top view is in the upper row, and the bottom view is in the lower one, on a cm grid for scale. The curvature of the top contact surface of the print heads can be identified by their print layer pattern. **Left** = concave, **middle** = convex, **right** = flat. _____43
- 3.14:** CAD render of the final rack and pinion solution of the Gear Box with length measurements in mm for scale, in isometric view. As a whole, in the left representation and with missing front, side, and top outer panels to visualize the inside mechanism. _____43

List of Figures

3.15: CAD render of the final rack and pinion solution of the Gear Box with length measurements in mm for scale, in an isometric edge perspective. Arrows in each movement transfer step indicate the functionality of the movement, with particular emphasis between steps 4 and 5, where through a gear ratio, the force of the movement gets increased by a factor of 5.	44
3.16: Photograph of an elastic polyurethane fiber gel mat on a cm grid for scale.	45
3.17: Inversion recovery measurement plot for T_1 determination of the CM's gel mat.	46
3.18: Spin-echo measurement plot for T_2 determination of the CM's gel mat.	46
3.19: Functional schematic of the function of an ultrasonic resonant piezo motor with standing wave.[33]	47
3.20: Photograph of the build Gear Box. Isometric view on the left and front view on the right. The Gear Box is placed on a cm grid for scale.	48
3.21: CAD assembly of the designed parts for the CM's functionality test.	49
3.22: Photograph of the manufactured test parts attached to the Gear Box.	50
3.23: CAD render of the monorail system of the AOB, in isometric view, measurement in mm for scale.	53
3.24: CAD render of the AOB wagon, measurement in mm for scale. Both views are from the same part in isometric views. The left one is seen from a cranial-lateral direction, and the right one from a lateral caudal direction.	54
3.25: CAD render of the AOB shell, in isometric view, with measurements in mm for scale. Left image as a singular piece, and the right one with the shell fitted inside the AOB wagon.	55
3.26: CAD render of the AOB liver phantom, in isometric view, with a measurement in mm for scale. The main liver body is colored gray, while the veins are colored yellow. The left top image is the whole phantom, while the phantom can be viewed through an intersectional cut on the right top. The bottom images are of the AOB shell with the phantom inside, as a whole, and with a viewing cut, respectively (left and right).	56
3.27: Photograph of the final additively manufactured liver phantom filled with a water solution on a cm grid for scale. Left = top view, middle = front view, right = bottom view.	56
3.28: Photograph of the manufactured AOB monorail on a cm grid for scale. Left = isometric view, middle = top view, right = side view.	57
3.29: Photograph of the manufactured AOB wagon on the monorail, viewed from the caudal end.	57
3.30: Photographs of the printed AOB shell. Top left: front view of the main body with the liver phantom. Top right: back-top view of the main body with the liver phantom. Bottom left: top view of the main body. Bottom right: bottom view of the shell lid.	58
3.31: Left: Photograph of the first iteration of the heart phantom, produced on novel MR visible additive manufacturing material, on a cm grid for scale. Right: MRI scan of the same heart phantom as the left image, in its transversal plane.	60

List of Figures

- 3.32:** Inversion recovery measurement plot for T_1 determination of the additively manufactured MR visible heart phantom. _____ **61**
- 3.33:** Spin-echo measurement plot for T_2 determination of the additively manufactured MR visible heart phantom. _____ **61**
- 3.34:** CAD render of the second iteration heart phantom with its inlay, measurement in mm for scale. Colored in red is the main heart body, yellow for the closing screw top, and gray for the heart inlay. **Left:** isometric view of the heart phantom. **Middle:** isometric view of heart phantom inside the inlay. **Right:** side view with a sagittal cut of the heart phantom inside the inlay. _____ **62**
- 3.35:** CAD render of the HM pneumatic piston with a measurement in mm for scale. Colored in dark blue are the piston chamber, lid, and shaft. Colored light blue is the air vents, and red is the supporting shaft. It can be viewed assembled on the left side as a whole and on the right as an explosion view to better illustrate the connections and inner parts. _____ **63**
- 3.36:** CAD renders of the HM module with measurements in mm for scale, colored for better differentiation. Red for the heart phantom box, supporting shaft, and connecting plates. Dark red for the guiding plates and safety constraining plates. Light blue for the pneumatic vents. Dark blue for the piston housing and piston shaft. **Top left:** top-front isometric view. **Top right:** same as top left but with a sagittal cut for better visualization. **Bottom left:** bottom-side isometric view. **Bottom right:** bottom back isometric view. _____ **65**
- 3.37:** CAD render of the HM module with the two different supporting pillars, with a measurement in mm for scale. Both renders are viewed from a cranial-side direction. The left render shows the C-column in the front and the right one the standard column. _____ **67**
- 3.38:** CAD render of the HM module attached to the AOB, with supporting pillars and base plate, in isometric edge view, measurement in mm for scale. Arrows are added to emphasize functionality and motion. _____ **67**
- 3.39:** **Left and middle:** Photograph of the printed final iteration of the heart phantom filled with water, side and front view, respectively. **Right:** Photograph of the printed heart phantom inlay in isometric view. _____ **68**
- 3.40:** Photographs of the pneumatic controller setup. **Left:** front view with casing. **Right:** top view without casing. _____ **69**
- 3.41:** Photograph of the manufactured HM attached to the AOB and next to the CM's Gear Box. _____ **69**
- 3.42:** Photograph of the functionality test actuated by the final pneumatic system and CNC machine as a stand-in for the piezo stages. This test was done directly in the workshop at CMPBME. _____ **71**
- 3.43:** Functional CAD render of the MP with its filling vent, SP, and clamping system provided by Acrylstudio GmbH, with a measurement in mm for scale. _____ **72**
- 3.44:** Visual CAD renders from the MP with its filling vent, SP, and clamping system provided by Acrylstudio GmbH. _____ **73**

List of Figures


- 4.1:** CAD render of the final design of the whole MP with length measurement in mm for scale, in isometric view. The main modules are color-coded for ease of identification. Gray/transparent → Outer Shell, blue → Chest Motion, yellow/orange → Abdominal Organ Bulk, red/violet → Heart Motion. _____ **75**
- 4.2:** Photographs of the assembled MP with the AOB printed shell placed inside. Front (**left**) and side (**right**) view. _____ **75**
- 4.3:** Photographs of the final assembly of the MP with all the manufactured parts by the time of the preliminary functionality tests, with first heart phantom iteration, liver phantom, push head (to be shortened based on the exact dimensions of the OS after fabrication), and temporary base plate. Isometric (**left**) and top (**right**) view. _____ **76**

List of Tables

- 2.1:** Table of motion artifact mitigation strategies classified by their type and application time during the image acquisition progress.[23] _____ **26**

Appendix


Appendix.01: Xeryon Linear Stage Datasheet



XLS-3 series

Precise linear piezo stage with high force output

The XLS-3 series are precise linear stages driven by an ultrasonic piezo motor. These stages combine high-speed positioning with nanometre precision and generate a high force output within a small volume. Xeryon's ultrasonic piezo motor ensures you a long lifetime, noiseless and vibration-free operation. In addition, the self-locking piezo motor holds the position of the stage when powered off. The reduced heat dissipation leads to a very stable nano-positioning system. The XLS-3 is used in metrology applications, e.g. for part alignment or sample manipulation. The XLS-3 series is available in different lengths and are easily stacked into an XY- or XYZ-assembly.



Key features

drive principle	patented Crosscor™ ultrasonic piezo technology
bearings	precision cross-cor roller
lifetime distance	> 100 km
control principle	closed-loop or open-loop position control
operating voltage	20 to 48 V

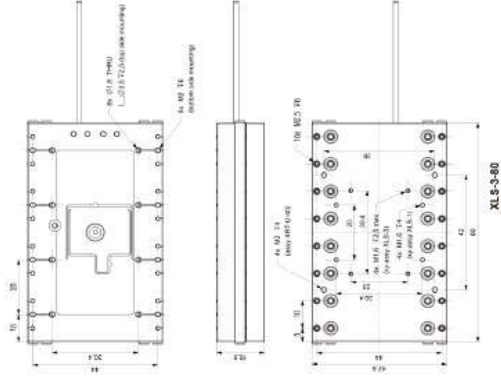
Model code structure

stage type	stage length (mm)	encoder resolution (nm)	vacuum compatibility (10 ⁻⁶ mbar)	optional low- or non-magnetic bearings	short cage for increased stroke
XLS-3	-OPEN	-1250	-HV	-LM / -NM	-SC
	-40	-312			
	-50	-78			
	-60	-5			
	-70	-1			
	-120	same as for XLS-3-40			

Environmental compatibility

temperature range	-30°C to +70°C
humidity range	20% to 90% RH (non-condensing)
heat dissipation (motor only)	< 5 W
mounting surface flatness	< flatness specification of stage

Appendix



Note: stages XLS-3-60, XLS-3-60, XLS-3-70, XLS-3-100 and XLS-3-120 have similar mounting holes as shown in the drawings above.

Last updated: 30.06.2023. All specifications are subject to change without prior notice.

www.xeryon.com

Appendix.02: MatLab Code for Pneumatic Control of the HM

```
d = daq("ni");
d.Rate = 5000; %5000 = max Samplerate for analog output

%% add output channel
ch_out1 = addoutput(d,"Dev2","ao0","Voltage")
ch_out2 = addoutput(d,"Dev2","ao1","Voltage")
% addoutput(d,"Dev2","Port0/Line0","Digital")
% addoutput(d,"Dev2","Port0/Line1","Digital")

%% generate waveform
n = 5000;

one_array = ones(1,n/4-n/100); %number of samples to be one -> ON State
zero_array = zeros(1,n/4+n/200); %number of samples to be one -> OFF
State

shiftzero_array = zeros(1,n/200); %shift of the vector, is needed, so
thaht no overlap of the output occurs (see plot)

analog0_out= [shiftzero_array one_array zero_array]; %Output Vector 1
analog1_out= [zero_array one_array shiftzero_array]; %Output Vector 2

analog_out=[analog0_out' analog1_out']; %Output Matrix

% frequency = d.Rate/size(analog0_out,2); %frequency of the cycle

figure, plot(analog_out) %plot of the two output signals
amplitude=3.3; %amplitude 3.3V for mosfet

%% Start output
preload(d,amplitude*analog_out); %Load output matrix with amplitude
start(d,"RepeatOutput");

%%

stop(d)

write(d, [0 0]);
```

Appendix.03: MatLab Signal for Pneumatic Control of the HM

